DESIGN, ANALYSIS AND DEVELOPMENT OF A MORPHABLE WING STRUCTURE FOR UNMANNED AERIAL VEHICLE PERFORMANCE AUGMENTATION

by

ABHIJIT HIRAMAN SUPEKAR

Presented to the Faculty of the Graduate School of

The University of Texas at Arlington in Partial Fulfillment

of the Requirements

for the Degree of

MASTER OF SCIENCE IN MECHANICAL ENGINEERING

THE UNIVERSITY OF TEXAS AT ARLINGTON

May 2007

DEDICATION

My thesis is entirely dedicated to my most loving family and friends in India. I have missed a lot of precious moments due to my studies abroad. My father and my mother have supported and constantly encouraged me to work hard to achieve my goals. My elder sister Ashwini and her husband Prashant along with their most adorable kids Shambhavi and Swanandi have always cheered me up. And my role models, my sister Amruta and her husband Kedar have been the invincible source of encouragement. Their motto “Be Focused and Work Smart” has shore me up till date. Last but not the least my friend, Malavika, has been the most understandable friend and has played an important role in the achievement of my career objectives. Without all their encouragement and understanding it would have been impossible for me to finish this work.

ACKNOWLEDGEMENTS

I would like to express my gratitude to all those who gave me the possibility to complete this thesis.

First a very special thanks to Professor Kamesh Subbarao. Dr. Subbarao constantly gave me the confidence and support for my Master's program at The University of Texas at Arlington. He was always focused to look for solutions to problems rather than be just focused on the problem itself. He helped me understand the basics of aircraft design and motivated me through the importance of our work on the future of aerospace industry. It was Dr. Subbarao's idea of the morphable wing that I have tried my best to give the shape he expects.

Equally, I would like to thank Dr. Kent Lawrence for the advice and suggestions on the design and analysis of the wing structure. His help and suggestions on the use of ANSYS have been unmatchable. Dr. Lawrence made possible the Static Wing Divergence calculations.

I thank Dr. Wen Chan for his timely suggestions during the research and also to be a part of the Master's program committee to evaluate my work.

Apart from my advisors, I owe a very sincere thanks to all my colleagues, especially Michael Byron Webb. Through his discussions and ideas on building the wing I was able to do a better job. It was possible only through his efforts to build a controller that my wing is able to morph. I thank Sohan Lal, a craftsman in India, for the

important time, knowledge and advise he gave me to build the complicated parts of the balsa wood prototype. I also thank Dr. Frank Lu and the Aerodynamics Research Center to provide me the workspace and tools required to build the wing prototype. And I also extend warm thanks Dr. Don Seath and my lab mates Brandon Shippey and Christen Soto for the time and help to conduct the wind tunnel test.

And I would like to mention that when things seemed to be impossible in this country away from home, I found another home with my room-mates Purushottam, Abhinav and Varun.

May 1, 2007

ABSTRACT

DESIGN, ANALYSIS AND DEVELOPMENT OF A MORPHABLE WING STRUCTURE FOR UNMANNED AERIAL VEHICLE PERFORMANCE AUGMENTATION

Publication No. _____

Abhijit Hiraman Supekar, MS

The University of Texas at Arlington, 2007

Supervising Professor: Dr. Kamesh Subbarao

In this research, we propose mechanisms to continuously morph a wing from a lower aspect ratio to a higher and to further extremities of a gull and an inverted-gull configuration. The mechanism comprises of a linear actuator for the extension of the wing and the servo motors to obtain the gull and inverted gull configurations. The initial design and preliminary finite element representation using 3D-beams and plates in ANSYS Classic were the benchmarks to proceed for the detailed structural analysis of the complete wing in ANSYS Workbench. An elliptical pressure distribution at the quarter cord is assumed for the linear static structural analysis. From these results the modified 3D-CAD model developed in CATIA, is imported in ANSYS Workbench and

used to compute the vibrational mode frequencies to avoid any resonance conditions due to the combined operation of the servo motors and the structure. The structure is also tested to ensure that the final model is light in weight and is stressed within the factor of safety. These results are useful for the next stage of the prototype development and its related instrumentation. A preliminary computational aerodynamic analysis conducted includes the use of the Athena Vortex Lattice (AVL) code to obtain basic aerodynamic parameters such as the drag polar and, lift curve slope and the pitching moment slope as functions of angle of attack. These results along with its comparison with the flight phases of the seagull provide an insight into the aerodynamic effects of morphing. Further, the wing is also tested numerically for static wing divergence speed at various stages of extension. A systematic method is developed to calculate the structural stiffness' of the wings non-uniform geometry which changes over the span. Thus, the torsional deformation and influence function is calculated and the static wing divergence speed is determined. An observation of the change of divergence speed with the changes in the aspect ratio is made. Finally, the wing prototype is tested in low-speed wind tunnel, and thus used to validate the aerodynamic benefits of morphing. It is not the goal of this research to mimic bird kinematics. Rather, the objective is to select a biologically-inspired system to improve the range of achievable flying conditions for an Unmanned Aerial Vehicle (UAV).

Keywords: *Adaptive Wing Technology; Biomimetics; Linear Static Analysis; Modal Analysis; Static Wing Divergence; CFD; Wind Tunnel Testing;*

TABLE OF CONTENTS

ACKNOWLEDGEMENTS iv

ABSTRACT vi

LIST OF ILLUSTRATIONS x

LIST OF TABLES xiv

Chapter

1. INTRODUCTION 1

1.1 Need For Adaptive Wing Technology 1

1.2 Related Work 3

2. BIOLOGICAL MOTIVATION 7

2.1 Characteristics Of Bird Flight 7

2.2 Seagull Flight 10

3. WING DESIGN AND ANALYSIS 16

3.1 Morphing Mechanism Conceptualization 16

3.2 Design Constraints And Preliminary Structural Analysis 22

3.3 Detailed Structural And Vibrational Analysis 32

4. AERODYNAMIC BENEFITS OF MORPHING 40

4.1 Computational Aerodynamics 40

4.2 Comparison Between AVL Results And Observed Seagull Flight 48

5. STATIC WING DIVERGENCE..... 52

5.1 Introduction…….. 52

5.2 Theory Of Wing Divergence 53

5.3 Bending And Torsion Theory..... 62

5.4 Wing divergence of morphable wing 71

6. SUMMARY…….. 80

6.1 Conclusions……. 80

6.2 Proposed future work..... 81

Appendix

A. PHYSICAL DIMENSIONS OF THE BALSA WOOD PROTOTYPE 83

REFERENCES 97

BIOGRAPHICAL INFORMATION..... 101

LIST OF ILLUSTRATIONS

Figure Page

1.1 A multi-mission aircraft sortie 2

1.2 Broad classification of lift generating mechanisms 3

2.1 Bird wing shapes and aspect ratio 8

2.2 Seagull taking-off 10

2.3 Seagull soaring at higher altitude 11

2.4 Seagulls displaying its wing during steep descent 11

2.5 Seagull in a low level flight preparing to stoop down 12

2.6 Seagull preparing to land 13

2.7 Seagull showing differential wing extension 13

3.1 Seagull distinctly showing the two limbs of its wing in a gull configuration 16

3.2 Preliminary mechanism configurations 17

3.3 Case 1 – Unextended wing configuration 18

3.4 Front-isotropic view of the extended wing configuration 19

3.5 Top view of the wing showing 75% extension 19

3.6 Rear-isotropic view of the wing showing 75% extension 20

3.7 Telescopic and gull mechanism 20

3.8 Gull wing configuration 21

3.9 Inverted-gull wing configuration 21

3.10 Spanwise Lift Distribution for the unextended and extended wing configuration 23

3.11 Airfoil - NACA 0018 26

3.12 Elliptical wing loading at the quarter chord-line along the wingspan for unextended wing configuration 28

3.13 Applied boundary conditions for 3D beam elements and plate/shell element 29

3.14 3D spar element model (Maximum Deflection = 0.43 in) 31

3.15 3D beam element model (Maximum Deflection = 0.15 in) 31

3.16 IGES format imported in ANSYS Workbench showing arrangements inside wing structure without motors and gear-sets 32

3.17 Setup environment in ANSYS Workbench for structural and vibrational analysis 33

3.18 Application of aerodynamic loads of lifts and side force on the wing in the above configurations 34

3.19 Max. deflection in unextended (L) and extended wing (R) configurations 35

3.20 Maximum deflection in gull (left) and inverted-gull wing (right) configurations 36

4.1 Comparison between Theoretical C_L for Span = 40 in versus AVL C_L for unextended wing configuration 41

4.2 Comparison between Theoretical C_L for Span = 60 in versus AVL C_L for extended wing configuration 41

4.3 Comparison between AVL C_L-results for the four wing configurations 42

4.4 Comparison between AVL C_D-results for the four wing configurations 43

4.5 Comparison between AVL Drag Polar results for the four wing configurations 45

4.6 Comparison between AVL Lift / Drag results for the four wing configurations 46

4.7 Comparison between Co-efficient of Pitching Moment for the four wing configurations 47

5.1 Rigid 2D airfoil showing the aerodynamic forces and restoring moments 53

5.2 Slender straight wing 54

5.3 Deformation and influence function for slender straight wing 55

5.4 Plan-view of the unextended wing configuration 60

5.5 Side-view of the C.G. locations over the span for unextended configuration 61

5.6 Top-view of the C.G. locations over the span for unextended configuration 61

5.7 Variation of the area moment of inertia about the y-axis as a function of span for unextended configuration 63

5.8 Euler-Bernoulli Bending Theory (pure bending moment) 64

5.9 Test Problem – Structure with geometric and material properties as a function of length L 65

5.10 Beam subjected to an end shear load P 65

5.11 Beam subjected to an end moment M 66

5.12 Element 1 of the test problem 66

5.13 Deflections and rotations of the elements due to the end shear force applied to the test problem 66

5.14 Timoshenko Bending Theory (pure bending moment) 67

5.15 Beam subjected to an end shear load P 69

5.16 Test Problem – Structure with geometric and material properties as a function of length L 69

5.17 Wing subjected to an end moment 'T' 70

5.18 Plan-view of the unextended wing configuration divided into 5-segments 72

5.19 2D Beam – 5-element model of the wing in unextended wing configuration 72

5.20 Deflections measured on the 2D beam model of various elements when subjected to an end shear load of 1 lbf 73

5.21 The flowchart to calculate the approximate stiffness of a structure 75

5.22 Plot showing the variation in torsional stiffness as a function of span for various values of extensions 77

5.23 Plot showing the variation in bending stiffness as a function of span for various values of extensions 77

5.24 Static wing divergence speed as a function of span 79

LIST OF TABLES

Table Page

2.1 Bird wing types and flight characteristics 9

3.1 Change in model weight depending on the change in aspect ratio for unextended wing 23

3.2 Change in wing loading depending on the change in chord-length for maximum gross weight obtained for the extended configuration 24

3.3 Wing loading for unextended wing for a constant model weight 24

3.4 Wing loading for gull and inverted-gull wing configurations for constant model weight of 50 oz 25

3.5 Final wing dimensions 25

3.6 Mechanical properties of balsa wood 27

3.7 Results for gravitational loading 34

3.8 Mechanical properties of Delrin 36

3.9 Results of aerodynamic loading 37

3.10 Details of the extension servo motor manufactured by Futaba (part no. S3003) loading 38

3.11 Details of the extension servo motor manufactured by Futaba (part no. S3003) loading 38

3.12 Details of the extension servo motor manufactured by Futaba (part no. S3003) loading 39

3.13 Details of the extension servo motor manufactured by Futaba (part no. S3003) loading 39

5.1 Comparison between the torsional stiffness and the form factor
factor of the same structure but different materials..... 74

CHAPTER 1

INTRODUCTION

1.1 Need For Adaptive Wing Technology

Serious efforts to master the air were initially taken by Leonardo da Vinci towards the end of the 1400s. He systematically studied bird and bat wings and observed their flight. Based on these observations, he first tried to build a man-powered flapping machine. But the first aviation trails were made by Otto Lilienthal in late 1800's. He studied the gliding flight in birds and based on these observations constructed gliding planes similar to today's hand-gliders. Lilienthal was the first to realize the importance of a carefully shaped wing section; he found that the camber and an appropriate thickness of the airfoil improved aerodynamic performance, as compared to a flat plate[1].

In nature, one observes this relationship between the bird wings and their corresponding characteristics to improve the aerodynamic performance of the bird in flight. It is also noted that the large species soar for extended periods of time while small birds have to flap vigorously (high frequency) to remain airborne. The shape of the wing plays an important role in determining the type of flight of which the bird is capable. This restricts the bird in some ways while enhances the bird in others.

The research and development activities in the field of adaptive wing technology continues as new ideas in morphing encompass more than the simple span

extension or wing twisting initially envisioned. It is a common knowledge that along a complete mission flight profile of an aircraft, the vehicle is subjected to widely varying aerodynamic conditions as shown in Figure 1.1; thus traditional vehicle designs are essentially a compromise on aircraft performance due to the conventional fixed wing design. This is so because the design of the traditional aircraft is optimized about a single operating point/regime (for e.g. cruise or loiter, depending in what phase the aircraft would spend most of its time), which leads to a sub-optimal performance at the off-design flight profile.

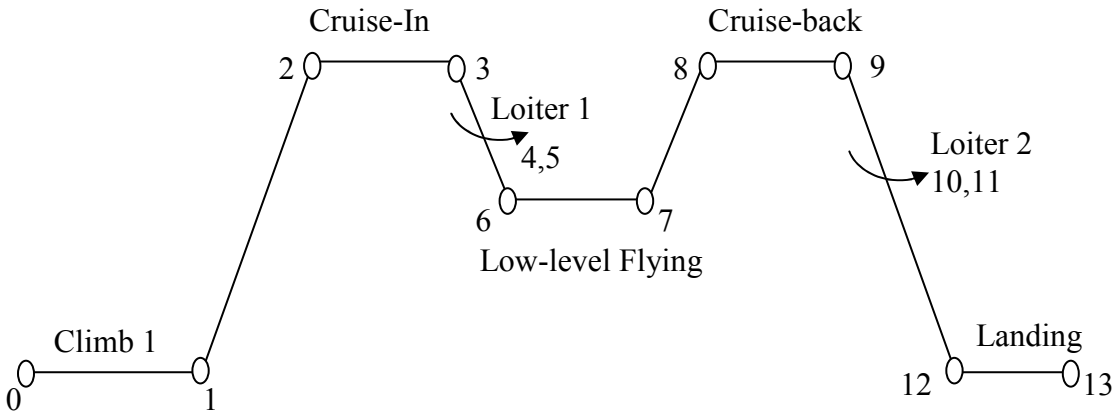

Figure 1.1: A multi-mission aircraft sortie

However, utilizing an adaptive wing technology by emulating the nature (birds wings, biomimetics); the wing geometry can be adjusted to the changing free-stream and load conditions. Thus, allowing one to fully explore the flow potential at each point of the flight envelope (including the off-design points) and optimize the flight dynamics to a greater extent. As seen in the contemporary aerospace industry, this implementation is standardized in the form of flaps which change the wing area as well as the effective camber of the wing.

1.2 Related Work

A morphable/adaptive wing is the one that can changes its geometry to accommodate multiple flight regimes. The ideal use of an adaptive strategy allows the wing to vary its geometric parameters in flight during encounters in situ of changing flow conditions such as wind speed or direction. Several approaches have been proposed over the years both in theory and in experiments that try to emulate bird wing characteristics[3-13]. The primary aim of these researchers was to develop different lift generating mechanisms which could be broadly classified as fixed wing and rotorcraft morphing approaches. Another approach towards the lift generating mechanisms is being investigated through the flapping wing technology. The following work derives inspiration from the fixed wing approaches.

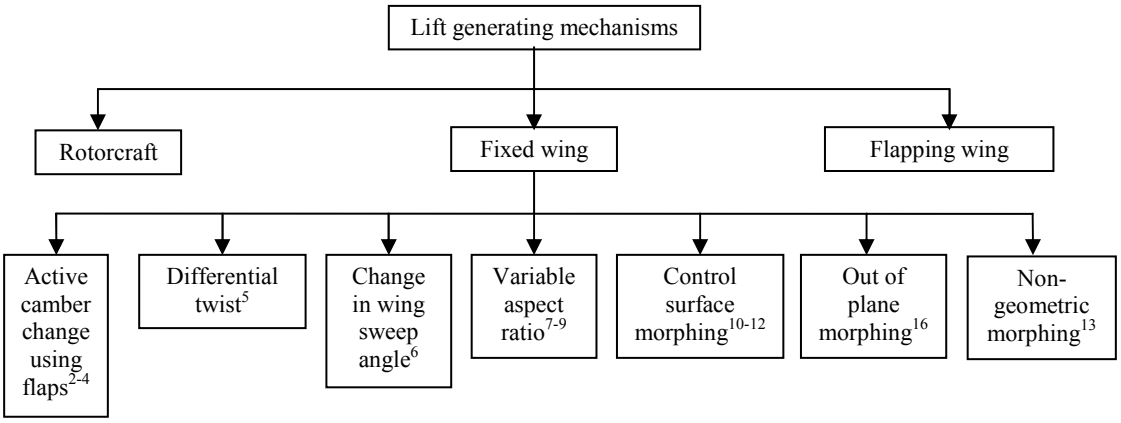

Figure 1.2: Broad classification of lift generating mechanisms

Some of these approaches as summarized in the above figure are an active camber change using flaps, a differential twist wing so that each airfoil cross-section would see a different angle of attack, wing sweep change, span-wise extension i.e. a variable aspect ratio wing, control surface morphing using piezoelectric materials, out-

of-plane morphing such as the gull and the inverted-gull configurations, and also using fluid jets (non-geometric morphing) to modify the aerodynamics of the aircraft.

In camber change, the adaptive airfoil can change camber to obtain a desired lift thus eliminating the need for conventional control surfaces[2-4]. In morphing via a differential twist wing, the wing is configured to optimize the twist angle to obtain low-drag and high-lift aerodynamic characteristics [5]. The wing sweep change is designed to change the wing configurations to suit the various flight conditions [6]. A variable aspect ratio wing would try to incorporate the high speed and maneuverability benefits of low aspect ratio wings, and increased range and fuel efficiency from the large aspect ratio ones[7-9]. The adaptive morphing using smart materials investigates the aerodynamic conditions by modifying the boundary layer characteristics of the fluid flow over the wings[10-12]. A similar inspiration seems to support the research using fluid jets on the wing surface[13]. This would fall under the category of non-geometric morphing wing.

Adaptive wings offer many benefits[14-15], but a viable wing will require research in several areas, including section of initial and perturbed airfoil shapes, steady and unsteady aerodynamic analysis of adaptive airfoils, and method of real-time shape control of an adaptive wing system. Aerodynamic performance and stability should be considered in the context of structural integrity and aeroelasticity. Also most of the above discussed approaches do not build ailerons, which could otherwise be used for flutter control (by symmetrically deflecting both the ailerons). An investigation of dynamic aeroelastic instability is a very important aspect for the wing morphing technology. The flexibility induced in the structure due to the morphing mechanism

may lead to more intense aeroelasticity problems. Efficiency, maneuverability, control, weight and cost could be the possible good indicators to discuss the viability of the adaptive wing design.

In this work, we focus on the design and development of mechanisms for a single morphable wing to emulate most of the characteristics of the bird flight. Thus, we suggest a design to optimize the flight characteristics with the dynamic change of wing structure during flight. The inspiration for this work is to build a single wing with the capability of a variable aspect ratio along with the out-of-plane morphing to a gull and an inverted-gull configuration. In spirit, this work is similar to the work carried out in Ref. [16], although the emphasis here is a systematic wing design and flight performance characterization. Further, Ref. [16] study a different mechanism for gull wing morphing as well as differential twist in wings for a Micro Air Vehicle (MAV) while the current work only focuses on differential telescoping and gull wing morphing. In addition, the wings are intended to be used in a small sized almost ready to fly aircraft that's significantly bigger than the MAV and has different actuator requirements.

The wing design and the mechanisms are considered towards the development of an experimental setup to determine the aerodynamic benefits of morphing. Here, we do not claim the optimality of the morphing solution. By observation of the bird flight, we see that the birds morph their wings to change their flight conditions. This gives us the initial advancement towards the research topic to understand the aerodynamic benefits of wing morphing. Thus, it is not the goal of this research to mimic bird

kinematics. Rather, the objective is to select a biologically-inspired system to improve the range of achievable flying conditions for an unmanned aerial vehicle.

CHAPTER 2

BIOLOGICAL MOTIVATION

2.1 Bird wing shapes and aspect ratio

Inspiration from the bird flight has been largely evident in the designs of the early aviators. The wing and tail shapes they chose were very similar to the planform of the bird wings. The first significant use of adaptive wing technology was developed and used by the Wright Brothers in their *Wright Flyer* aircraft. They incorporated a rigid frame covered in a cloth skin, which along with the shape resembled the wings of a bat at large. Their wing warping concept was the first effective element of lateral control, essentially changing the camber of the aircraft wing to increase or decrease lift.

While warping worked for the relatively light and flexible aircraft of the earlier days, the current aircraft design scenario has been widely changed owing to the varied aerodynamic conditions seen by today's aircraft operating typically at very high Reynolds number. The contemporary aircrafts carry more weight and fly at a faster speed and thus stronger wings have been developed over the time to accommodate these requirements. The revelation during the First World War that thicker airfoil sections were better at creating lift than the thin profiles used at the time also gave aeronautical engineers more leeway in designing wings with greater stiffness and length. Thus, a decade after the first flight inspired from nature was made, the idea of biomimetics as a solution to the large scale practical application in the aerospace industry lost its pace.

Conversely, for the class of small scale vehicles operating at lower speeds would resemble similar aerodynamic conditions as seen by the birds. With the miniaturization of electronics and development of the small scale air-vehicles, there has been an increased research interest towards the low Reynolds number applications in a multi-mission vehicle having a close similarity between the birds flight. The Figure 2.1 shows the important bird wing shapes. Shape and aspect ratio of the bird wing are its most important characteristics that birds modify to suit the flight phase. Amongst birds there are five main kinds of wing types that the majority of birds use, although in some cases wings may fall between two of the categories. These types of wings are elliptical wings, high speed wings, high aspect ratio wings and soaring wings with slots. Additionally, the wing loading for small birds is less than that for large birds[18].

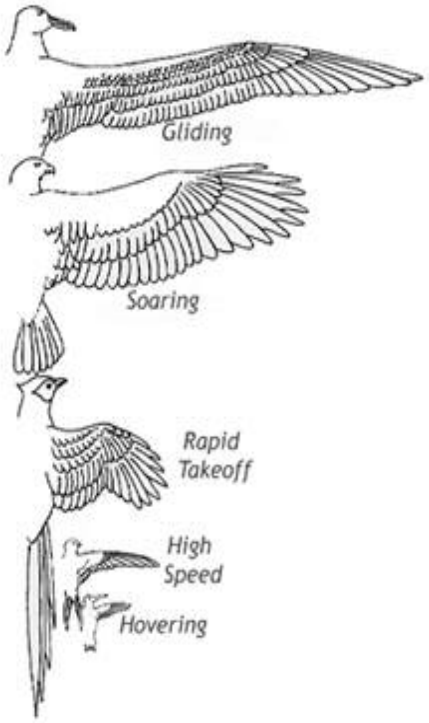

Figure 2.1: Bird wing shapes and aspect ratio

The birds employ an adaptive wing technology to suit their varying aerodynamic needs. By adaptive wing technology, we indicate their change in the wing shape as well as the aspect ratio. The idea here is to develop an aircraft wing using this biological motivation from birds to re-optimize the flight performance to suit the varied aerodynamic conditions experienced in multi-task mission.

Table 2.1: Bird wing types and flight characteristics

Sr. No	Wing Type	Characteristics
1.	**short, broad**, cupped wings	**rapid takeoff** and short-distance flight
2.	shorter and broader wings with slotted primary feathers	soaring flight
3.	flat moderately long, narrow, triangular wings	high-speed flight
4.	large, distinctly arched wings	flapping flight
5.	**long, narrow, flat** pointed wings	**gliding** flight
6.	pointed, swept-back wings	hovering or motionless flight

To summarize, the above Table 2.1, discusses the bird wing shapes and their flight characteristics. The table shows a variety of morphing techniques employed by the bird wings to accomplish dynamic maneuvering and stabilization. The highlighted wing types correspond to the various flight phases that a typical combat vehicle is subjected to. Rapid take-off, soaring at high altitudes, steep-descend flight, slow low-level flying conditions and, short and sudden landing are the conditions aimed to be emulated via a single morphable wing. The above mentioned wing characteristics and the wing shapes, along with the aimed flight conditions lead us to the biological motivation from the flight phases of a seagull.

2.2 Seagull Flight

The seagulls have been a biological inspiration due to its observed flight characteristics like the rapid take-off, soaring at higher altitudes, faster steep descend and slow low level flying. The case of a differential wing extension is one of the important flight phases observed in the seagull sortie to obtain a roll-control authority. These variable characteristics are most desirable for a UAV being developed for surveillance and reconnaissance missions.

The following are the wing shapes observed at the above mentioned flight phases. The visual illustrations accompanying the description of the wing shape are provided by *www.AcclaimImages.com*.

Figure 2.2: Seagull taking-off

1. TAKE-OFF *(figure 2.2)*
    a. higher angle of attack
    b. slight gull configuration
    c. short and high frequency flapping

Figure 2.3: Seagull soaring at higher altitude

2. SOARING (at higher altitude) *(figure 2.3)*

    a. long and stretched out wings, hence a higher aspect ratio

    b. wings slightly above the body of the bird

    c. wings in a smaller gull configuration

    d. lower angle of attack


Figure 2.4: Seagulls displaying its wing shape during steep descent

3. STEEP DESCENT *(figure 2.4)*

    a. wings pointing downward and slightly swept forward (left picture) and showing slight inverted-gull configuration (right picture)

    b. negative angle of attack

    c. wings stretched out

Figure 2.5: Seagull in a low altitude flight preparing to stoop down

4. LOW ALTITUDE FLIGHT (slow and low level flight) *(figure 2.5)*

    a. wings are not completely stretched out i.e. wingspan is short and hence comparatively broader

    b. wings in complete gull configuration (inverted 'V') or an inverted 'L' type configuration

    c. slightly higher angle of attack

Figure 2.6: Seagull preparing to land

5. LANDING *(figure 2.6)*
    a. higher angle of attack
    b. gull configuration
    c. slower flapping
    d. legs stretched out

Figure 2.7 shows a Seagull showing the Differential Wing Extension. The right-side wing is completely stretched out versus the left-side wing curled inward. Here, the seagull is preparing to turn left.

Figure 2.7: Seagull showing differential wing extension

In the seagull, the gull-wing action depends on a set of parallel bones connecting the shoulder and elbow joints of a bird wing[17-18]. A rotation of the shoulder joint in the vertical plane results in an extension or contraction of the entire wing. The skeletal mechanism provides a geometric ratio between the extension of the inner and outer bones. Such a mechanism allows the bird to morph into a variety of positions using a single movement. Each of the positions is largely stable and affords a unique capability within the flight envelope. The purpose of this variable gull-wing action in birds is likely for a variety of reasons, including static aerodynamic[4], physiology, and for flapping control. However, it is studied here solely to investigate the quasi-static aerodynamic benefit and the corresponding effect on the vehicle dynamic response. This type of morphing is considered on a small aerial vehicle, exploring the potential benefits to the cruise, steep descent, and approach phases of flight.

The above discussed flight conditions and the observed wing characteristics provide an initial starting point for implementing morphing on a small vehicle. With the knowledge of the background work and a careful study of the bird wing characteristics, we derive the motivation for our work from the seagull flight to be applied to a fixed wing aerial vehicle to be able to optimize its flight performance for varied aerodynamic conditions. Such vehicles would typically find applications in reconnaissance missions for agriculture, forests, military, etc., and unmanned warfare, and many more.

To summarize, the thesis objectives are proposed as follows:

- Conceptual design and development of mechanisms for a wing to be able to change its span through telescopic extension and perform out-of-plane morphing into gull and inverted-gull configurations.
- Rigorous structural analysis to determine the wing loading characteristics to size the wing and mechanism components, and vibrational analysis to avoid resonance conditions.
- Computational approaches to study the changes in lift, drag and pitching moment due to variable aspect ratio and further extend the studies to the gull and the inverted-gull configurations.
- Comparison of the above computational results with the observed seagull flight to understand the aerodynamic benefits of morphing.
- Static wing divergence speed calculations for a wing with non-uniform structural and material properties as a function of span

In the following chapter 3, we focus on the mechanism design and development and structural and vibrational analysis of the wing structure. Followed in chapter 4, is the discussion on the preliminary computational aerodynamic analysis and a comparison of these aerodynamic results with the seagull flight phases. In chapter 5, a systematic method has been derived to approximate the static wing divergence speed for wing with the structural and geometric properties as a function of span. And finally we summarize our work in chapter 6 and also mention the future aspects of research based on the obtained analysis.

CHAPTER 3

WING DESIGN AND ANALYSIS

3.1 Morphing Mechanism Conceptualization

Owing to the material differences in the natural and engineered systems, the design of a biological-inspired aircraft possesses considerable challenges to the aircraft designer. The birds employ a structure of hollow bones, flexible joints and muscles, and feathers to morph their wings to suit the desired flight condition[17-18]. While the aircrafts use the rigid joints and structures to sustain the aerodynamic loading. With this underlying difference between the two systems and the aim of this research work being to understand the aerodynamic benefits of morphing wings, it is not desired to exactly emulate the bird wing kinematics. Rather, the objective is to devise a mechanism to emulate the bird wing shapes and aspect ratios for quasi-steady aerodynamic analysis using computational and experimental setups.

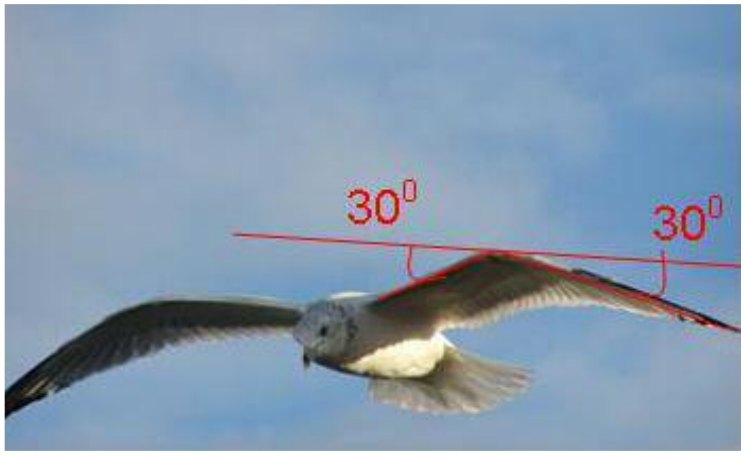

Figure 3.1: Seagull distinctly showing the two limbs of its wing in a gull configuration

Deriving inspiration from the seagull wings two-limb structure follows the design and development of a simple two-link mechanism:

- Shorter and broader wings for rapid takeoff and short-distance flight, and
- Moderately long (and thus comparatively narrower) wings for gliding-flight.

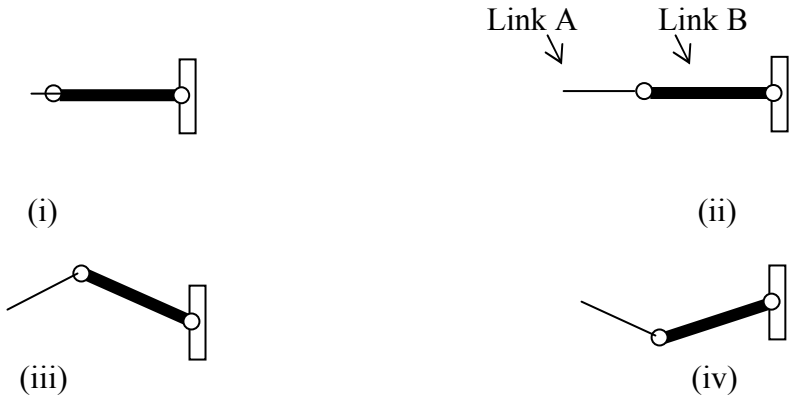

Figure 3.2: Preliminary Mechanism Configurations (i) Un-extended Short and Broad Wing, (ii) Telescopically extended long & (comparatively) narrow wing, (iii) Gull Wing Configuration, (iv) Inverted-Gull Wing Configuration.

The above figures show the desired four configurations of the UAV wing. Link-A and link-B are the two links of the mechanism emulating the two-limbs of the seagull wing. Link-B is a hollow structure able to incorporate link-A. When link-A is stowed inside link-B, we have the first case of a short and a broad wing used by birds typically for a rapid takeoff and a short-distance flight. This is the "Unextended-Wing" configuration. It is to be noted that this wing configuration will have the least aspect ratio for this UAV. *Such a configuration is observed in the seagull wings during take-off*. The following figure shows the unextended wing configuration modeled in CATIA V5 R15. Link-A has been termed as the extendible wing which is stowed inside the main wing i.e. the link-B.

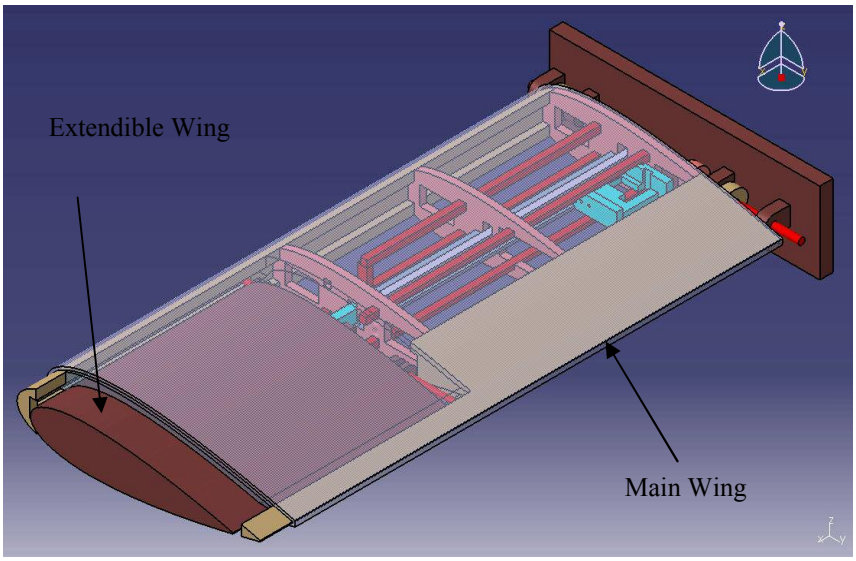

Figure 3.3: Case 1 – Unextended wing configuration

The morphable wing's two-link structure is telescopic in nature. The telescopic actuation is performed by a linear actuator consisting of a rack and pinion arrangement driven by continuous rotation (speed controlled) servo motor, thus changing the shorter and broader wings to moderately long. The cross-sectional area remains almost constant but the aspect ratio does change due to the telescopic action. This forms the second case of our study i.e. is the "Extended-Wing" configuration, *typically used by birds for gliding flight*. Thus we obtain a variable aspect ratio wing. It is one of the objectives of this research to observe the changes in the aerodynamic loading due to a dynamic change in the wing aspect ratio. The figure 3.4 shows the extended wing configuration modeled in CATIA V5 R15. The extendible wing is in its extreme position and thus has the highest aspect ratio. The figure also shows the ribs and spars that form the basic wing configuration. The fuselage forms the fixed end of the wing. The locations for the servo motors used to obtain the extension as well as the gull mechanism have been specified in the figure 3.4.

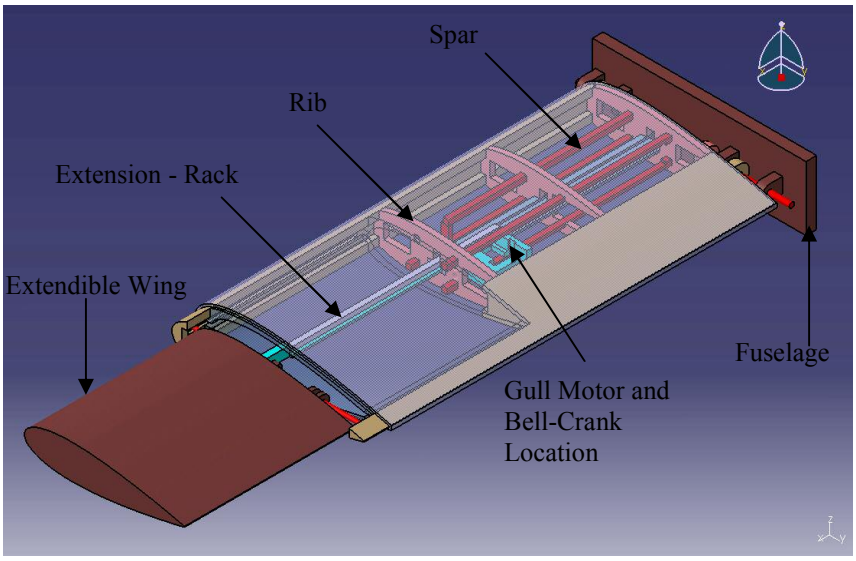

Figure 3.4: Front-isotropic view of the extended wing configuration

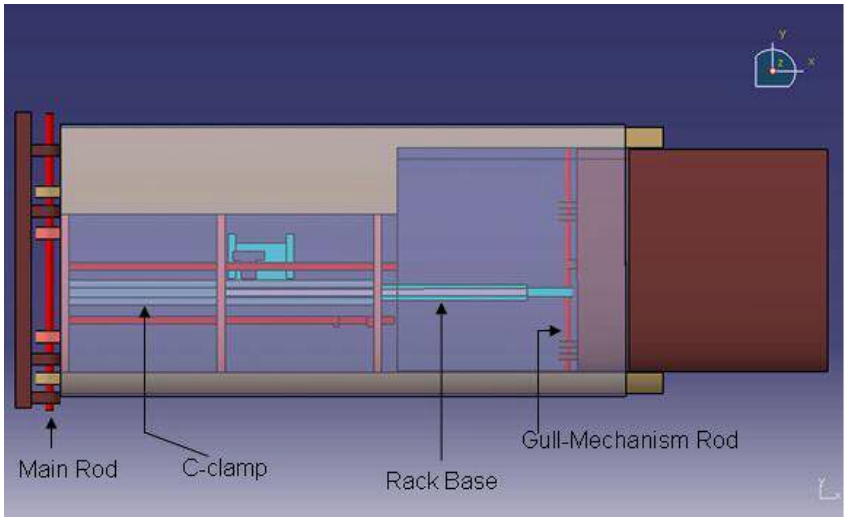

Figure 3.5: Top view of the wing showing 75% extension

The telescopic extension is achieved through a rack and pinion arrangement driven by a servo motor. As shown in the above figure, the rack is placed on the rack base which is held secured in a C-clamp, whose cross-section is like a 'C' (Also see Appendix A). Figure 3.7 shows the rack base which also houses the space for the gull-mechanism's servo motor and bell-crank type arrangement, which would move with the

telescopic extension of the wing. The main rod and the gull-mechanism rod form the rotational joints of this wing structure.

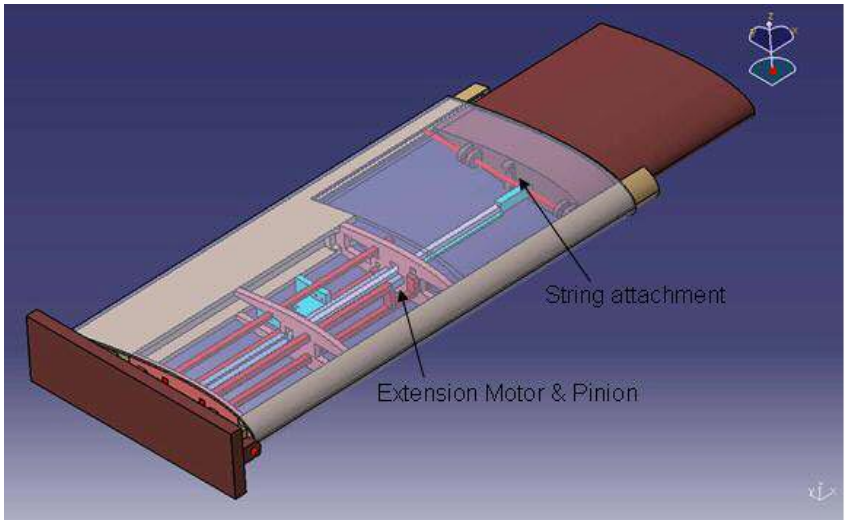

Figure 3.6: Rear-isotropic view of the wing showing 75% extension

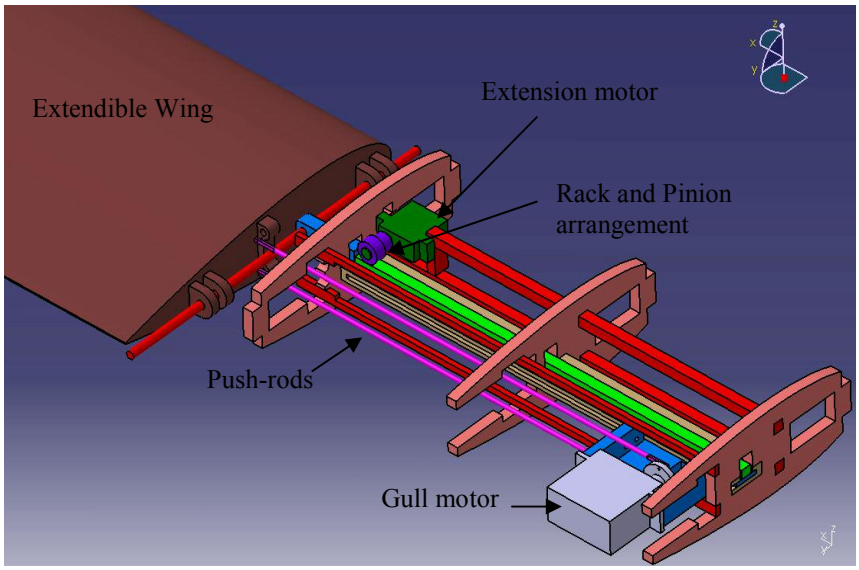

Figure 3.7: Telescopic and gull mechanism

It is also observed that for a seagull when in the gull configuration, the angle between the two limbs of the seagull wing is approximately 30^{o} (see Ref. [17-18]). To morph the aircraft wing to the further extremities of the "Gull" and "Inverted-Gull"

configurations, we have used a push-rod and a bell-crank type of an arrangement driven by the gull-mechanism servo motor.

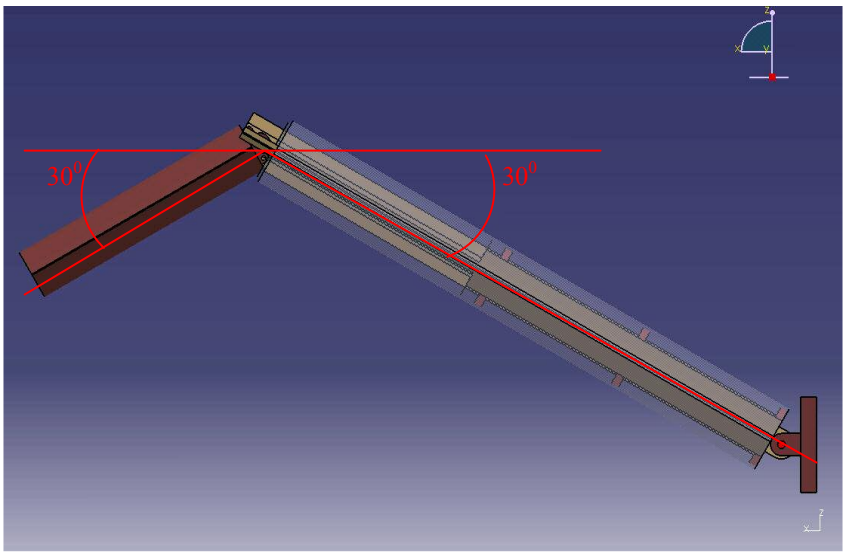

Figure 3.8: Gull wing configuration

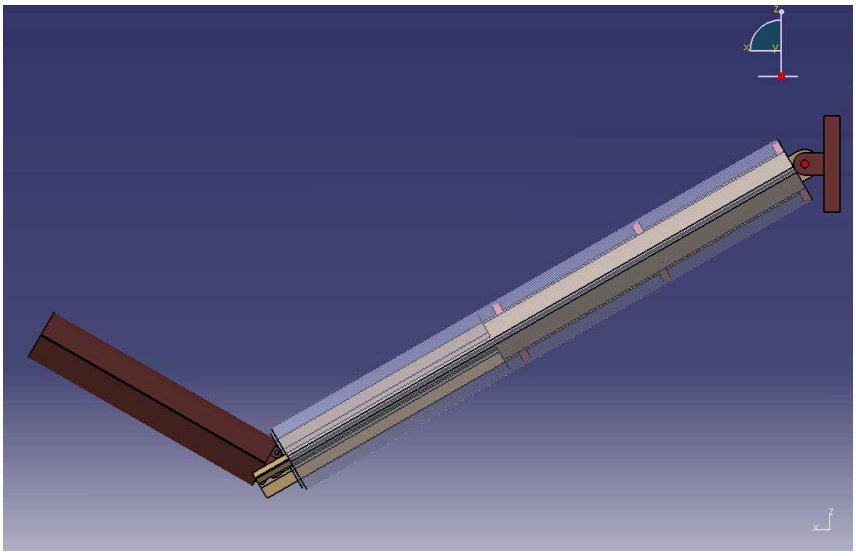

Figure 3.9: Inverted-gull wing configuration

Thus a relative motion between the two links of the mechanism is achieved and the angle between the outer main wing and the inner extendible wing can be varied by the push-rods and a servo motor through ±60 degrees. Also, the angle between the outer

wing and the aircraft structure can be varied by using a bevel gear-set, where the outer wing angle would vary from ±30 degrees with respect to the aircraft's fixed fuselage.

The 3D models have been created in CATIA V5 R14 as shown in figures 3.8 and 3.9. The model is simulated using the I-DEAS NX11 - Mechanism Module to verify the required degrees of freedom for the mechanism to operate.

3.2 Design Constraints And Preliminary Structural Analysis

While the primary reason to develop an adaptive wing is the aerodynamic benefits[14-15], the primary hindrance is the structural and vibrational considerations due to the unsteady nature of the airflow during the flight. And, hence this analysis forms an important part of the morphable wing technology.

The preliminary construction is to be tested in the low speed subsonic wind-tunnel and as such based upon the tunnel dimension (width – 36 inches, height – 24 inches and length – 72 inches) the maximum semi-wingspan of the wing was limited to 30 inches to avoid the wall effects of the wind tunnel. The outer wing thus measures up to 20 inches and the inner (telescopic/extendible wing) measures 10 inches span wise. Thus the wing would span 40 inches for the first case of unextended configuration and would approximately span 60 inches for the extended configuration. The wing loading for model aircrafts of this size is typically about 18 - 24 oz/sq. ft. A value of 20 oz/sq. ft. is assumed initially for design consideration.

Based on the methodology outlined in Ref. [19] and the density of air, the preliminary sizing is carried out.

Table 3.1: Change in model weight depending on the change in aspect ratio for unextended wing

Span (S_{UE})	**Aspect Ratio (AR_{UE})**	**Chord Length (c)**	**Wing Area (A_{UE})**	**Wing Loading (WL_{UE})**	**Model Weight (W)**
inch		**inch**	**sq. inch.**	**oz./sq. ft.**	**oz.**
40	4.45	8.99	359.99	20	49.99
40	5	8	320	20	44.44
40	6	6.67	266.67	20	37.03
40	7	5.71	228.57	20	31.74

From the above table we see that for an aircraft with a 40 inch wingspan, when the aspect ratio is varied from about 4 to 7 and for a given wing loading condition, the maximum gross weight of the aircraft that the wing would support cannot exceed about 50 oz.

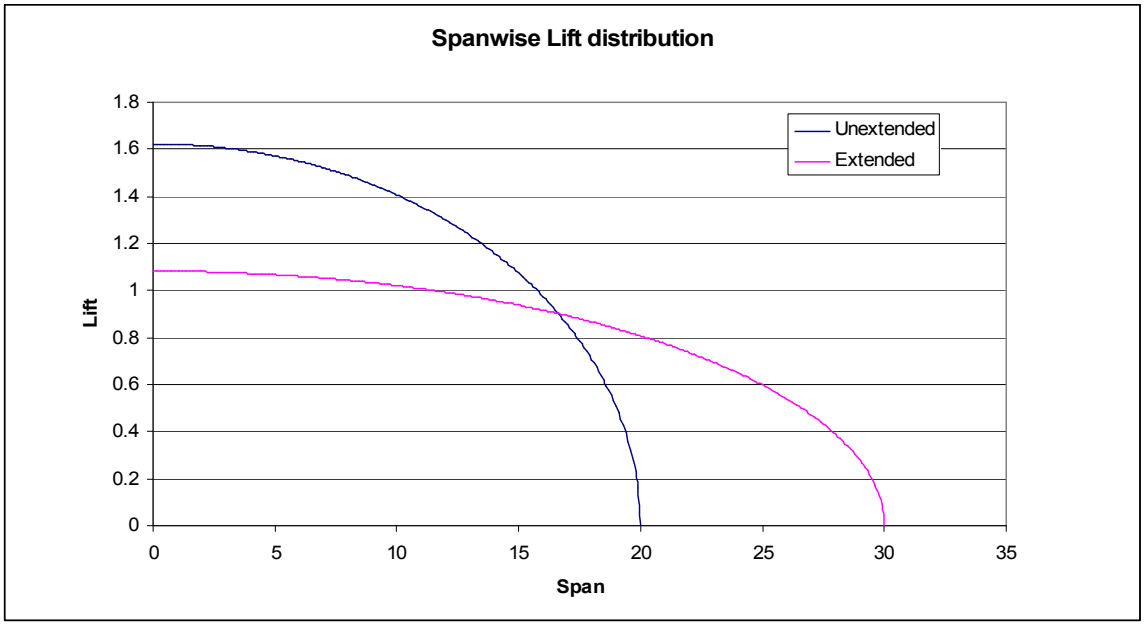

Figure 3.10: Spanwise lift distribution for the unextended and extended wing configuration

The area under the lift distribution is equal to the total lift produced by the morphing wing. To obtain the same lift, the lift per unit span decreases was the

wingspan increases. And thus, we see a decrease in the wing loading experienced by the wing in the extended configuration.

When the aircraft would undergo the telescopic extension and increase the wingspan to 60 inches, it would achieve a higher aspect ratio. Keeping the chord lengths constant for the earlier table 3.1, but increasing the span to 60 inches we see an increase in the aspect ratio by about 2.5 to 3.5 for each case. And, assuming the model weight to be about 50 oz, we see the least wing loading would be experienced for the first case

Table 3.2: Change in wing loading depending on the change in chord-length for maximum gross weight obtained for the unextended configuration

Span (S_E)	**Chord Length (c)**	**Aspect Ratio (AR_E)**	**Extended Wing Area (A_E)**	**Model Weight (W)**	**Wing Loading for Extended wing (WL_E)**
inch	**inch**		**sq. inch.**	**oz.**	**oz./sq. ft.**
60	8.99	6.67	539.99	49.99	13.33
60	8	7.5	480	49.99	14.99
60	6.67	9	400	49.99	17.99
60	5.71	10.5	342.85	49.99	20.99

A similar procedure is applied to calculate the wing loading conditions for the gull and the inverted-gull configurations. The table below summarizes the wing loading experienced at various aspect ratios when the gross weight is assumed to be 49.99 oz.

Table 3.3: Wing loading for unextended wing for a constant model weight

Span (S_{UE})	**Aspect Ratio (AR_{UE})**	**Chord Length (c)**	**Unextended Wing Area (A_{UE})**	**Model Weight (W)**	**Wing Loading for Unextended wing (WL_{UE})**
inch		**inch**	**sq.inch**	**oz.**	**oz/ft^2**
40	4.45	8.99	359.99	49.99	20
40	5	8	320	49.99	22.50
40	6	6.67	266.67	49.99	26.99
40	7	5.71	228.57	49.99	31.50

Table 3.4: Wing loading for gull and inverted-gull wing configurations for constant model weight of 50 oz

Span (S_E)	**Aspect Ratio (AR_E)**	**Extended Wing Area (A_E)**	**Wing Loading for Extended wing (WL_E)**	**Wing Area in gull configuration (A_E)**	**Wing Loading for gull wing (WL_E)**
in		**in^2.**	**oz/ft^2**	**in^2**	**oz/ft^2**
60	6.67	539.99	13.33	473.67	15.20
60	7.5	480	14.99	421.05	17.10
60	9	400	17.99	350.87	20.52
60	10.5	342.85	20.99	300.75	23.94

In the above tables, we see that the projected wing planform area (A_{UE}) for an unextended wing is the lowest resulting in an increased wing loading (WL_{UE}). But with the increase in aspect ratio due to telescopic extension we see a corresponding decrease in the wing loading WL_E for the extended wing configuration. The wing planform area (A_G) for the gull and inverted-gull configurations reduces since the projected area is the cosine of the extended wing area due to the wing rotation i.e. due to the out-of plane wing morphing. Consequently, as seen in the first case on the table, the wing loading increases from 13.33 oz/ft^2 for the extended configuration to 15.20 oz/ft^2 (WL_G) for the gull and the inverted-gull configurations. From the above table, it is also observed that the least wing loading condition is seen in the first case (when the aspect ratio is approximately 4.45 for the unextended wing configuration). Thus the dimensions for the wing were finalized to be:

Table 3.5: Final wing dimensions

Unextended Wing Span	40 inches
Extended Wing Span	60 inches
Chord Length	9 inches
Gross Weight of the Model Aircraft	50 oz

Further, we note that sea-gulls typically fly at a speed ranging between 15 to 38 mph (see Ref. [17-18]) and a design flight speed of 33 mph was chosen. This information was additionally used to size the wing structure based on the knowledge of basic principles of design.

Note, while the aspect ratio is varied from 4.45 to 8 (morphing strategy), the wing with aspect ratio 4.45 is the broader one capable of supporting the model aircraft with more weight (as compared to other initial unextended wing aspect ratios when the wing loading is assumed to be 20 oz/ft^2), resulting in lesser weight restrictions for the model aircraft and also satisfying the first construction requirement of the wing. With a wing loading of 20 oz/sq. ft. and a chord length of 9 inches, the wing is capable of carrying weight up to 50 oz. A thicker profile of NACA 0018 was chosen to incorporate the mechanism inside the wing with a maximum height of the elliptical cross-section of 1.62 inches.

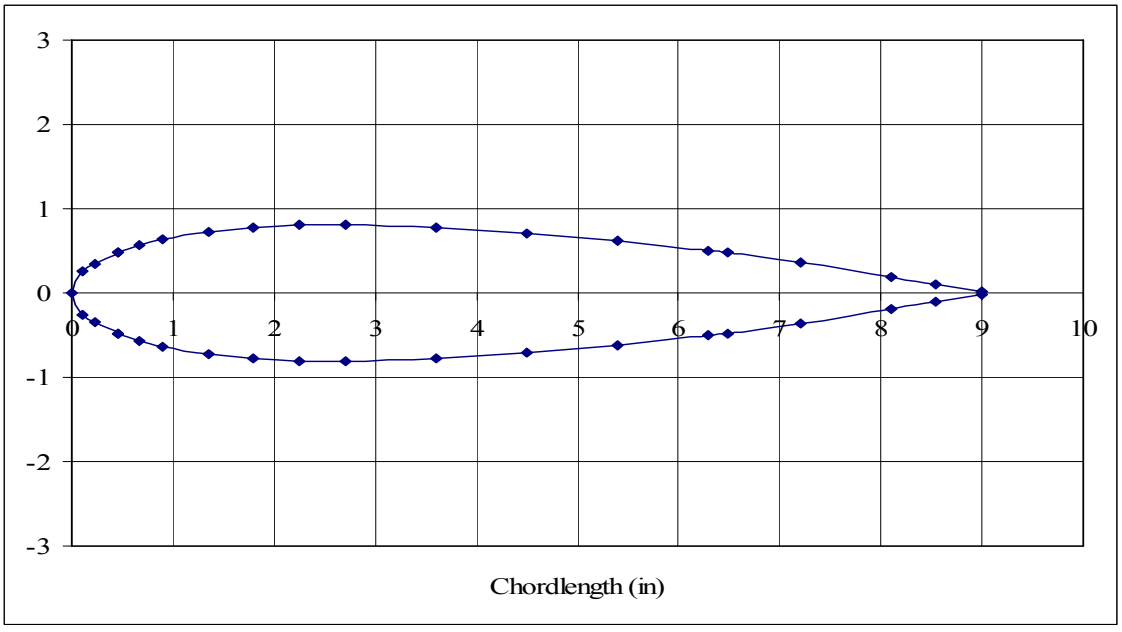

Figure 3.11: Airfoil - NACA 0018

During the linear actuation of the telescopic wing, the wing planform area increases and consequently the wing loading decreases, until it reaches the least value of 13.33 oz/ft^2, when the semi-wingspan equals 30 inches. The angle made by the limbs of typical sea-gull wing is approximately 60 degrees (see Ref. [17-18]). The mechanism is designed to incorporate this angle between the two links and consequently the angle between the outer wing and the aircraft body is assumed to be 30 degrees. When the wing forms the gull or the inverted gull configurations, the wing loading reduces to 15.2 oz/ft^2, which is less than the design wing loading value.

Further, the material is chosen to be Balsa Wood. The following table summarizes its mechanical properties.

Table 3.6: Mechanical properties of balsa wood[20]

Material: Balsa Wood	Low Density	Medium Density	High Density
	lbf/in^2	lbf/in^2	lbf/in^2
YS (Compressive)	680	1750	2830
YS (Tensile)	1100	2890	4670
Elastic Modulus - Compression (E)	56400	66700	77000
Weight Density *(lbf/in³)*	0.0027	0.0054	0.0081
Shear modulus of elasticity, G	15700	23600	37500

There are actually six Poisson's Ratios for any given piece of wood, depending on the orientation of the grain to the direction in which the load is acting. However, normally we are only concerned with wood in which the grain runs along the long axis of the member. In this case, the relevant Poisson's Ratios are ν_{LR} and ν_{LT}, i.e. tension or compression acting longitudinally with a passive strain in the radial or tangential direction. For balsa, ν_{LR} is 0.23 and ν_{LT} is 0.49. Since one dimensional property along the longitudinal direction is needed, we use $\nu_{LT} = 0.23$.

The preliminary design approach is conservative. An elliptical lift distribution having its aerodynamic center (0.25 times the chord length) of the cross-section was assumed for the structural as well as the actuator calculations of the mechanism.

The subsequent figure 3.12 shows the elliptical pressure distribution that acts on the unextended wing configuration. The area under the curve gives the total lift produced and equals 25 oz, which is half the total gross weight of the model aircraft. This preliminary load data is applied to a simple structural model of the wing built in ANSYS Classic.

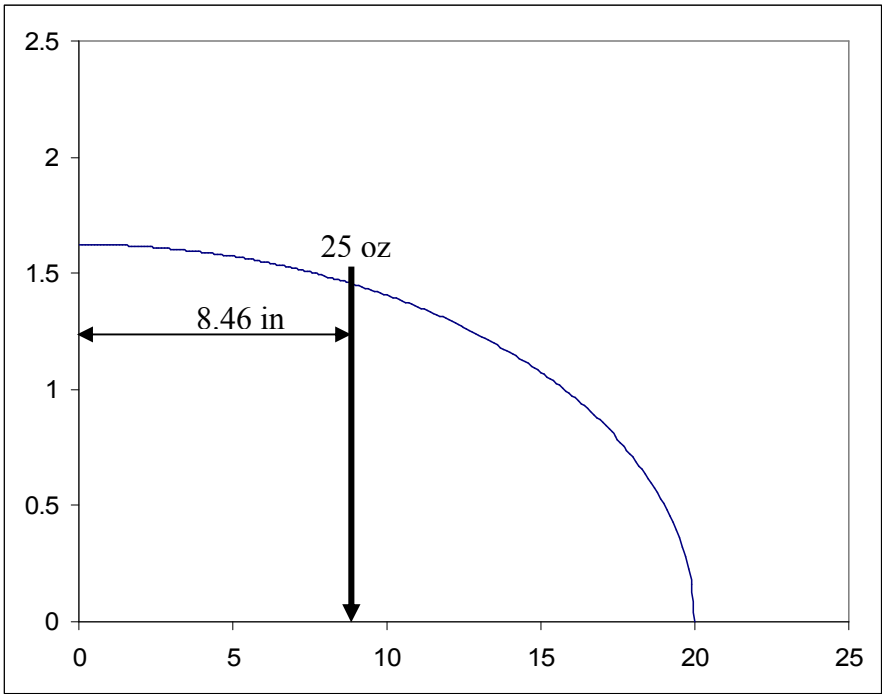

Figure 3.12: Elliptical wing loading at the quarter chord-line along the wingspan for unextended wing configuration

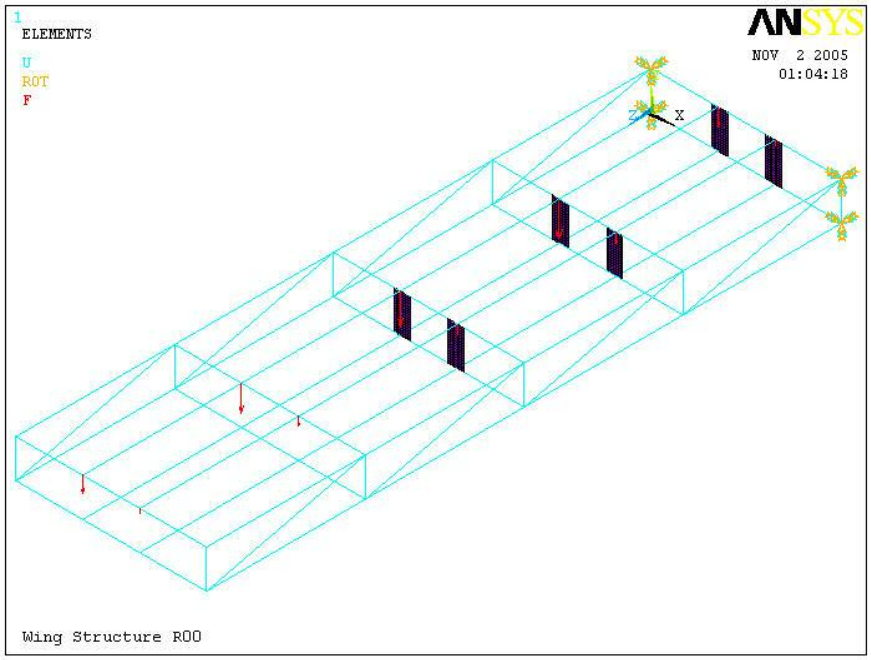

Figure 3.13: Applied boundary conditions for 3D beam elements and plate/shell element.

In the above figure 3.13, the blue lines represent the spar of the wing and are constructed using 3D beam models known as BEAM4 in ANSYS Classic. BEAM4 is a uniaxial element with tension, compression, torsion, and bending capabilities. The element has six degrees of freedom at each node: translations in the nodal x, y, and z directions and rotations about the nodal x, y, and z axes. Stress stiffening and large deflection capabilities are included. A consistent tangent stiffness matrix option is available for use in large deflection (finite rotation) analyses. The black rectangles represent the ribs of the wing and are constructed using 3D plates models known as PLANE183 in ANSYS Classic. PLANE183 is a higher order 2-D, 8-node element. PLANE183 has quadratic displacement behavior and is well suited to modeling irregular meshes (such as those produced by various CAD/CAM systems). This element is defined by 8 nodes having two degrees of freedom at each node: translations in the

nodal x and y directions. The element may be used as a plane element (plane stress, plane strain and generalized plane strain) or as an axisymmetric element. The red arrows depict the load applied over the entire span. This is a good initial representation of the unextended wing.

Note that the free end is kept hollow. The extendible wing would be stowed in this hollow section of the main wing. It would increase the global stiffness to this initial representation. Also, the acceleration due to gravity and the weight of the mechanisms has not been taken into account. Here the, actuator along with its components and the extendible part of the telescopic wing are not modeled. These also add to the global stiffness matrix and thus reduce the deflection and stresses at large. The aim of this initial analysis is to reduce the deflection of the structure under the influence of aerodynamic load alone and optimize the spar and rib sizes with consideration of the space available within the wing. The material used is balsa wood and its commercial availability is also taken into account while modifying the spar and rib sizes in this initial analysis.

The cross-sectional properties of these elements are supplied to ANSYS in terms of real constant sets. Based on some initial calculations and space requirements, the spar cross-section is a square of 0.2 inches and the thickness of the ribs is also taken as 0.2 inches. The deflection at the farthest end after the elliptical loading applied in the above figure was of the order of 0.425 inches for in the unextended wing position and the rotation at the wing base is 1.2174 degrees.

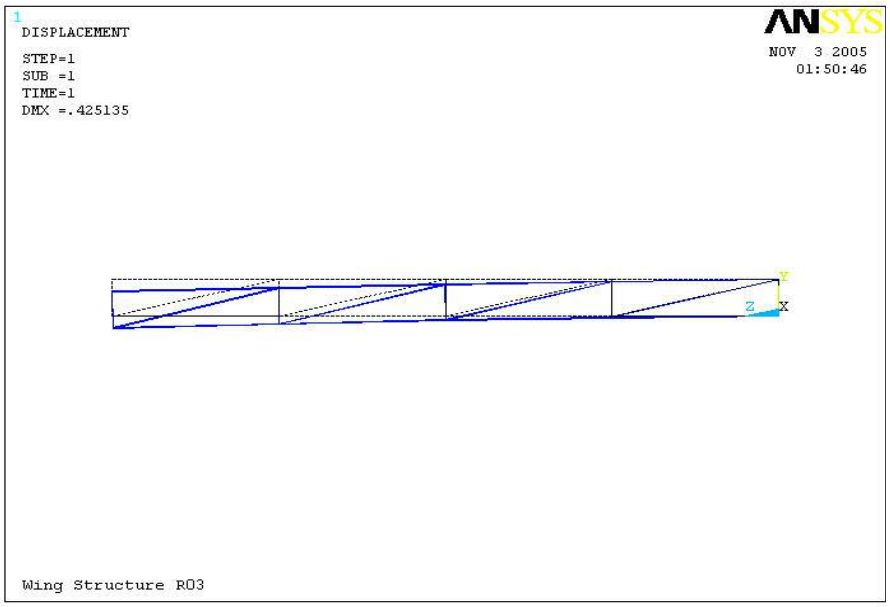

Figure 3.14: 3D spar element model (Maximum Deflection = 0.43 in)

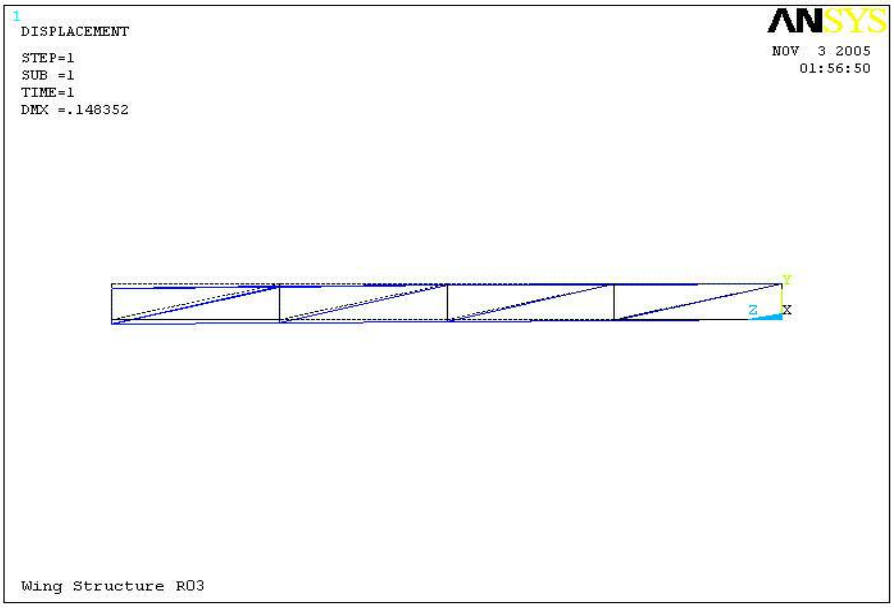

Figure 3.15: 3D beam element model (Maximum Deflection = 0.15 in)

By changing the spar cross-section to a square of 0.25 inches and the rib thickness as 0.25 inches, we see that the deflection reduces to 0.15 inches and the rotation at the wing base reads 0.4250 degrees. Due to the restriction of space within the

wing and the limitation on the gross weight of the entire vehicle, this size of the basic components of the wing showed a considerable reduction in the deflection of the free end. Increment in the cross-section of the spar and the thickness of the rib is done at the commercially available standards of balsa wood which are available as off-the-shelf items in the hobby shops.

3.3 Detailed Structural And Vibrational Analysis

The 3D models, created in I-DEAS NX11 and CATIA V5 R14, were being modified continuously to meet the design requirements. This model is then imported through IGES format to ANSYS workbench for further detailed structural and vibrational analysis. The above figure shows the imported model of the extended wing in ANSYS Workbench.

In this figure, we also see the extended wing support, the part of the wing structure that would support the hollow space in the main wing during the cases of wing extension as well as in the gull and inverted-gull configurations.

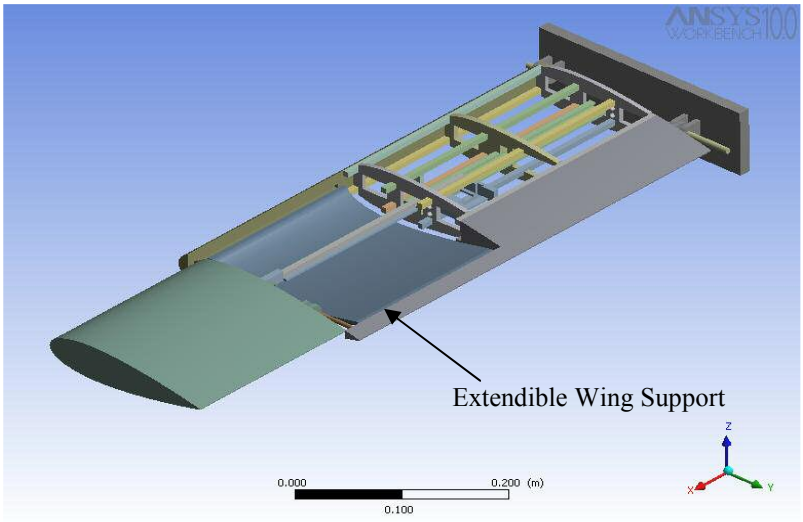

Figure 3.16: IGES format imported in ANSYS Workbench showing arrangements inside wing structure without motors and gear-sets

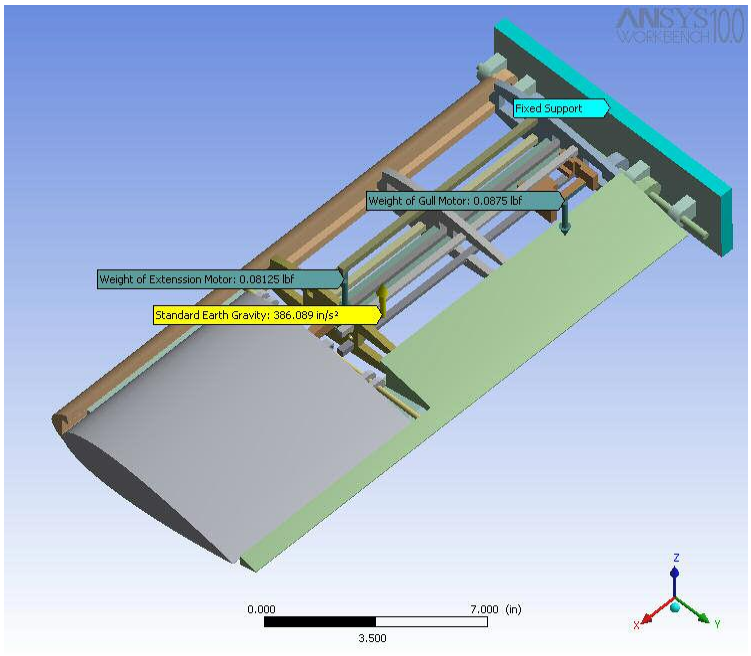

Figure 3.17: Setup environment in ANSYS Workbench for structural and vibrational analysis

The above figure shows the typical environment setup for the analysis of the unextended wing in ANSYS Workbench. The model has been fixed at one end which would be connected to the aircraft fuselage. At the locations specified for the gull mechanism motor and extension mechanism motor, a force has been applied in the negative z-direction representing the weight of these motors. Also, the standard earth gravity has been applied to the entire model.

All the configurations of the wing are tested in a similar setup under the influence of gravity to determine the need to redesign according to the deflection observed. Also, along with the maximum stress and its location, the first frequency of vibration is noted. Since the bending load increases for the extended wing configuration, as expected, a higher value of deflection and maximum stresses has been observed.

The following table summarizes the observations for the above environment in ANASYS Workbench.

Table 3.7: Results of gravitational loading

Wing Configuration	Deflection (inch)	1st frequency of Vibration (Hz)	Max. Stress (psi)	Location of Max. Stress
Unextended	1.60e-002	71.62	62.29	Main Rod
Extended	3.71e-002	47.51	104.52	Main Rod
Gull	2.94e-002	52.76	90.25	Main Rod
Inverted-Gull	2.93e-002	52.82	89.79	Main Rod

It is also observed that the maximum stress is located in Main Rod of the structure and thus would be the part under maximum stress condition due to the aerodynamic loading as well.

Now, along with this initial environmental setup for the wing configurations, the predicted aerodynamic load of elliptical pressure distribution along the quarter chord line i.e. the line along the aerodynamic center of the NACA 0018 profile, is applied and the structural and vibrational analysis is repeated.

The following figure shows the aerodynamic loads applied to the various configurations.

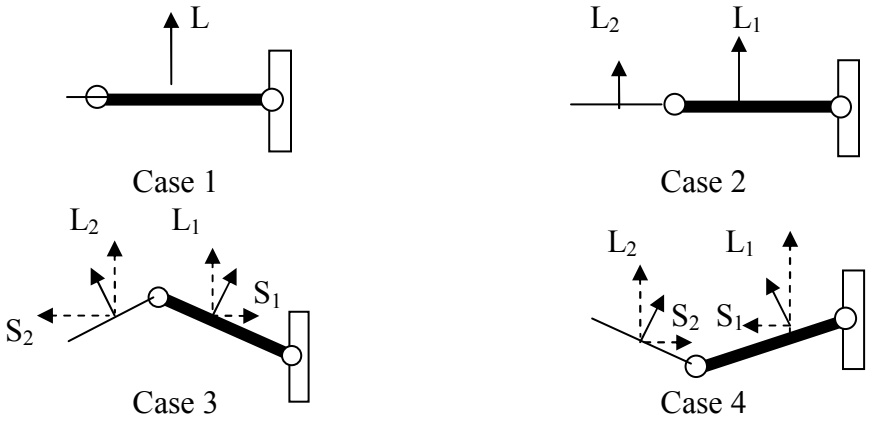

Figure 3.18: Application of aerodynamic loads of lifts and side force on the wing in the above discussed configurations

Figure 3.19 shows the case of static analysis of the unextended wing structure and the telescopically extended wing and figure 13.20 shows gull configuration as well as the inverted-gull configuration were all performed using ANSYS Workbench. As expected, it shows (in red) that the maximum deflection increases from 0.201 inches for the un-extended wing case to 0.639 inches for the case of telescopic extension of the wing. And the rotation at the wing base increases from 0.5758 degrees for the unextended configuration to 1.2193 degrees for total extension.

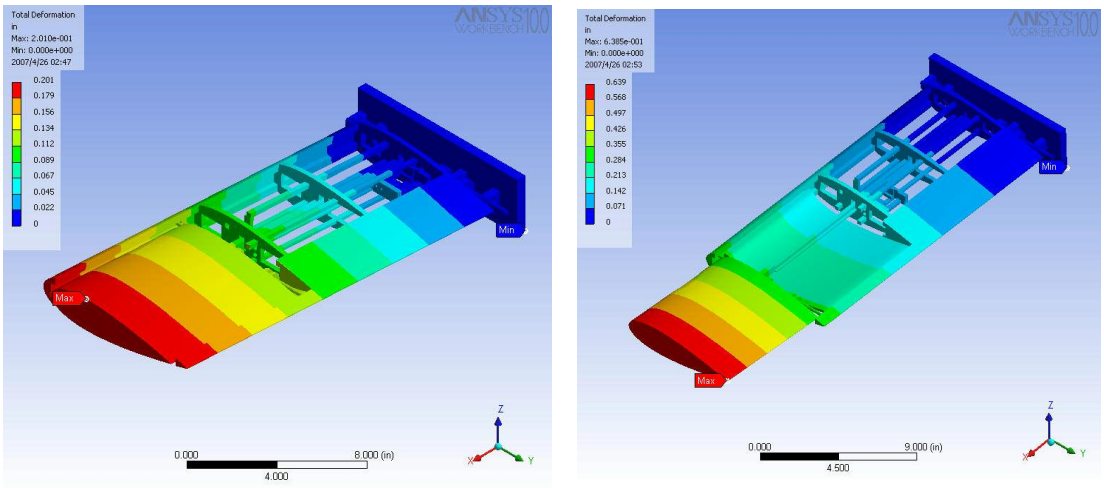

Figure 3.19: Maximum deflection in unextended (left) and extended wing (right) configurations

The area under the lift distribution is equal to the lift produced by the morphing wing. To obtain the same lift, the lift per unit span decreases as the wingspan increases; since the aspect ratio and the wing area increase due to the telescopic extension. But, it is to be noted that the wing-root bending moment increases drastically due to an increase in the wingspan. Thus, the bending moment along the wingspan of the morphing wing is much larger than that of the conventional wing which results in an increase in the deflection of the free-end. The maximum stress for the unextended wing

configuration is 781.81 psi increases to 1238.4 psi for the extended wing configuration. These values are observed for the main rod and the gull-mechanism rod respectively. The maximum tensile strength of balsa wood is 680 psi (compression) and 1100 psi (tensile). Hence, the material of the rods has been changed to Delrin. The gull-mechanism rod measures 0.2 inch while the main rod measures 0.35 inches in diameter.

Delrin is the brand name for an acetal resin engineering plastic invented and sold by DuPont. Delrin is a lightweight, low-friction, and wear-resistant plastic. Other names for this compound include: polyoxymethylene (POM), acetal resin and polytrioxane.

The following table summarizes its mechanical properties of Delrin

Table 3.8: Mechanical properties of Delrin[21]

Material: Delrin	Low Density
	lbf/in^2
YS (Compressive)	18000
YS (Tensile)	10000
Elastic Modulus - Compression (E)	450000
Weight Density *(lbf/in³)*	0.055
Poisson's Ratio	0.35

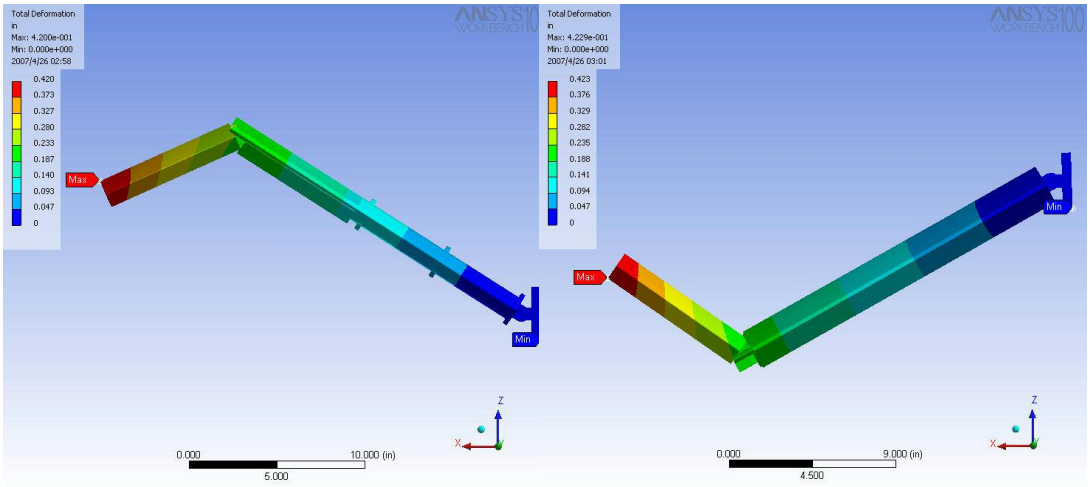

Figure 3.20: Max. deflection in gull (L) and inverted-gull wing (R) configurations

Similar to the above two cases of un-extended and extended wing, the maximum deflection due to the aerodynamic loading for the gull and the inverted-gull configurations are shown in figure 3.19. The maximum deflection obtained is shown in red.

The wing structure is modified at some of the weak components for design safety and stability in vibration. Delrin rods (main rod and the gull-mechanism rod) at the joints have been used to strengthen the member with the most stress concentration. It is to be noted that the stresses encountered in the main rod due to aerodynamic loading exceeds the yield stress (in tension and compression) as specified earlier for the balsa wood. And, hence there is a need to replace these rods with the Delrin rods. Delrin has a higher yield stress in tension as well as compression. The following table discusses the results from the aerodynamic loads of lift and side force on the wing structure, obtained from ANSYS Workbench.

Table 3.9: Results of aerodynamic loading

Wing Configuration	Max. Deflection (inch)	1st mode Frequency (Hz)	Max. Stress (psi)	Location of Max. Stress (Material)
Unextended	0.2010	71.66	781.81	Main Rod (Delrin)
Extended	0.6385	47.56	1238.4	Gull-Mechanism Rod (Delrin)
Gull	0.42	52.902	875.17	Main Rod (Delrin)
Inverted-Gull	0.4230	52.78	967.56	Gull-Mechanism Rod (Delrin)

The forces and moments transferred by morphing the wing dynamically are obtained from ANSYS directly. These results demonstrate the practicality of the structure developed.

Further, the vibration analysis showed that the lowest frequency amongst the above mentioned configurations was 47.56 Hz for the extended wing configuration. Knowing the value for the lowest vibration mode leads one to size the various motors used for the linear as well as the rotational actuation. The motor torques are obtained from the force analysis of the above configurations. Since the choice of speed for motor actuation is not to change the wing shape rapidly but a gradual change so as to avoid any unnecessary excitation of the structural modes and any aerodynamic instability due to morphing, the motors are chosen to be of a lower frequency than the above. The gear-sets were sized on the similar lines. Nylon (plastic) spur rack and pinion suits the purpose of higher strength to weight ratio.

The following are the specifications of the components mentioned above:

Table 3.10: Details of the extension servo motor manufactured by Futaba (part no. S3003)

SERVO for EXTENSION MECHANISM			
Volts	6	4.8	V
Torque	56.9	44.4	ozf-in
Speed	0.19	0.23	sec/60deg
Dimensions	1.6 x 0.8 x 1.4		in
Weight	1.3		ozm
	0.08125		lbm

Table 3.11: Details of the gull-mechanism servo motor manufactured by Futaba (part no. S3010 standard)

SERVO for GULL MECHANISM			
Volts	6	4.8	V
Torque	90.2	72.2	ozf-in
Speed	0.16	0.2	sec/60deg
Dimensions	1.6 x 0.8 x 1.5		in
Weight	1.4		ozm
	0.0875		lbm

Table 3.12: Details of the pinion manufactured by Rush Gears Inc (part no. TP2412)

SPUR PINION		
Diametrical Pitch (= T/d)	24	
Number of Teeth	12	
Pressure Angle	20	deg
Max. Pitch Diameter	0.5	inch
Face Width	0.25	inch
Bore	0.25	inch
Hub Projection	0.31	inch
Hub Outer Diameter	0.39	inch

Table 3.13: Details of the rack manufactured by Rush Gears Inc (part no. TP24DL-2)

SPUR RACK		
Pressure Angle	20	deg
Face Width	0.25	inch
Thickness	0.25	inch
Pitch Line to Back	0.208	inch
Length	24	inch

The completion of the design stage is marked by the systematic sizing of all the components of the wing structure. Now the focus of the work is shifted to the computational aerodynamic analysis of the wing in the four configurations discussed above. And finally comparing of these computational results with the observed seagull flight, we obtain an insight towards the aerodynamic benefits of morphing.

CHAPTER 4

AERODYNAMIC BENEFITS OF MORPHING

4.1 Computational Aerodynamics

The aerodynamic analysis is performed using Athena Vortex Lattice (AVL) developed by Mark Drela, MIT Aero & Astro and Harold Youngren, Aerocraft, Inc., to obtain basic aerodynamic parameters such as the lift curve slope, drag polar and the pitching moment slope as functions of angle of attack. AVL was originally written by Harold Youngren circa 1988 for MIT Athena TODOR aero software collection. A number of modifications have been added by Mark Drela and Harold Youngren, to the point where only a trace of the original code remains.

Conventionally, the aerodynamic characteristics are simplistically modeled as functions of angle of attack to be used later in stability and control analyses as well as flight performance calculations. However with the morphable geometries, it is essential that the aerodynamic characteristics be modeled not only as functions of the angle of attack but also the morphing parameters (such as the angle between the inner and outer wing, wing span, aspect ratio, etc).

To verify the accuracy of the AVL results, the code is executed for the wing surface with various known airfoil sections. The values for co-efficient of lift are noted for every airfoil section at different angles of attack and are compared to the theoretical values of co-efficient of lift for the same airfoil having applied the finite wing

correction. It is observed that for a wing efficiency factor of 0.68, the AVL results are in close correspondence with the theoretical values. The code is executed for an air flow speed of 580.8 in/sec i.e. 33 mph.

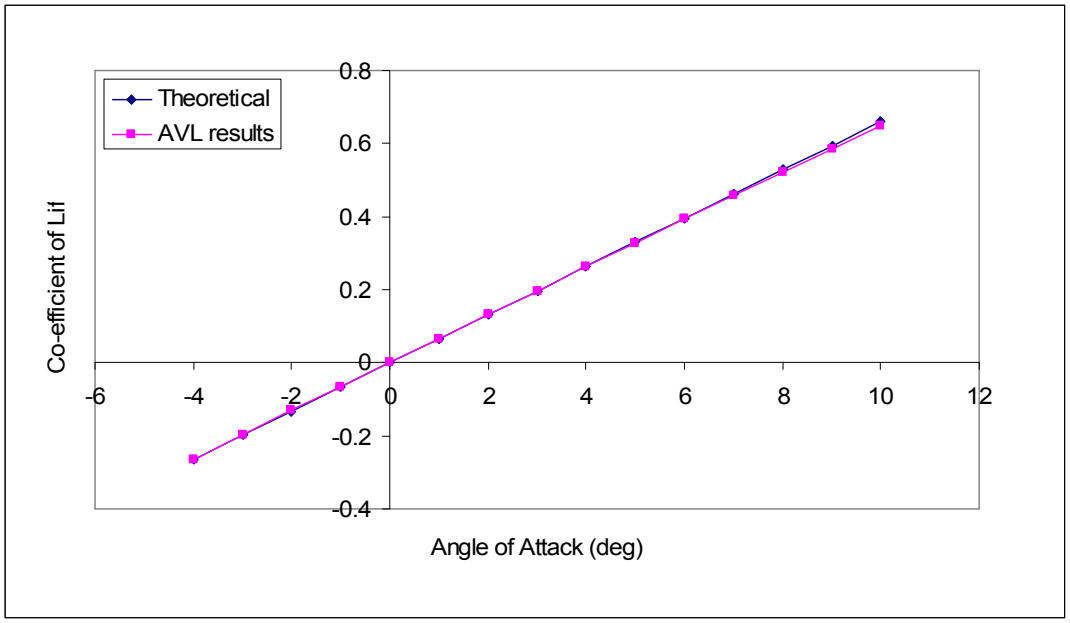

Figure 4.1: Comparison between Theoretical C_L for Span = 40 in versus AVL C_L for unextended wing configuration

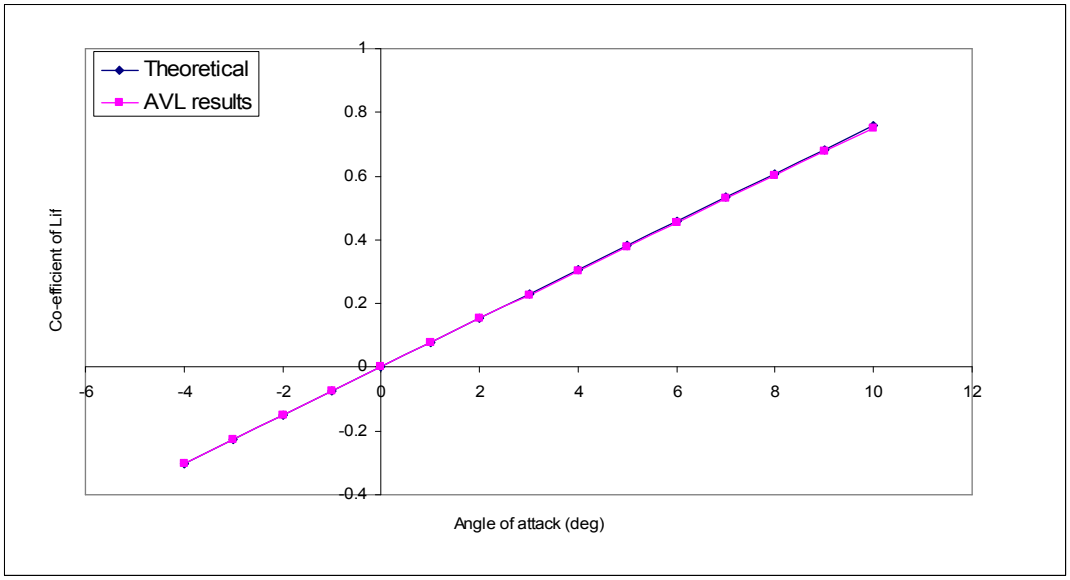

Figure 4.2: Comparison between Theoretical C_L for Span = 60 in versus AVL C_L for extended wing configuration

The above graphs show a comparison between the AVL results and the theoretical values (with a finite wing correction) for co-efficient of lift versus the angle of attack (deg) for an unextended wing configuration (span = 40 inches) (Figure 4.1) and for an extended wing configuration (span = 60 inches) (Figure 4.2). The airfoil section is NACA 0018. The AVL being developed for lifting surfaces at lower angles of attack, the graphs overlap for lower values of angles of attack and a small deviation is observed at the higher angles of attack. Thus, the validity of the AVL code for 3D airfoil sections is established.

The following graphs show a comparison between the values obtained from AVL for lift (Figure 4.3), co-efficient of drag (Figure 4.4) and co-efficient of pitching moment (Figure 4.7) versus the angle of attack (in degrees), as well as the drag polar (Figure 4.5) for the all the discussed wing configurations.

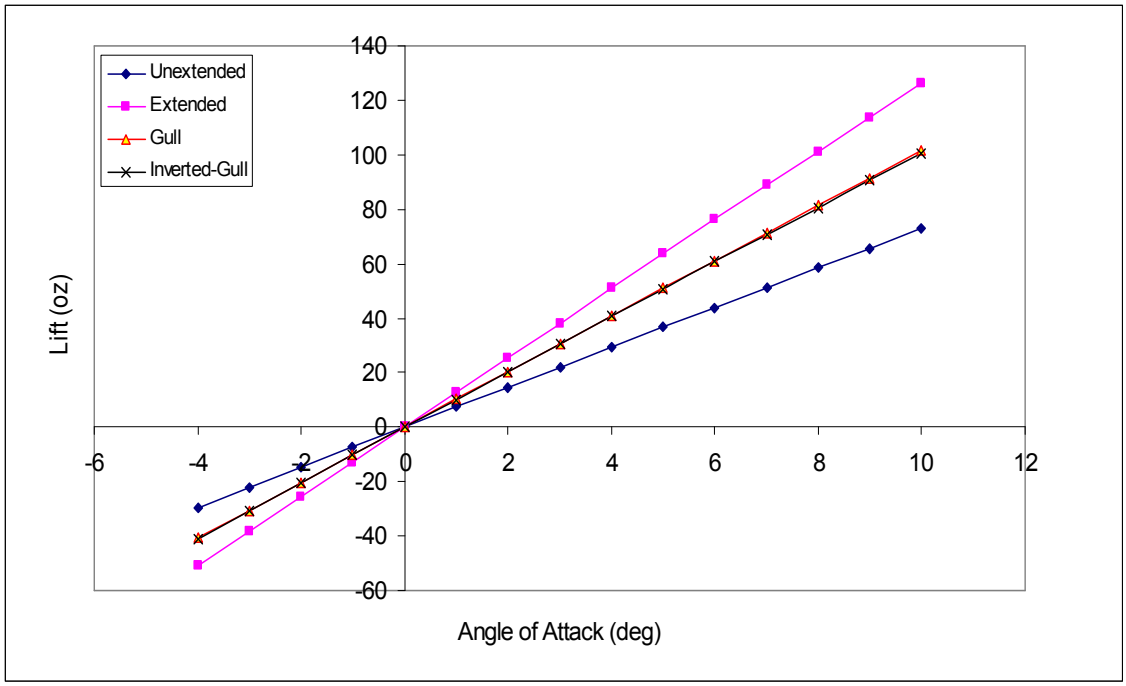

Figure 4.3: Comparison between AVL C_L-results for the four wing configurations

The wing area and the aspect ratio of a conventional wing are fixed. To increase the lift, the lift co-efficient should be increased which is typically achieved via an increase in the angle of attack. In contrast for the morphable wing, the lift increase could be achieved by an increase in the aspect ratio i.e. by increasing the wing area. Also, with an increase in the span, an increase in the lift co-efficient is achieved, since the lift curve slope of the wing in the extended wing configuration, (as compared to the unextended wing configuration), approaches the lift curve slope of a 2D airfoil.

In Figure 4.3, the lift curve is approximately coincident for the gull and inverted-gull configurations. It shows that the lift curve slope increases as the wingspan approaches the 2D airfoil theory. Also, it is noted that since a symmetric airfoil has been used, the lift is zero for all the wing configurations at zero degrees of angle of attack.

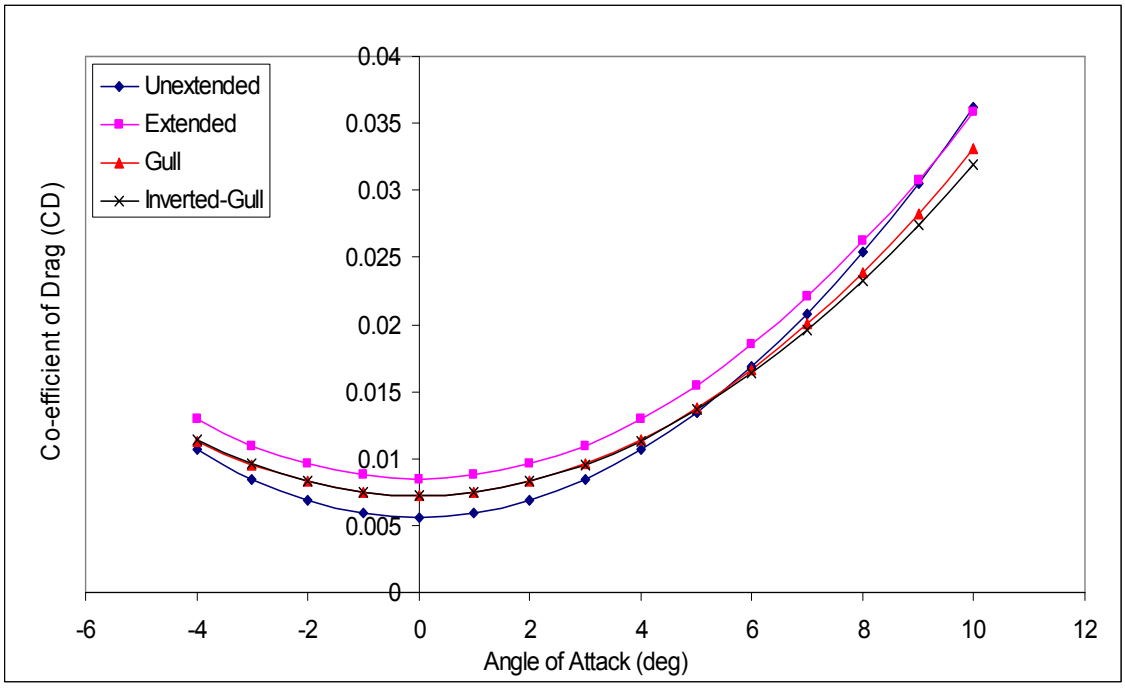

Figure 4.4: Comparison between AVL C_D-results for the four wing configurations

The slope of the co-efficient of drag (Figure 4.4) decreases due to the telescopic extension and at the higher angles of attack least drag co-efficient is observed for the inverted-gull Configuration.

$$C_D = C_{D0} + C_{Di} \quad \text{.....4.1}$$

$$C_D = C_{D0} + \frac{C_L^2}{\pi . AR . e} \quad \text{.....4.2}$$

Total Drag = Profile drag + Induced Drag

Where,

C_D = Co-efficient of Total Drag

C_{D0} = Profile Drag Co-efficient i.e. Co-efficient of skin friction and form drag

C_L = Co-efficient of Lift

AR = Aspect Ratio = $\frac{Span^2}{Planform \quad Area}$

e = Span Efficiency factor

The profile drag co-efficient obtained for the rounded-tip airfoil of aspect ratio 6 at zero lift by force test method is 0.0076 (See Ref.[25]). Here it is assumed to be constant for all the angles. This profile drag is direct proportional to the increase in the wingspan and thus the aspect ratio[25], while the value of the induced drag changes and shows significant reduction at higher angles of attack.

The subsequent figure shows the drag polar for all the wing configurations. It is to be noted that the change in the co-efficient of drag for the unextended configuration is larger than the change in the co-efficient of lift. And, for the extended configuration,

this change in the co-efficient of drag per change in the co-efficient of lift is reduced. This is due to the reduction in the co-efficient of induced drag resulting from the telescopic extension i.e. due to an increase in the aspect ratio.

$$C_{Di} = \frac{C_L^2}{\pi \times AR \times e} \quad \text{.....4.3}$$

This effect is prominent at the higher angles of attack. *In comparison to bird wings, a long and a comparatively narrower wing is used for gliding flight*.

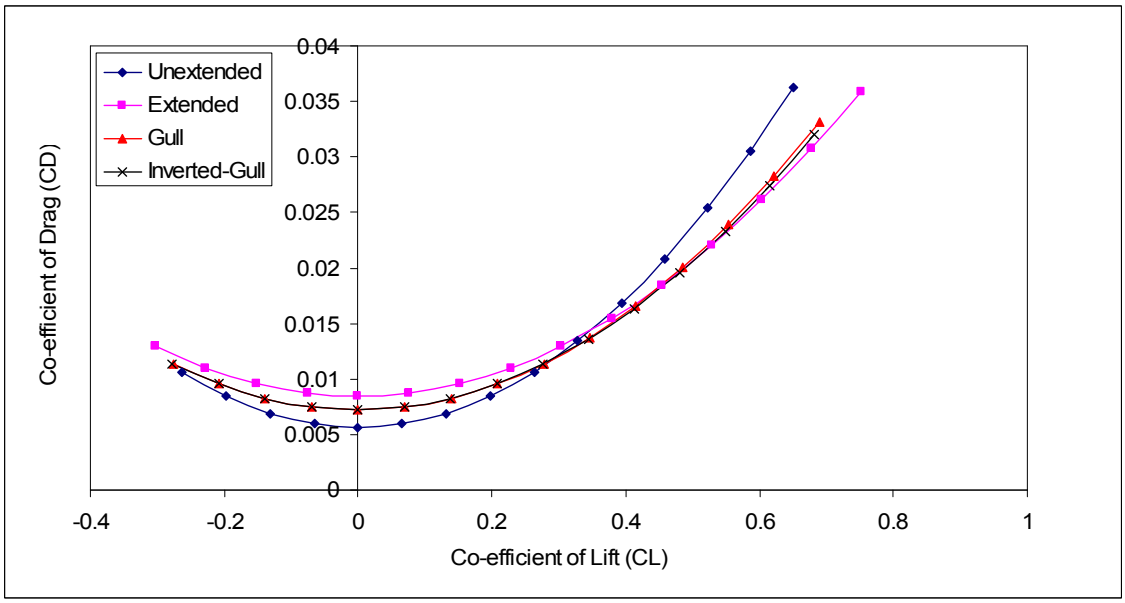

Figure 4.5: Comparison between AVL Drag Polar results for the four wing configurations

As a result of the above discussion on the decrease in drag co-efficient and a corresponding increase in the lift due to an increase in the aspect ratio, we observe an increase in the range for the aircraft. The range (R) can be computed from the following formula 4.4 (See Ref.[26]):

$$R = 2\sqrt{\frac{2}{\rho}}\frac{1}{c_t}\frac{(C_L S)^{1/2}}{C_D S}\left(W_f^{1/2} - W_e^{1/2}\right) \quad \text{.....4.4}$$

Where,

c_t = fuel consumption rate

W_f = gross weight with full tank

W_e = gross weight with empty tank

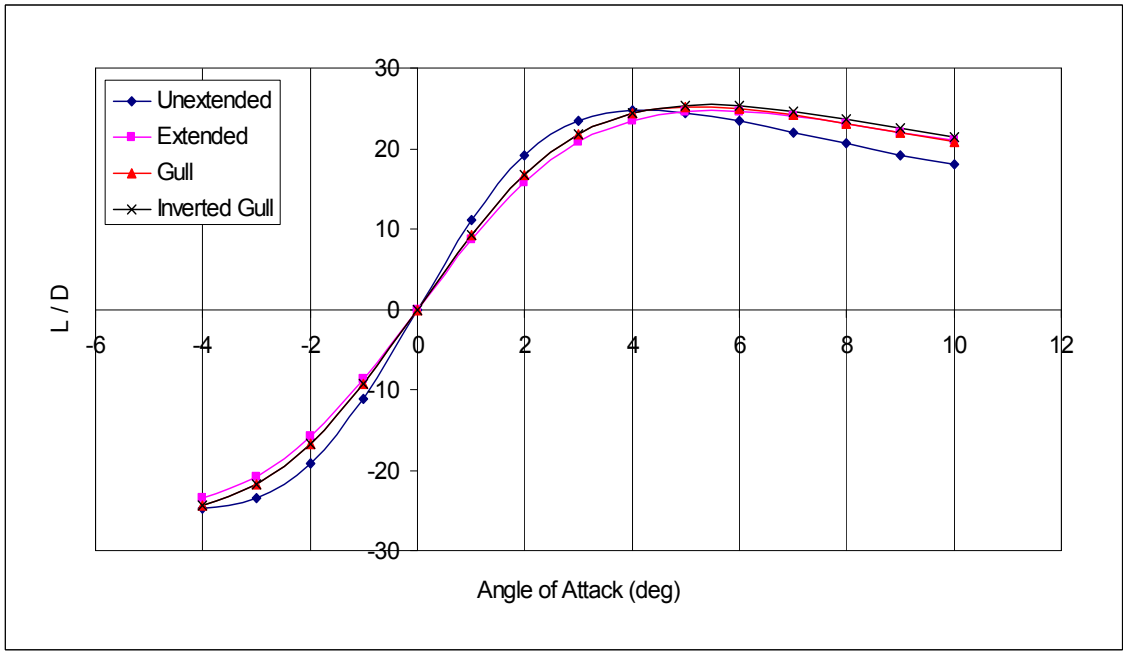

Figure 4.6: Comparison between AVL Lift / Drag results for the four wing configurations

The above figure shows the ratio of lift–to-drag plotted against the angle of attack in degrees. The lift-to-drag ratio is a measure of the aerodynamic efficiency of an airplane. Minimum thrust is required when flying the airplane when the lift-to-drag ratio is maximized. It is to be noted from the above figure that the location and value of maximum the lift-to-drag ratio changes due to wing morphing. It changes from about 4

degrees for the unextended configuration to about 5 to 6 degrees for the other configurations. Also, the drop in the ratio at higher angles of attack is more for the unextended i.e. the lower aspect ratio wing, than the other configurations. Thus, this morphable-wing aircraft could be operated at higher angles of attack thus generating more lift and less induced drag and maintains a high aerodynamic efficiency.

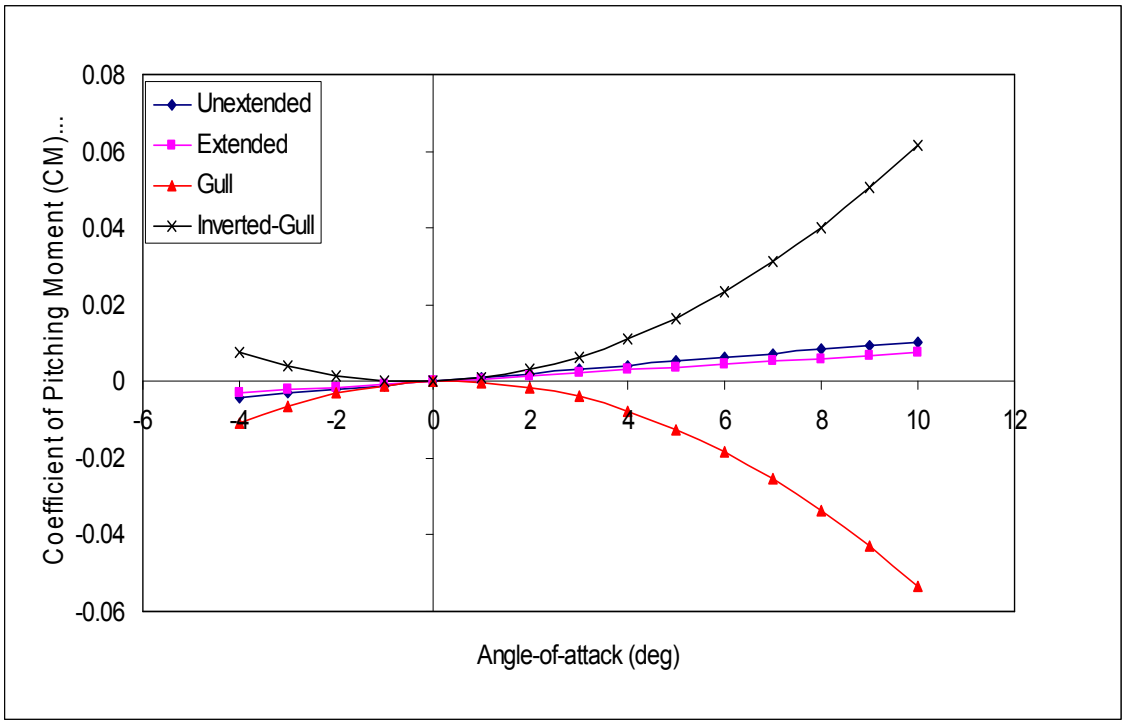

Figure 4.7: Comparison between Co-efficient of Pitching Moment for the four wing configurations

As expected, a lower pitching moment co-efficient is obtained due to telescopic expansion (Figure 4.7). Also, it is noted that since a symmetric airfoil has been used, the co-efficient of pitching moment is zero for all the wing configurations at zero degrees of angle of attack. But, an anomalous trend is observed in the case of the plot for gull and inverted-gull configurations, co-efficient of pitching moment versus the angle of attack.

A non-linear parabolic curve is obtained for the Gull configuration and its mirror image observed for the Inverted-Gull configuration.

It is to be noted that for the gull configuration, at positive angle of attack that would typically correspond to a nose-up condition; a negative pitching moment is generated, leading to the static stability of the aircraft. While for the inverted-gull configuration, at negative angle of attack that would typically correspond to a nose-down condition; a positive pitching moment is generated, again leading to the static stability of the aircraft. This non-linear path from positive co-efficient of pitching moment for a negative angle of attack to a negative co-efficient of pitching moment for a positive angle of attack is of interest to us.

These computational results are validated via wind tunnel tests on an in-house manufactured Balsa Wood Wing prototype at low speed subsonic conditions (quasi steady conditions).

4.2 Comparison Between AVL Results And Observed Seagull Flight

The following paragraphs gives a direct comparison between the observed seagull flight in chapter 2 (section 2.2) and the above obtained AVL results. This comparison gives us an insight towards the aerodynamic benefits of morphing which have been efficiently utilized by a seagull in flight.

1. TAKE-OFF (figure 2.2)

   a. higher angle of attack
   b. gull configuration
   c. short and high frequency flapping

Aerodynamic conditions for a gull wing at higher angle of attack

- high and positive value of lift
- lower value of coefficient of drag (as compared to other configurations)
- highly negative value of coefficient of pitching moment (ensuring static stability for nose-up condition)

2. SOARING (at higher altitude) (figure 2.3)

a. long and stretched out wings, hence a higher aspect ratio
b. wings slightly above the body of the bird
c. wings in a smaller gull configuration
d. lower angle of attack

Aerodynamic conditions for a higher aspect ratio (small gull configuration) at lower angle of attack

- lower but positive value of lift
- lower value of coefficient of drag
- small negative value of coefficient of pitching moment

3. STEEP DESCEND (figure 2.4)

a. wings pointing downward and slightly swept forward (slightly inverted-gull configuration)
b. negative angle of attack
c. wings stretched out

Aerodynamic conditions for a slight inverted-gull wing at negative angle of attack

- comparatively higher and negative value of lift

- lower value of coefficient of drag
- Positive value of coefficient of pitching moment (ensuring static stability for nose-down condition)

4. LOW LEVEL FLIGHT (slow and low level flight) (figure 2.5)

a. wings are not completely stretched out i.e. wingspan is short and hence comparatively broader
b. wings in complete gull configuration (inverted 'V') or an inverted 'L' type configuration
c. slightly higher angle of attack

Aerodynamic conditions for a gull wing at higher angle of attack

- slightly higher value of lift
- comparative lower value of coefficient of drag
- greater negative value of coefficient of pitching moment (compensating for the clockwise moment generated due to higher lift

5. LANDING (figure 2.6)

a. higher angle of attack
b. gull configuration
c. slower flapping
d. legs stretched out

Aerodynamic conditions for a gull wing at higher angle of attack

- high lift
- comparative lower value of coefficient of drag

- greater negative value of coefficient of pitching moment (ensuring static stability for nose-up condition)

With the preliminary knowledge on the aerodynamic loading, the focus is now shifted towards the basic problem in aeroelasticity; the static wing divergence. In chapter 5, we discuss a systematic method to approximate the static wing divergence speed for wing with the structural and geometric properties as a function of span.

CHAPTER 5

STATIC WING DIVERGENCE

5.1 Introduction

From early 1930's until World War II, airplane designers concentrated primarily on the establishment of a wing stiffness criterion to prevent flutter. In the calculations of the spanwise load distributions for structural design purposes, elastic deformations were often ignored. Margins of safety were fortunately adequate to allow for the error in spanwise lift distribution incurred by ignoring elastic deformations. But with the increase in speed and the need for thinner airfoils, the static wing divergence is of primary interest to the aircraft designer.

The wing divergence corresponds to the physical condition where the increase in aerodynamic moment about the elastic axis due to an arbitrary change in angle of attack is equal to the corresponding increase in the elastic restoring force. It gives us the maximum speed before the wing structure would start to break.

The following figure 5.1 shows a 2D airfoil. The lift and the pitching moment act at the aerodynamic center while the torsional restoring force acts about the elastic axis. The lift and the pitching moment are a function of the aircraft speed and the angle of attack. A physical limit is reached when these forces exceed the restoring moment and wing divergence takes place. This restoring moment is a function of the material properties and the geometry of the wing.

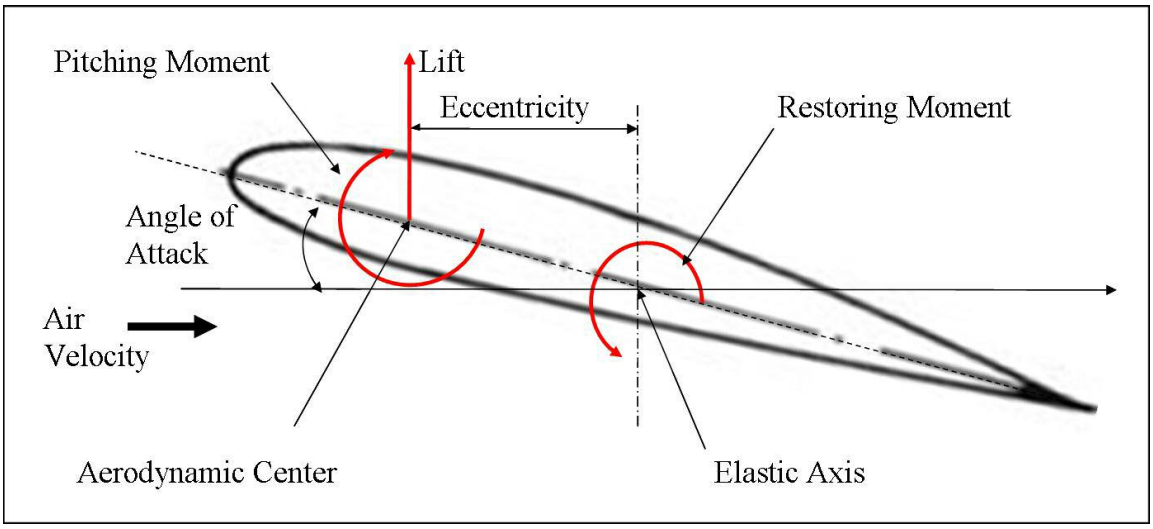

Figure 5.1: Rigid 2D Airfoil showing the aerodynamic forces and the restoring moment

5.2 Theory of Wing Divergence[23]

In the following discussion, it is assumed that the straight wings area characterized essentially by an elastic axis which is nearly perpendicular to the plane of symmetry of the airplane, and that chord-wise segments of the wing remain rigid, that is, camber bending is not considered. The differential equation of torsional aeroelastic equilibrium of a straight wing about its elastic axis is obtained by relating rate of twist to applied torque by the St. Venant torsion theory

$$\frac{d}{dy}\left(GJ\frac{d\theta}{dy}\right) = -\tau(y) \quad \text{..... 5.1}$$

where,

$\theta(y)$ is the elastic twist distribution.

G = Shear Modulus of Elasticity

J = Torsional Moment of Inertia

$\therefore GJ$ = Torsional stiffness

From the following figure it can be seen that the applied torque per unit span, $\tau(y)$, is

$$\tau(y) = \left(ecc_l + c^2 c_{mAC}\right) q - Nmgd \quad \text{.....} \quad 5.2$$

where,

c_l = local lift co-efficient,

c_{mAC} = local moment co-efficient about the aerodynamic center,

N = load factor normal to the wing surface (N = 1, for level flight),

mg = weight per unit span.

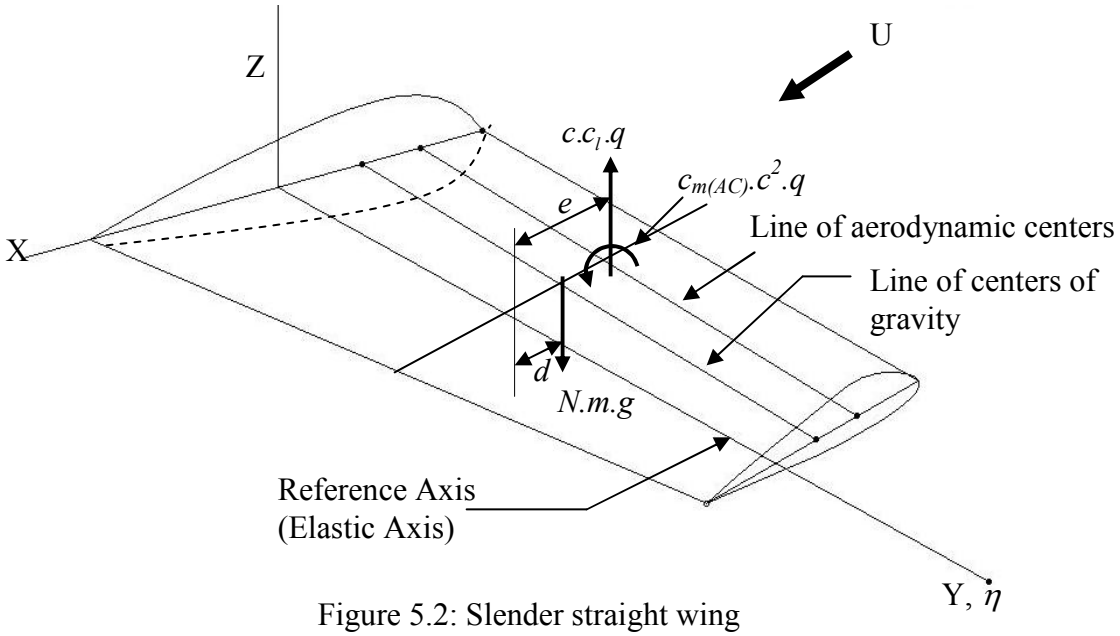

Figure 5.2: Slender straight wing

By substituting the equation (5.2) in equation (5.1), the following equation of equilibrium is obtained,

$$\frac{d}{dy}\left(GJ\frac{d\theta}{dy}\right) + qecc_l = -qc^2 c_{mAC} + Nmgd \quad \text{.....} \quad 5.3$$

The boundary conditions are

$$\theta(0) = \dot{\theta}(l) = 0$$

We know that the torque deflection equation is given by,

$$\theta(y) = \int_0^l C^{\theta\theta}(y,\eta).t(\eta).d\eta \quad \text{.....} \quad 5.4$$

where,

$C^{\theta\theta}$ = torsional deformation and influence function

$$C^{\theta\theta}(y,\eta) = \int_0^y \frac{d\lambda}{GJ}, \qquad (\eta \geq y),$$
$$\text{.....} \quad 5.5$$
$$C^{\theta\theta}(y,\eta) = \int_0^\eta \frac{d\lambda}{GJ}, \qquad (y \geq \eta),$$

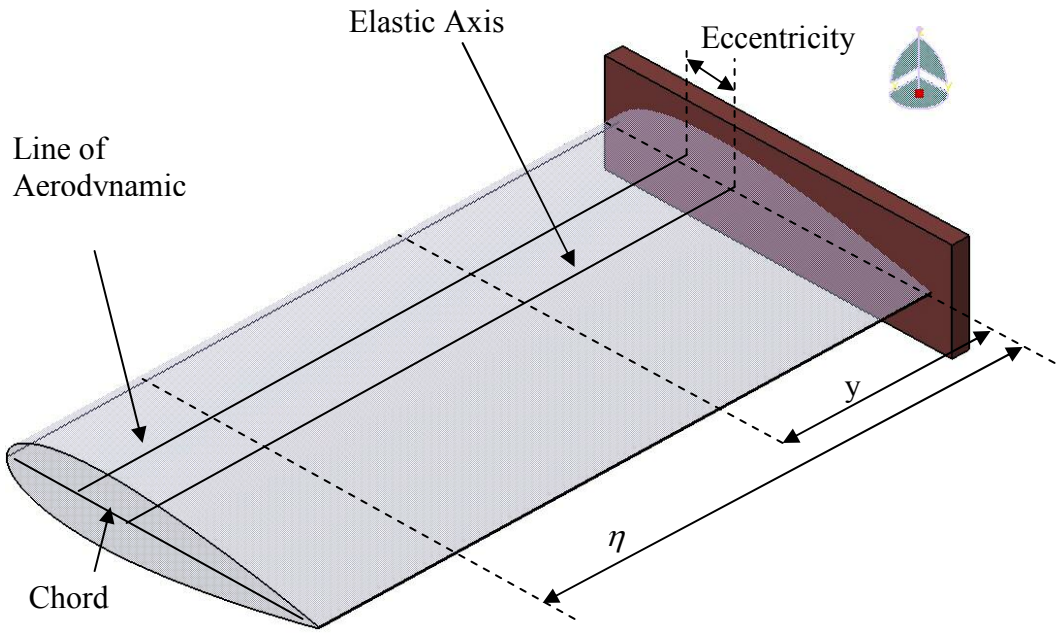

Figure 5.3: Deformation and influence function for a straight slender wing

It also noted that the bending deformation and influence function $\left(C^{zz}\right)$ is given by,

$$C^{zz}(y,\eta)=\int_0^{y}\frac{(\eta-\lambda)(y-\lambda)}{EI}d\lambda+\int_0^{y}\frac{d\lambda}{GK},\qquad(\eta\geq y)$$

$$C^{zz}(y,\eta)=\int_0^{\eta}\frac{(\eta-\lambda)(y-\lambda)}{EI}d\lambda+\int_0^{\eta}\frac{d\lambda}{GK},\qquad(y\geq\eta)\qquad\text{.....}\quad 5.6$$

The quantity EI and GK are bending and shear stiffness respectively. The deflection problem to be solved in computing the torsional influence function is shown in the above figure. A unit torque is applied at a distance η from the origin, and the resulting angular displacement at y is denoted by the $C^{\theta\theta}(y,\eta)$.

Thus,

$$\therefore\theta(y)=\int_0^{l}C^{\theta\theta}(y,\eta)\left[\left(ecc_l+c^2c_{mAC}\right)q-Nmgd\right]d\eta\quad\text{.....}\quad 5.7$$

Boundary conditions on θ are contained implicitly in the influence function and need not be stated separately.

We can regard the total angle of attack as a superposition of a rigid angle and an elastic twist,

$$\alpha(y)=\alpha^{r}(y)+\theta(y)\quad\text{.....}\quad 5.8$$

and correspondingly the local lift co-efficient as a superposition of

$$c_l(y)=c_l{}^{r}(y)+c_l{}^{e}(y)\quad\text{.....}\quad 5.9$$

where,

$\alpha^{r}(y)$ = Local angle of attack measured from zero lift, not including elastic twist and spanwise aerodynamic induction effects. It may contain such terms such as

wing attitude, geometric twist, aerodynamic twist resulting from deflected control surfaces, or induced angle of attack due to a gust

$c_l^{\,r}(y)$ = Local lift co-efficient distribution resulting from rigid twist, $\alpha^r(y)$

$c_l^{\,e}(y)$ = Local lift co-efficient distribution resulting from elastic twist, $\theta(y)$

Inserting equation (5.9) in equations (5.3) and (5.7), we get the following alternative differential and integral equation,

$$\frac{d}{dy}\left(GJ\frac{d\theta}{dy}\right) + qecc_l^{\,e} = -qecc_l^{\,r} - qc^2 c_{mAC} + Nmgd \quad \text{..... 5.10}$$

and,

$$\theta(y) = q\int_0^l C^{\theta\theta}(y,\eta)\,ecc_l^{\,e}\,d\eta + f(y) \quad \text{..... 5.11}$$

where

$$f(y) = q\int_0^l C^{\theta\theta}(y,\eta)\left(qecc_l^{\,r} + qc^2 c_{mAC} - Nmgd\right)d\eta \quad \text{..... 5.12}$$

In both the equations, $\theta(y)$ and $c_l^{\,e}(y)$ are regarded as unknown functions, and all other terms are assumed specified. This problem becomes mathematically determinate as a soon as the second relation between the two unknowns is stated; this is supplied by some appropriate choice of aerodynamics theory. As stated earlier, the aerodynamic theory is assumed to have a linear relation between incidence and lift distribution which can be represented symbolically by

$$\alpha(y) = \wp(cc_l) \quad \text{..... 5.13}$$

where, $\wp$ is a linear operator which operates on the lift distribution $cc_l(y)$ to produce the required incidence distribution $\alpha(y)$. For example, in the case of strip theory, $\wp$ is simply

$$\wp = \frac{1}{a_0 c} \quad \text{..... 5.14}$$

where, a_0 is the local two-dimensional slope of the lift co-efficient curve.

The torsional divergence speed of a three dimensional wing is determined from the lowest eigenvalue of the dynamic pressure q obtained from the homogeneous differential or integral equations of equilibrium. It thus represents the speed at which the wing, arranged so that in the untwisted conditions it experiences no aerodynamic moments whatever, is theoretically capable of assuming an arbitrary amount of twist and remaining in neutral equilibrium there under the airloads due to the twist alone. Since the solution to a non-homogeneous equation becomes infinite for the eigenvalues of the corresponding homogeneous equation, we may conclude that an actual wing (which can never be adjusted so that the rigid airloads are exactly zero) would twist off and be destroyed as its divergence speed. Following are the homogeneous forms of equations (5.10) and (5.11) are

$$\frac{d}{dy}\left(GJ\frac{d\theta}{dy}\right) + qecc_l^{\,e} = 0 \quad \text{..... 5.15}$$

$$\theta(y) = q\int_0^l C^{\theta\theta}(y,\eta).ecc_l^{\,e}\,d\eta \quad \text{..... 5.16}$$

Equations (5.15) or (5.16) could be alternatively used along with equation (5.13) to compute the divergence speed. They are satisfied by the same infinite set of

eigenvalues and eigenfunctions. The lowest eigenvalue is the dynamic pressure, q_D, corresponding to torsional divergence. The corresponding eigenfunctions $\theta_D(y)$ is the spanwise twist distribution at the divergence speed.

When treating practical airplane problems where assured accuracy is required, it is usually necessary to employ numerical solutions. Applying strip theory, equation (5.16) has the form,

$$\frac{c_l^{\,e}}{dC_L/d\alpha}\theta(y) = q\int_0^l C^{\theta\theta}(y,\eta)ecc_l^{\,e}\,d\eta \quad \text{..... 5.17}$$

Here, it is to be noted that $a_0(y)$ has been replaced by $dC_L/d\alpha$, the effective lift-curve slope corrected for aspect ratio. The matrix equation for equation (5.17) can be written as follows

$$[A]\{cc_l^{\,e}\} = q[E]\{cc_l^{\,e}\} \quad \text{..... 5.18}$$

where,

$$[A] = \frac{1}{dC_L/d\alpha}\begin{bmatrix} \ddots & \\ & 1/c \\ & & \ddots \end{bmatrix} \quad \text{.....5.19.a}$$

$$[E] = \left[C^{\theta\theta}\right]\begin{bmatrix} \ddots & \\ & e \\ & & \ddots \end{bmatrix}\begin{bmatrix} \ddots & \\ & \overline{W} \\ & & \ddots \end{bmatrix} \quad \text{.....5.19.b}$$

The basic requirement of a non-zero solution is the vanishing of the determinant of the co-efficients of $cc_l^{\,e}$.

$$\left|[A] - q[E]\right| = 0 \quad \text{..... 5.20}$$

This determinant, when expanded, yields a polynomial in q, the smallest root of which corresponds to the divergence condition, q_D. The divergence speed is then obtained by,

$$U_D = \sqrt{\frac{q_D}{\rho/2}} \quad \text{..... 5.21}$$

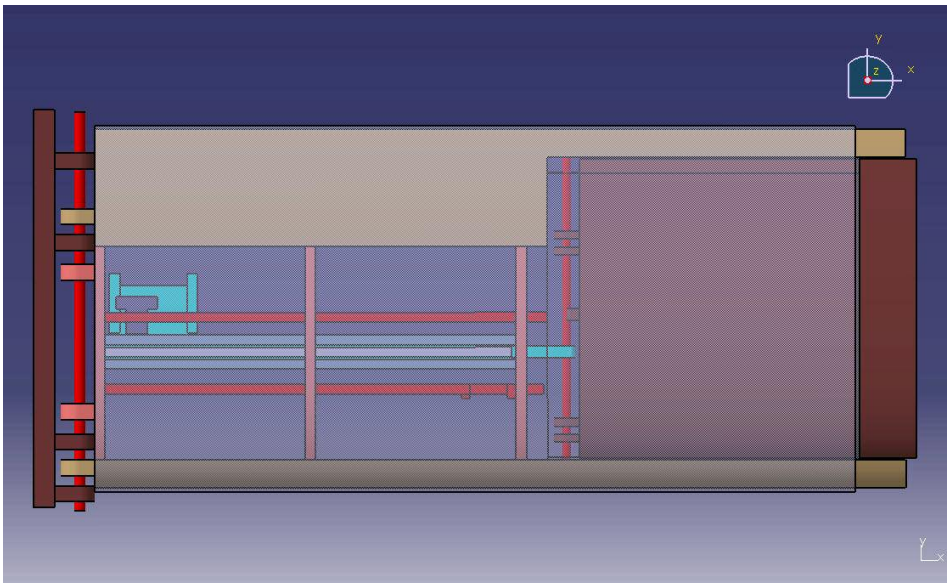

Figure 5.4: Plan-view of the unextended wing configuration

The above figure shows the plan–view of the morphing wing. The line containing the centers of gravity is not straight. Also, by observation, we notice that for this multi-material, non-uniform structure the modulus of elasticity, shear modulus, area, area moment of inertia (I_{yy}), torsional moment of inertia and shear form factor, all would be a function of span. Thus, the torsional deformation and influence function would also be a function of the span.

The following plots show the location of the center of gravity over the span for the unextended wing configuration. This data has been obtained from CATIA V5. The

wing was divided by 17 planes i.e. 16-element model. The planes were chosen under the assumption that we would have a constant area and least amount of change in the geometry in-between the planes. This model is assumed to be the truth model capturing almost all the structural properties of the wing.

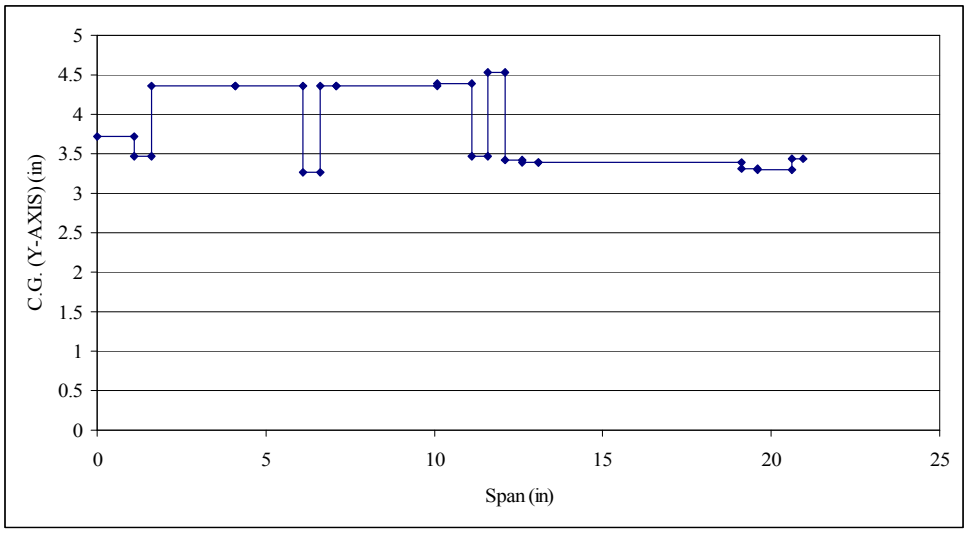

Figure 5.5: Side-view of the C.G. locations over the span for unextended configuration

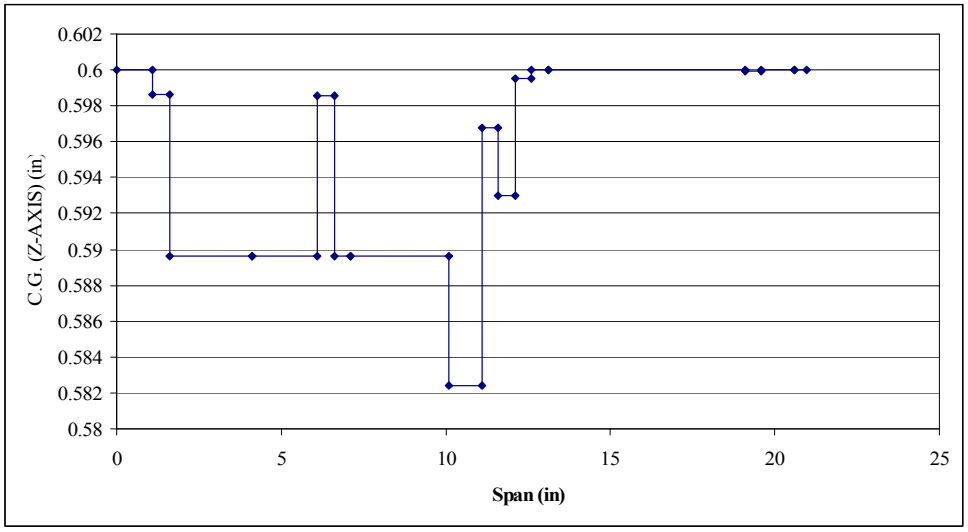

Figure 5.6: Top-view of the C.G. locations over the span for unextended configuration

The following plot shows the area moment of inertia about the bending axis (I_{YY}) for the 16-element representation of the wing in the unextended configuration.

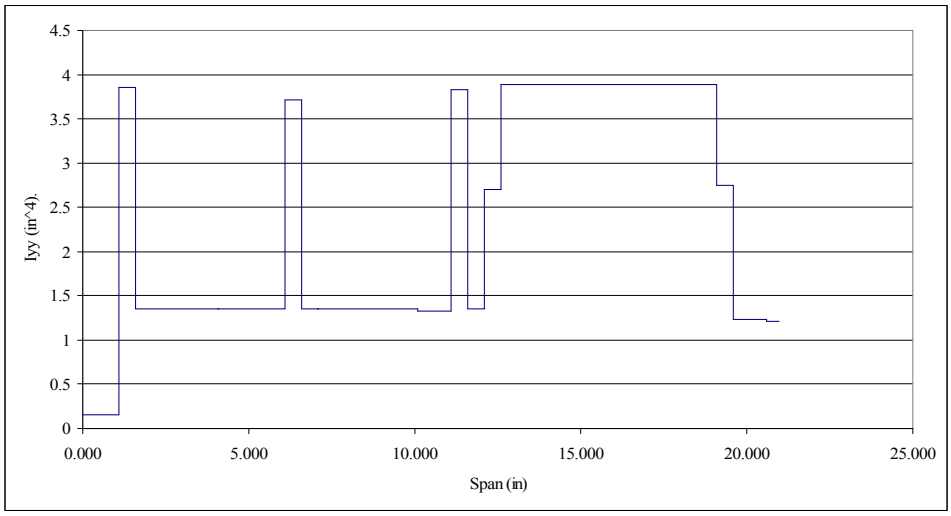

Figure 5.7: Variation of the area moment of inertia about the (y-axis) as a function of span for unextended configuration

The following sections discuss a systematic procedure to calculate the bending and torsional stiffness' as well as the torsional deformation and influence functions required in the further calculations for the divergence speed. Here, we also calculate the bending deformation and influence function which would be required for the study of the dynamic aeroelastic problems which forms a part of the future study for this morphable wing.

5.3 Bending and Torsion Theory[24]

In this section, we discuss the Euler-Bernoulli beam theory as well as the Timoshenko beam theory and state the equations for the bending and rotation of beams under the influence of an end load applied to a cantilever beam. Further, we also discuss the torsion theory.

Euler-Bernoulli beam theory or just beam theory is a simplification of the linear isotropic theory of elasticity which provides a means of calculating the load-carrying and deflection characteristics of beams.

The full theory of elasticity is too complicated for routine design work. To simplify it, Euler-Bernoulli beam theory makes the following assumptions which are approximately true for most beams:

1. The beam is long and slender.
    - length >> width
    - length >> depth
    - therefore, tensile/compressive stresses perpendicular to the beam are much smaller than tensile/compressive stresses parallel to the beam.
2. The beam cross-section is constant along its axis.
3. The beam is loaded in its plane of symmetry.
4. Plane sections of the beam remain plane.
    - approximately true for most solid beam forms
    - not necessarily true for a truss-beam
    - this was Bernoulli's critical contribution

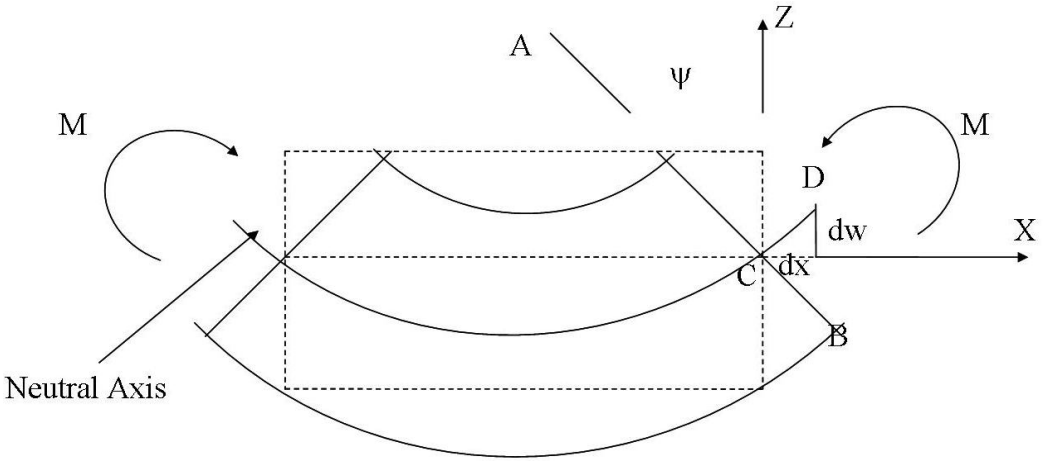

Figure 5.8: Euler-Bernoulli Bending Theory (pure bending moment)

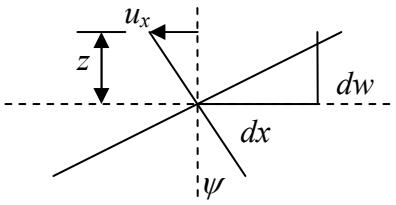

Form the above figure,

$u_z = w(x)$ = vertical deflection of the neutral axis, and..... 5.22

$$u_x = -z.\psi(x) \quad \text{.....} \quad 5.23$$

If the plane AB remains perpendicular to CD, then

$$\psi = \frac{dw}{dx} \quad \text{.....} \quad 5.24$$

$$\therefore u_x = -z\frac{dw}{dx} \quad \text{.....} \quad 5.25$$

Solving, the stress-strain relations, we get the moment as

$$M = E.I\frac{d^2w}{dx^2} \quad \text{.....} \quad 5.26$$

where,

E = Elastic Modulus of Elasticity

I = Area Moment of Inertia

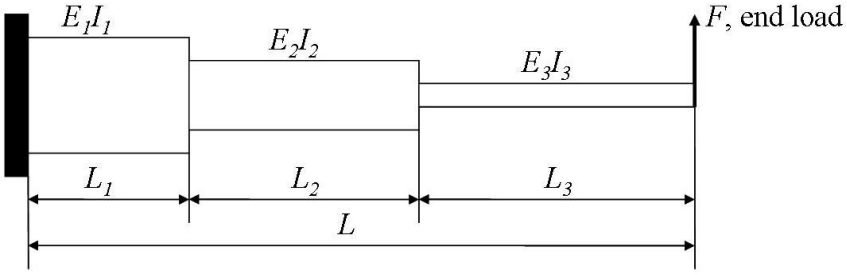

Figure 5.9: Test Problem – Structure with geometric and material properties as a function of length L

From Euler-Bernoulli bending theory, we get the following results –

1. when a load P is applied,

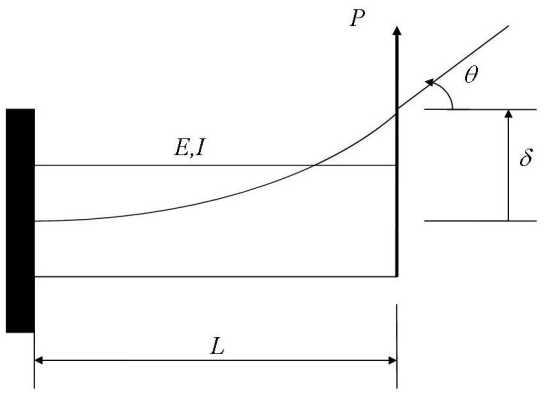

Figure 5.10: Beam subjected to an end shear load P

$$\theta = \frac{PL^2}{2EI} \quad \text{..... 5.27}$$

$$\delta = \frac{PL^3}{3EI} \quad \text{..... 5.28}$$

2. when a moment M is applied

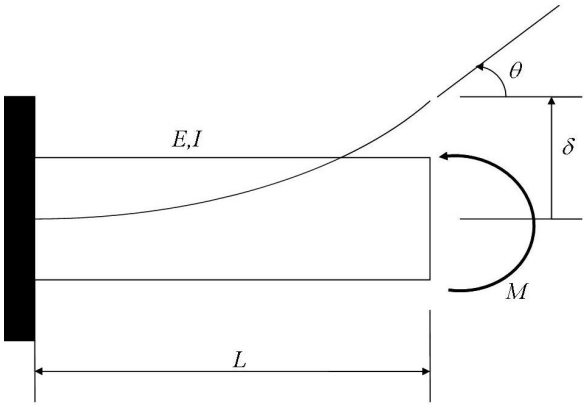

Figure 5.11: Beam subjected to an end moment M

$$\theta = \frac{ML^2}{2EI} \quad \text{..... 5.29}$$

$$\delta = \frac{ML^2}{2EI} \quad \text{..... 5.30}$$

From the above results, for the first segment in figure 5.8

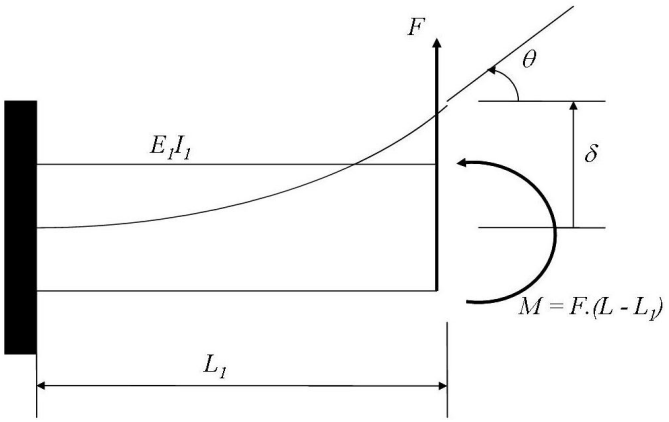

Figure 5.12: Element 1 of the test problem

$$\delta_1 = \frac{FL_1^{\,3}}{3E_1I_1} + \frac{F(L-L_1)L_1^{\,2}}{2E_1I_1} \quad \text{..... 5.31}$$

$$\theta_1 = \frac{FL_1^{\,2}}{2E_1I_1} + \frac{F(L-L_1)L_1}{E_1I_1} \quad \text{..... 5.32}$$

and, second segment in figure 5.8

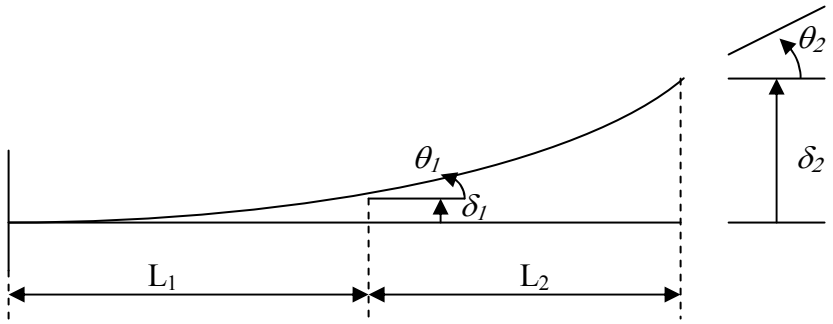

Figure 5.13: Deflections and rotations of the elements due to the end shear force applied to the test problem

$$\delta_2 = \delta_1 + \theta_1 L_2 + \frac{FL_2^{\,3}}{3E_2I_2} + \frac{F(L-L_1-L_2)L_2^{\,2}}{2E_2I_2} \quad \text{..... 5.33}$$

$$\theta_2 = \theta_1 + \frac{FL_2^{\,2}}{2E_2I_2} + \frac{F(L-L_1-L_2)L_2}{E_2I_2} \quad \text{..... 5.34}$$

Thus, by forward substitution, we can generalize the above procedure for ‘n’ segments.

Real-life structures never meet these assumptions exactly, but often approximate them well enough for the theory to make useful predictions. The Timoshenko beam theory is an extension of the Euler-Bernoulli beam theory to allow for the effect of transverse shear deformation. This more refined beam theory relaxes the normality assumption of plane sections that remain plane and normal to the deformed centerline. The relaxation takes the form of allowing an additional rotation to the bending slope, and thus admits a nonzero shear strain.

Here, we consider

1. The beam to be short and stubbed
2. The load applied at the shear center
3. Plane sections of the beam do not remain plane.

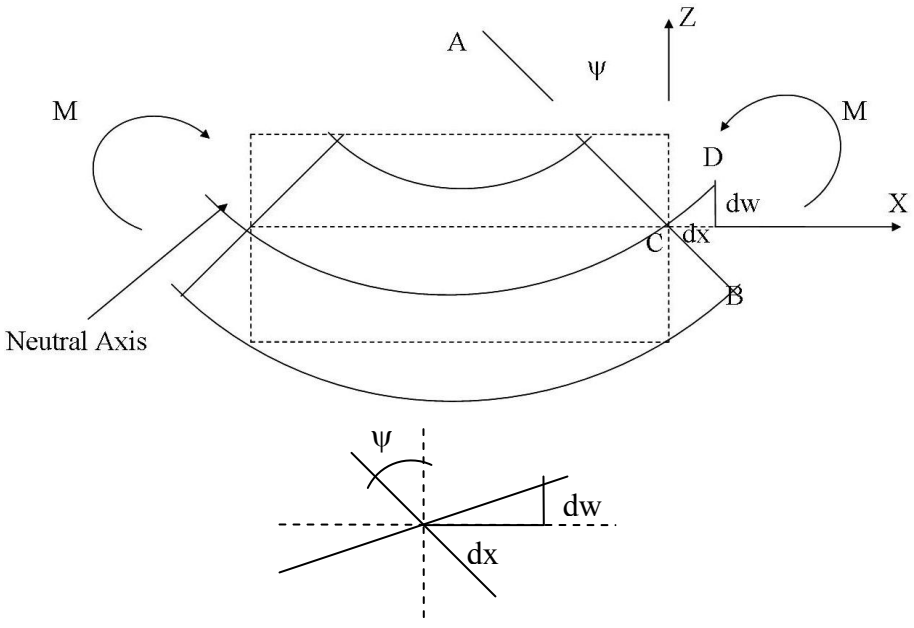

Figure 5.14: Timoshenko Bending Theory (pure bending moment)

Form the above figure,

$$u_x = -z.\psi(x) \quad \text{..... 5.35}$$

$$\psi \neq \frac{dw}{dx} \quad \text{..... 5.36}$$

Thus the difference between the Timoshenko beam and the Euler-Bernoulli beam is that the former includes the effect of the shear stresses on the deformation. A constant shear over the beam height is assumed.

$$\theta = \psi(x) + \frac{dw}{dx} \quad \text{..... 5.37}$$

Setting the shear angle, ψ, to zero leads to the Bernoulli beam theory. Then the slope of the centre axis, w', is the same as the rotation, θ, of the cross-section.

$$\sigma_{xx} = -E.z\frac{d\psi}{dx} \quad \text{... (4.38)}$$

$$\sigma_{xz} = G\left(\frac{\partial u_x}{\partial z} + \frac{\partial u_z}{\partial x}\right) = G\left(-\psi(x) + \frac{dw}{dx}\right) \quad \text{... (4.39)}$$

This equation is better than Euler-Bernoulli equation but still it is a constant shear across the cross-section. Hence, we introduce a form factor κ^2.

$$\therefore \sigma_{xz} = \kappa^2 G\left(-\psi(x) + \frac{dw}{dx}\right) \quad \text{..... 5.40}$$

Integrating the stress over the cross-sectional area, we get moment as,

$$M = E.I\frac{d\psi}{dx} \quad \text{..... 5.41}$$

and shear force as,

$$V = \kappa^2 G\left(-\psi(x) + \frac{dw}{dx}\right) \quad \text{..... 5.42}$$

From Timoshenko bending theory, we get the following results, when a load P is applied to beam with cross-sectional area A ,

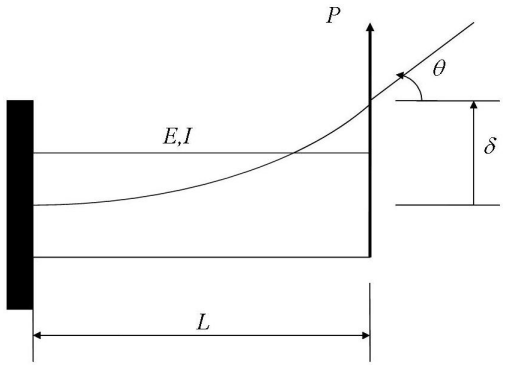

Figure 5.15: Beam subjected to an end shear load P

$$\theta = \frac{PL^2}{2EI} + \frac{P}{\kappa^2 GA} \quad \text{..... 5.43}$$

$$\delta = \frac{PL^3}{3EI} + \frac{PL}{\kappa^2 GA} \quad \text{..... 5.44}$$

Combining equations (5.33), (5.34), (5.43) and (5.44) for a beam with 'n' elements, then the generalized equation for the ith element could be written as

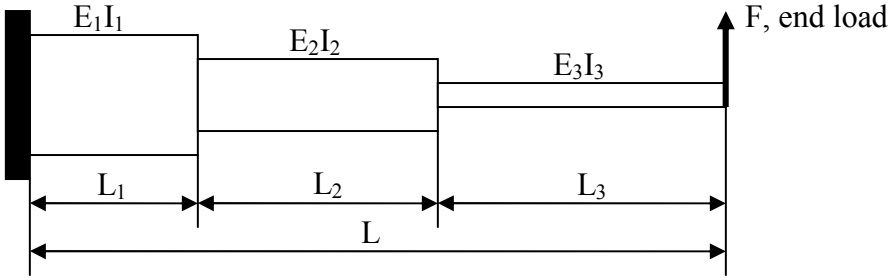

Figure 5.16: Test Problem – Structure with geometric and material properties as a function of length L

$$\delta_{i+1} = \delta_i + \theta_i L_{i+1} + \frac{FL_{i+1}{}^3}{3E_{i+1}I_{i+1}} + \frac{ML_{i+1}{}^2}{2E_{i+1}I_{i+1}} + \frac{FL_{i+1}}{\kappa_{i+1}{}^2 G_{i+1}A_{i+1}} \quad \text{..... 5.45}$$

$$\theta_{i+1} = \theta_i + \frac{FL_{i+1}^{\ 2}}{2E_{i+1}I_{i+1}} + \frac{ML_{i+1}}{E_{i+1}I_{i+1}} + \frac{F}{\kappa_{i+1}^{\ 2}G_{i+1}A_{i+1}} \quad \text{..... 5.46}$$

where, the moment is

$$M = F\left(L - \sum_{j=1}^{i} L_j\right) \quad \text{..... 5.47}$$

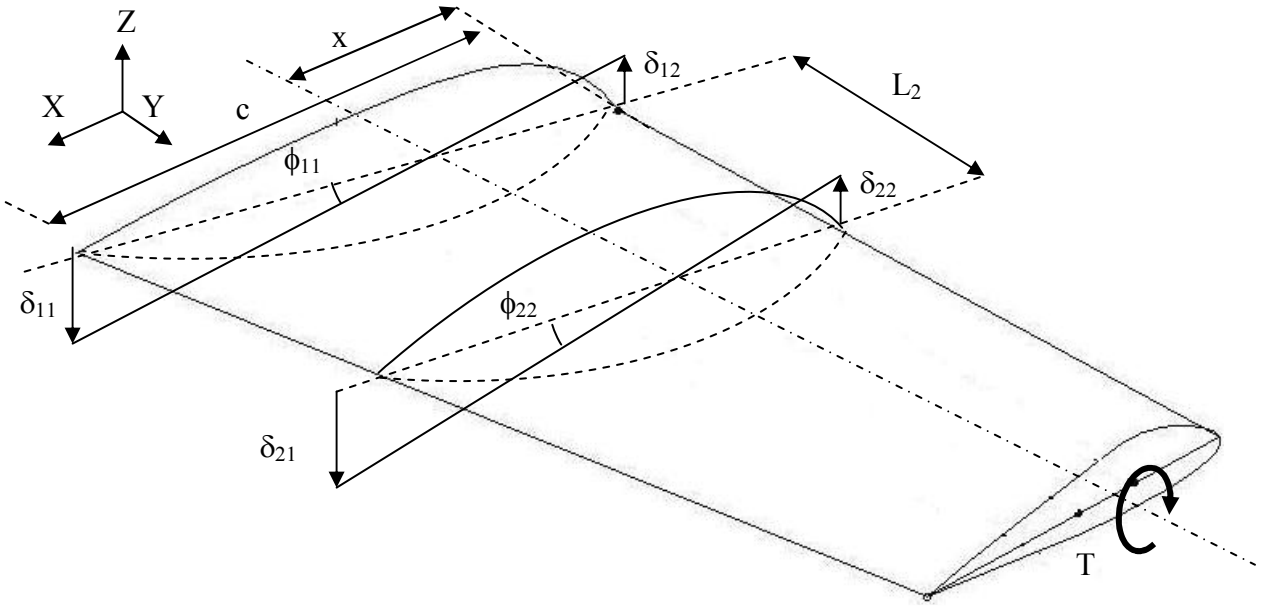

Figure 5.17: Wing subjected to an end moment 'T'

For small angles,

$$\phi_{11} = \frac{\delta_{12}}{x.c} = \frac{\delta_{11}}{(1-x)c} \quad \text{..... 5.48}$$

$$\therefore x = \frac{\delta_{12}}{(\delta_{11} + \delta_{12})c} \quad \text{..... 5.49}$$

and similarly,

$$\phi_{22} = \frac{\delta_{22}}{x.c} = \frac{\delta_{21}}{(1-x)c} \quad \text{..... 5.50}$$

Now, from the solid mechanics results, we know that

$$\frac{T}{J} = \frac{G\phi}{L} \quad \text{..... 5.51}$$

where,

ϕ = angle of twist

Here, we assume that the structural and geometric properties of the wing remain constant over the length L_2 i.e. over the second element

$$\frac{T}{J_2} = \frac{G_2\phi_2}{L_2} \quad \text{..... 5.52}$$

where,
$\phi_2 = \phi_{22} - \phi_{11}$ = the total twist

The generalized equation for the ith element could be written as

$$\frac{T}{J_i} = \frac{G_i\phi_i}{L_i} \quad \text{..... 5.53}$$

5.4 Wing divergence of Morphable Wing

We will use equations (5.45), (5.46), (5.47) and (5.53) to calculate the stiffness' and their respective deformation and influence functions. But, before we could use them, the minimum numbers of stations or elements are required to be identified, which divide the wing with an assumption that the structural and geometric properties remain constant over the span of each element.

The following figure shows that the wing has been divided in 5 elements. And the subsequent figure shows the 2D representation of the above figure. This is cantilever beam model created in ANSYS Classic. The model is loaded at the free end as shown by the red arrow.

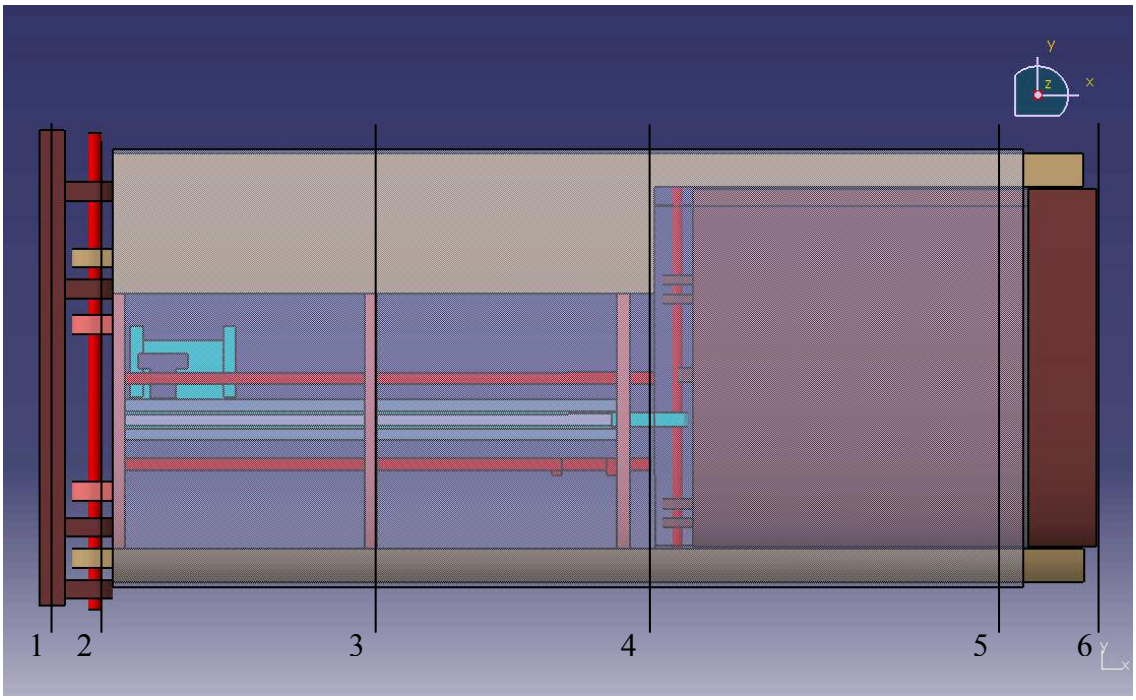

Figure 5.18: Plan-view of the unextended wing configuration divided into 5-segments

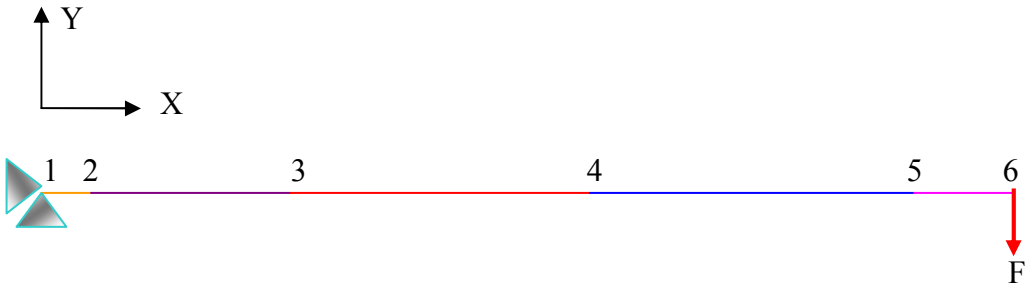

Figure 5.19: 2D Beam – 5-element model of the wing in unextended wing configuration

The element used is BEAM3. This is a uniaxial element with tension, compression, and bending capabilities. The element has three degrees of freedom at each node: translations in the nodal x and y directions and rotation about the nodal z-axis.

The real constant sets contain the area, area moment of inertia about the y-axis, and height of the element in the z-direction. These values are obtained from CATIA V5. A uniform material (steel) has been assumed for the initial analysis.

The deflections at each node are noted. The analysis is repeated several times with different number of elements.

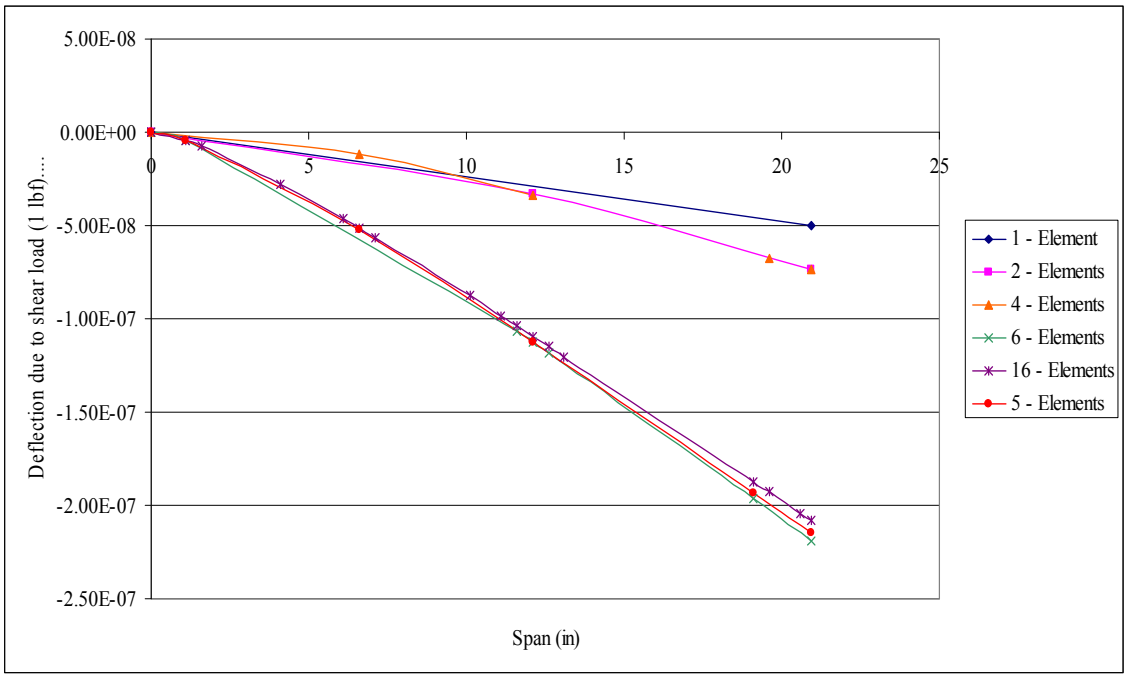

Figure 5.20: Deflections measured on the 2D beam model of various elements when subjected to an end shear load of 1 lbf

The above plot shows the deflections noted at each node due an applied shear force of 1 lbf. It is to be noted that when the entire wing is assumed to have the same geometric properties (averaged over the entire span into a single element) shows a deflection which is distinctly different from the wing which is divided into 16 elements having varying geometric properties over the span (but constant for each element) as calculated from CATIA V5. It is also to be noted that when the wing was approximated as a 5-element structure as shown in figure 5.17, the above figure shows that the

deflections are in close correspondence to the deflections shown by a 16-element wing structure. Hence, the wing could be safely assumed to be a 5-element structure when analyzing the unextended wing configuration.

The 3D wing model is subjected to an end shear load and then the free end is twisted by applying a moment. From ANSYS, the deflections are noted at the nodes shown in figure 5.18, for both the cases of applied loading. And using equations (5.45), (5.46), (5.47) and (5.53)), the following torsional moment of inertias and form factors are obtained for the two different materials that were used in the analysis

Table 5.1: Comparison between the torsional stiffness and the form factor of the same structure but different materials

Nodes	**Element**	**Torsional Stiffness (in-lb/rad.) (*J*)**		**Form Factor (κ)**	
		Steel	**Balsa Wood**	**Steel**	**Balsa Wood**
1-2	1	19.28	18.49	16.9594	16.5157
2-3	2	2.98	2.90	0.0197	0.0193
3-4	3	5.84	5.79	0.0188	0.0185
4-5	4	12.45	13.04	0.0118	0.0116
5-6	5	1.45	1.38	0.0127	0.0124

Here, in the above table 5.1, we show that by using two different materials for the wing structure, we have obtained similar values for the torsional stiffness and the form factor. These properties are a function of the geometry of the structure and not the material. Thus the above method has been verified.

The following flowchart figure 5.20 explains the procedure followed to calculate the stiffness' of the structure as a function of the span.

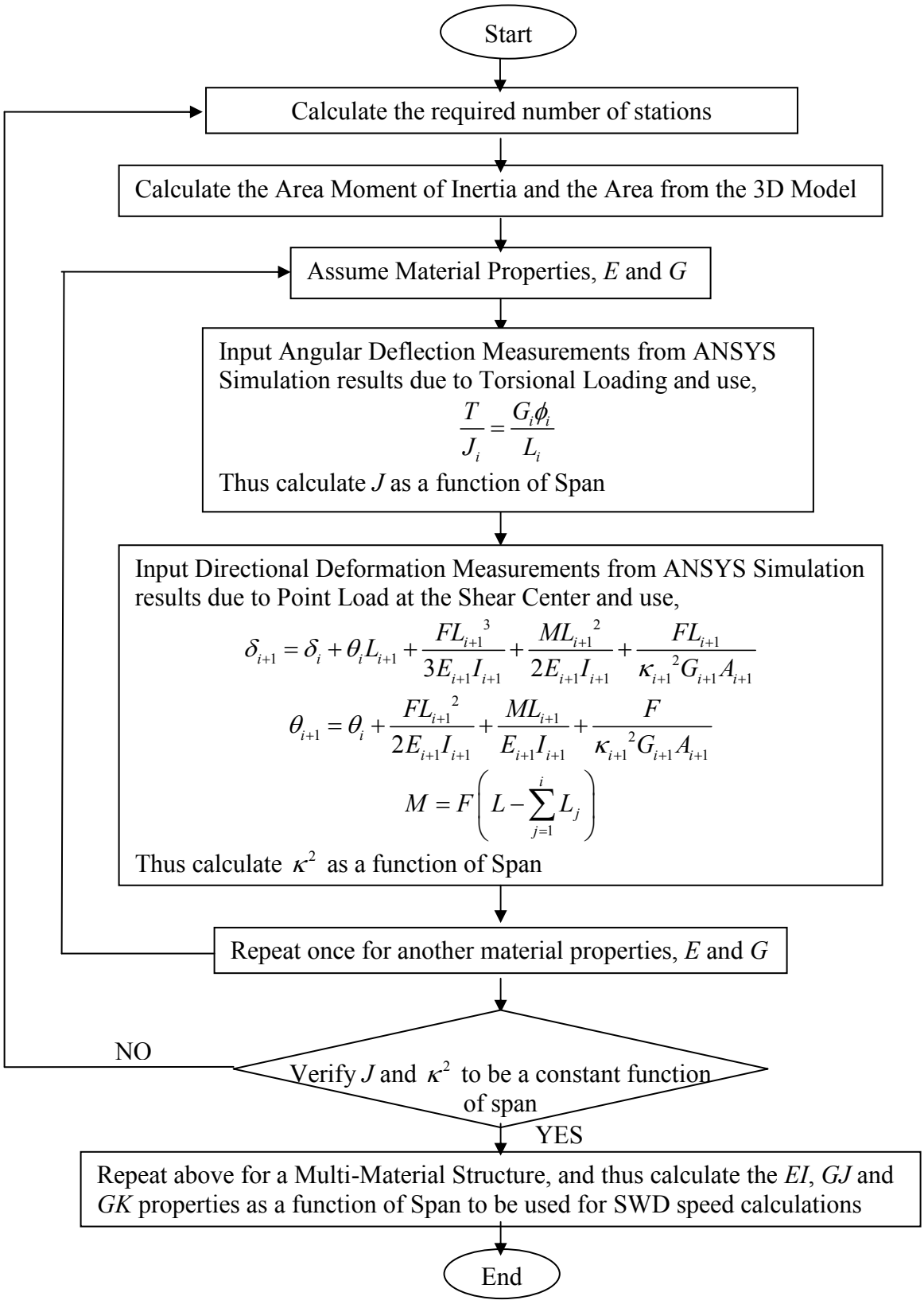

Figure 5.21: The flowchart to calculate the approximate stiffness of a structure

We observe a higher value of the form factor for the first element since this element undergoes the least shear deformation. And, since more material is located away from the elastic axis; this element also shows a high torsional stiffness. The element 4 also shows a higher value of the torsional stiffness which results due to the overlapping of the extendible wing inside the main outer wing.

With the confirmation of similar values for the torsional stiffness and the form factor, the analysis is repeated for the original multi-material wing structure. The equations (5.45), (5.46), (5.47) and (5.53) are used again. Now, the geometric properties of the structure i.e. the values for area, area moment of inertia, torsional area moment of inertia and form factor are know. And, the material properties i.e. the modulus of elasticity and the shear modulus of elasticity and thus the bending and torsional stiffness are unknown. The deflections are obtained from ANSYS simulations. By forward substitution process, the stiffness' are obtained as a function of span.

The entire process is repeated for an extension of 2.5, 5.0 and 7.5 *(100%)* inches and, the bending and torsional stiffness' are calculated as shown in the subsequent graphs.

With the knowledge of these stiffness' as a function of span, the bending deformation and influence function (equation (5.5)), and torsional deformation and influence function equation (5.6)) can be calculated. The bending deformation and influence function is required for the study of the dynamic aeroelastic problems; the future study for this morphable wing.

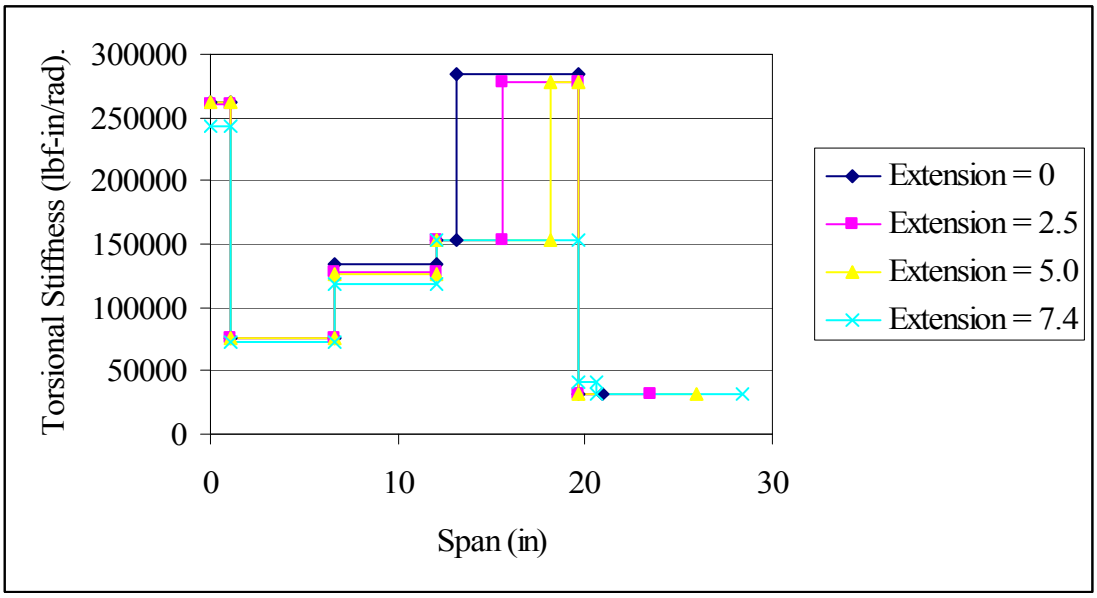

Figure 5.22: Plot showing the variation in torsional stiffness as a function of span for various values of extensions

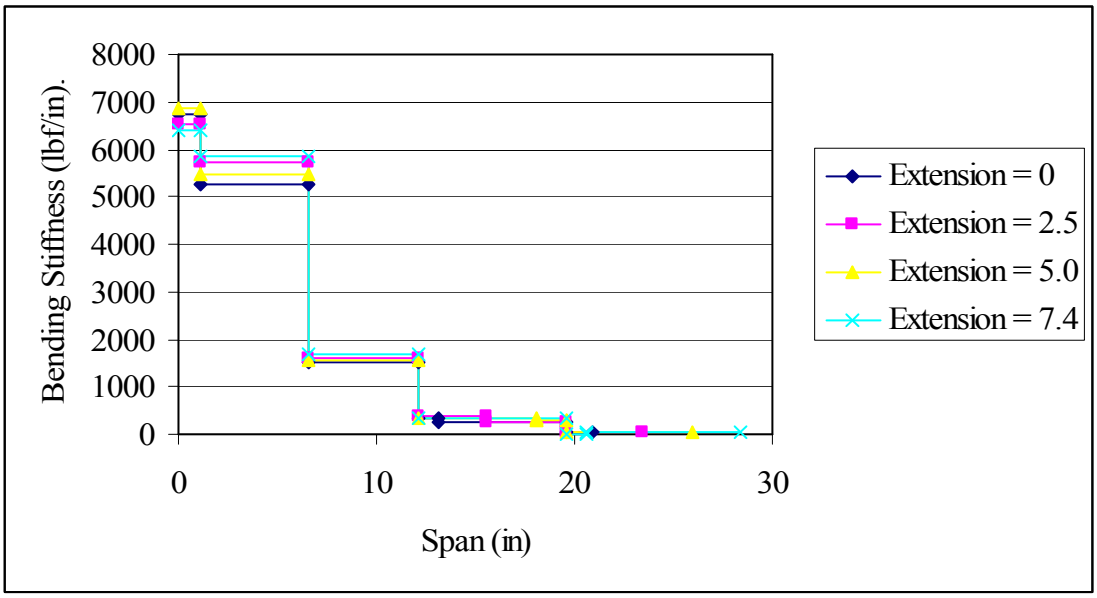

Figure 5.23: Plot showing the variation in bending stiffness as a function of span for various values of extensions

Using equations (5.18), (5.19), (5.20) and (5.21) the divergence speed is calculated for the aforementioned extensions. Following is an example calculation for the unextended case has been shown –

Based on the torsional stiffness information obtained from the above flowchart, using equation 5.5

$$C^{\theta\theta} = \begin{bmatrix} 0.000142657 & 0.000118095 & 7.72944E\text{-}05 & 4.19197E\text{-}06 & 0 \\ 0.000118095 & 0.000118095 & 7.72944E\text{-}05 & 4.19197E\text{-}06 & 0 \\ 7.72944E\text{-}05 & 7.72944E\text{-}05 & 7.72944E\text{-}05 & 4.19197E\text{-}06 & 0 \\ 4.19197E\text{-}06 & 4.19197E\text{-}06 & 4.19197E\text{-}06 & 4.19197E\text{-}06 & 0 \\ 0 & 0 & 0 & 0 & 0 \end{bmatrix}$$

The weight matrix was calculated by applying the Multhopp's quadrature formula. The procedure is outlined in Ref. [23] - Appendix B. And the value of $dC_L/d\alpha$ was obtained from the AVL results. The following eccentricity, chord and weight matrices were used,

$$e = \begin{bmatrix} 1.193952565 & & & & \\ & 0.532017064 & & & \\ & & 1.356673056 & & \\ & & & 0.997511799 & \\ & & & & 0.107233649 \end{bmatrix}$$

$$c = \begin{bmatrix} 7.50003 & & & & \\ & 9.20017 & & & \\ & & 9.20017 & & \\ & & & 9.20017 & \\ & & & & 10.0628 \end{bmatrix}$$

$$\overline{W} = \begin{bmatrix} 2.708773224 & & & & \\ & 5.37519008 & & & \\ & & 6.248484338 & & \\ & & & 6.574445527 & \\ & & & & 3.291760782 \end{bmatrix}$$

The following graph shows the approximated static wing divergence speed plotted as a function of varying extensions in the span.

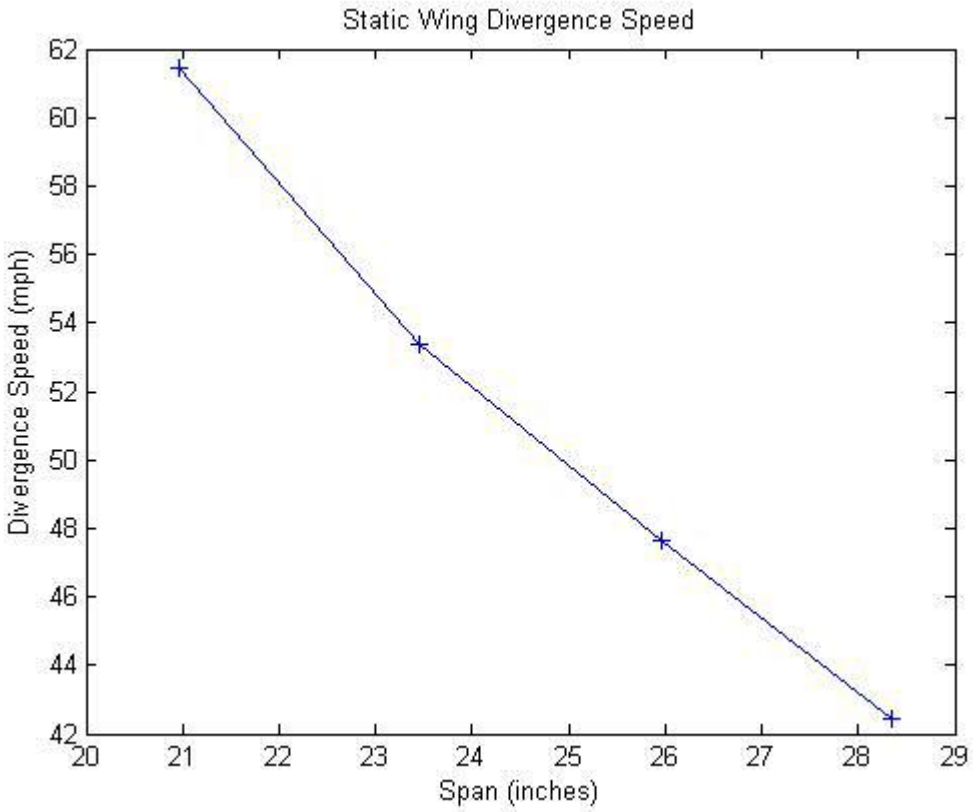

Figure 5.24: Static wing divergence Speed as a function of span

As expected, least divergence speed has been observed for the full extension wing configuration. Owing to the factor of safety, it is also to be noted that this speed is greater than the design speed of 33 mph.

CHAPTER 6

SUMMARY

6.1 Conclusions

The Appendix A shows the manufacturing details of the Balsa wood prototype and a few photographs of the assembled wing. This balsa wood wing will be tested in a Low Speed Wind Tunnel at the Aerodynamics Research Center, University of Texas at Arlington. A six-component small pyramidal balance measures the Lift, Drag, Side Force, Pitching Moment, Yawing Moment and Rolling Moment for the mounted wing. This strain gauge balance system is used to support a wing model in a wind tunnel, adjust its angle of attack over a plus-minus 25 degree range, adjust its angle of yaw over a 360 degree range and separate and measure the six force and moment components which determine the resultant force exerted by the air stream on the model.

The components are separated mechanically and measured through individual strain gauge load cells and readout is accomplished through appropriate electrical equipment. Component ranges of minus 50 to plus 100 pounds in Lift, minus 50 to plus 50 pounds in Drag and Side Force, minus 100 to plus 100 inch pounds in Rolling, Yawing and Pitching moments are recommended although overloads of at least 50% may be sustained. Adjustable stops on each load cell limit the deflection to a safe value. See Ref. [27]. But due to the mal-functioning of this force balance. the wind tunnel test results are a part of the future work.

Thus, to summarize the thesis objectives met:

- Morphing mechanism – conceptual design and development
- Rigorous structural and vibrational analysis
- Static wing divergence speed calculations for a wing with non-uniform structural properties as a function of span
- Computational approaches to study the changes in lift, drag and pitching moment due to variable aspect ratio and further extend the studies to the gull and the inverted-gull configurations

6.2 Proposed future work

The results from the AVL analysis will be validated via wind tunnel tests on the in-house manufactured Balsa Wood Wing at low speed subsonic conditions (quasi steady conditions).

A mathematical model will then be developed to be used to estimate the UAV flight performance as well as stability and control characteristics. Finally, the objective to characterize the vehicle dynamic response as well as the aerodynamic benefits (improved control authority) is thus achieved via differential telescopic extension and change in gull angle configuration (symmetric as well as asymmetric).

Thus, to summarize the proposed future work:

- Validation of the computational results via wind tunnel tests
- Verification of improvisation in the range capabilities due to morphing
- Verification of static wing divergence speed
- Roll- control authority – numerical simulation of aircraft dynamics

- Implication of transient actuation on aerodynamic instability such as flutter
- Thus obtain the control parameters to avoid aerodynamic instabilities
- Perform flight tests using the morphable wing and measure the performance augmentation capered to a traditional UAV.

APPENDIX A

PHYSICAL DIMENSIONS OF THE BALSA WOOD PROTOTYPE

(All dimensions in inch)

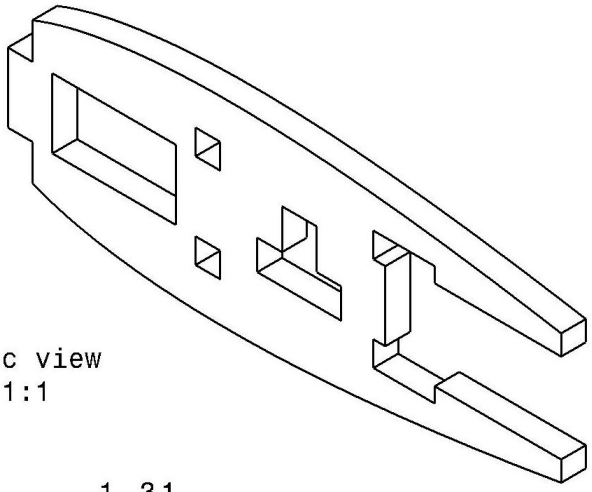

BASE
Isometric view
Scale: 1:1

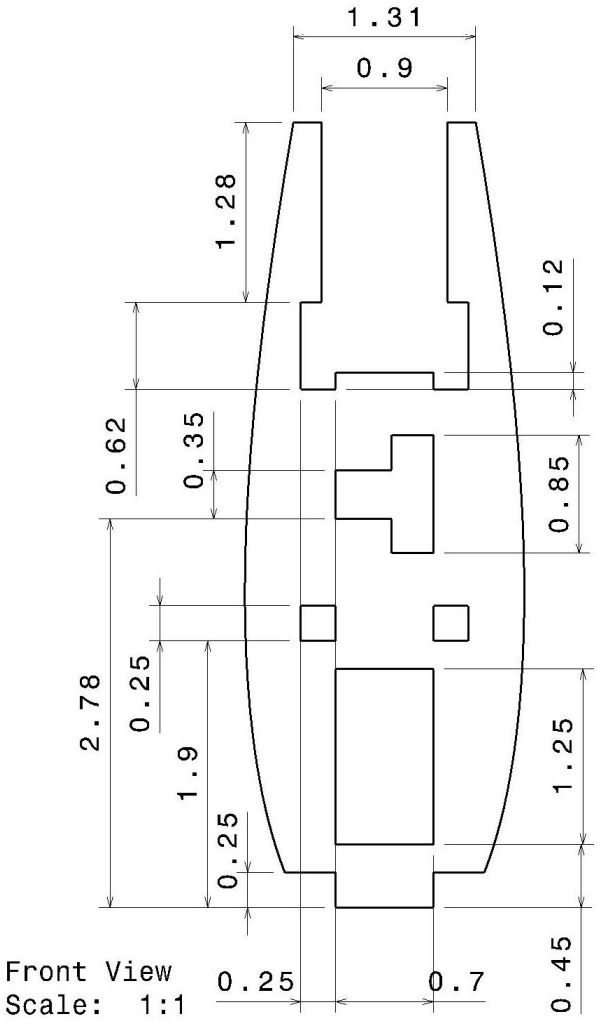

Front View
Scale: 1:1

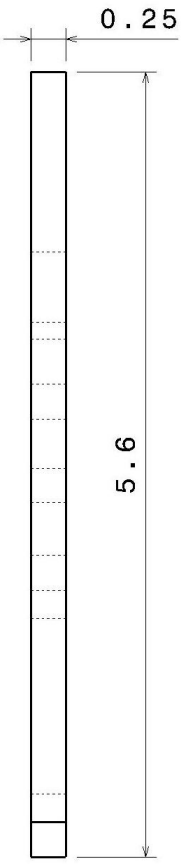

Top View
Scale: 1

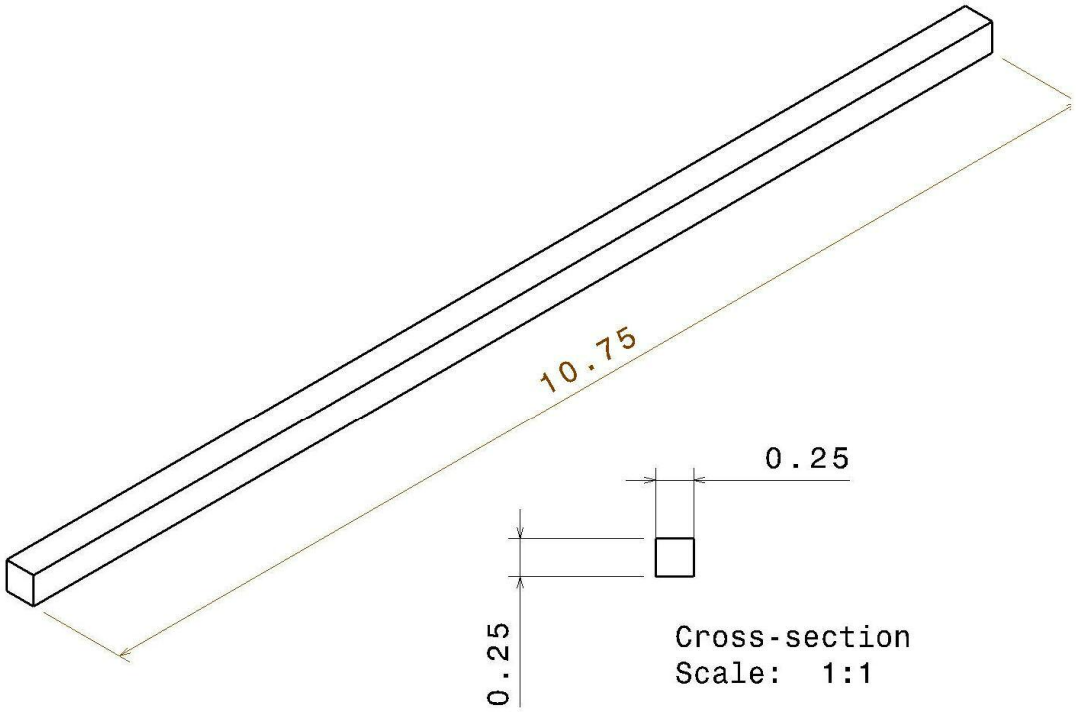

SPAR
Isometric view
Scale: 1:1

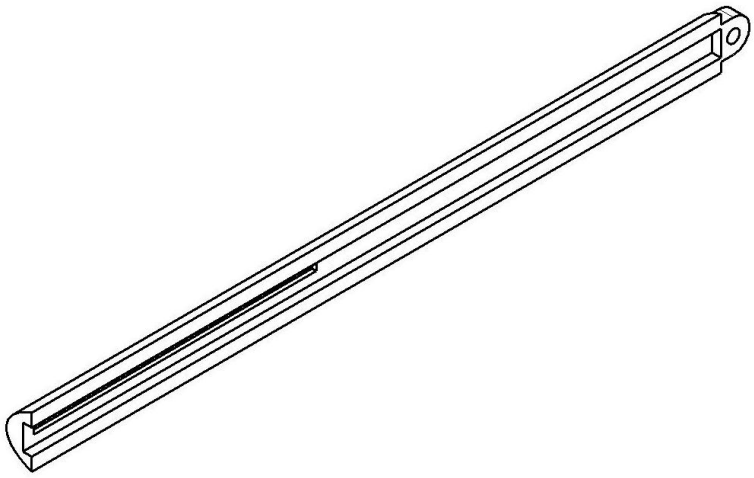

WING NOSE
Isometric view
Scale: 1:3

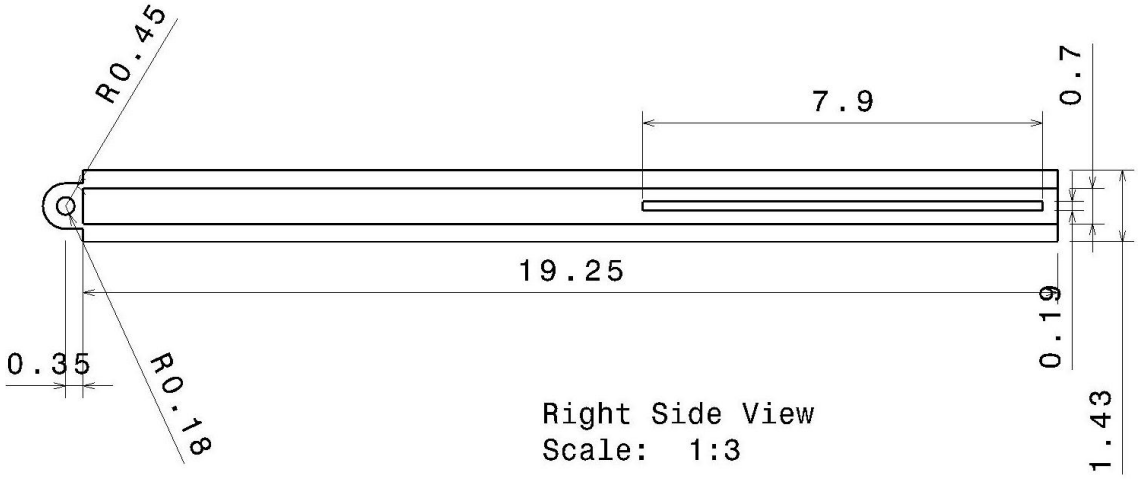

Right Side View
Scale: 1:3

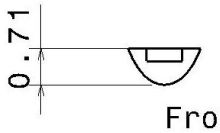

Front View
Scale: 1:3

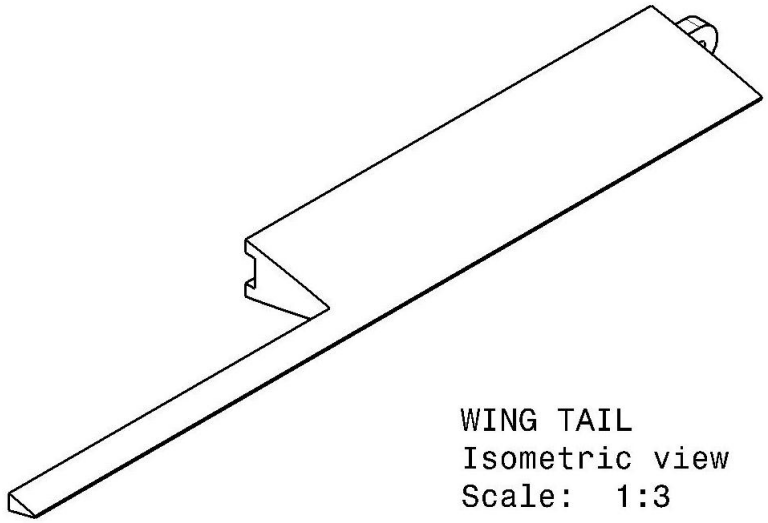

WING TAIL
Isometric view
Scale: 1:3

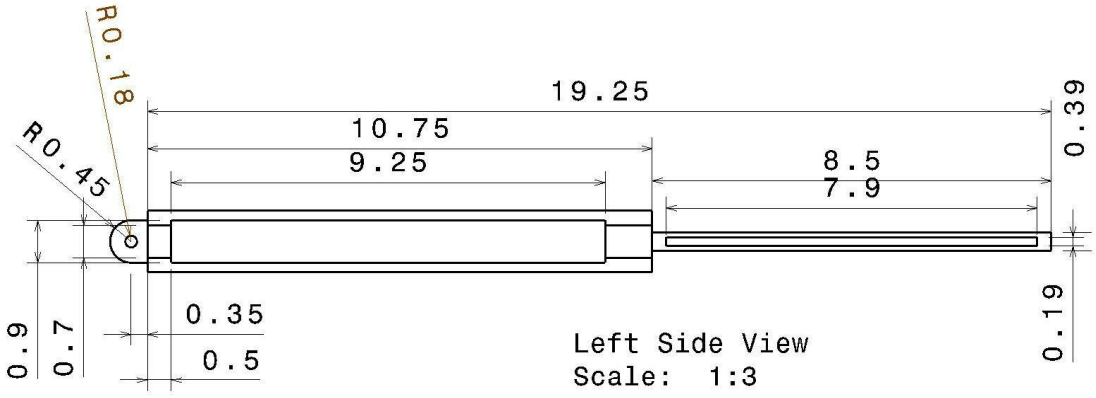

Left Side View
Scale: 1:3

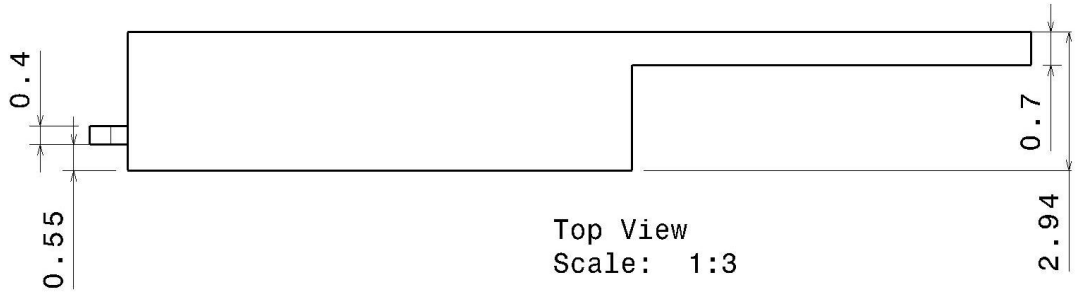

Top View
Scale: 1:3

C-CLAMP
Isometric view
Scale: 1:2

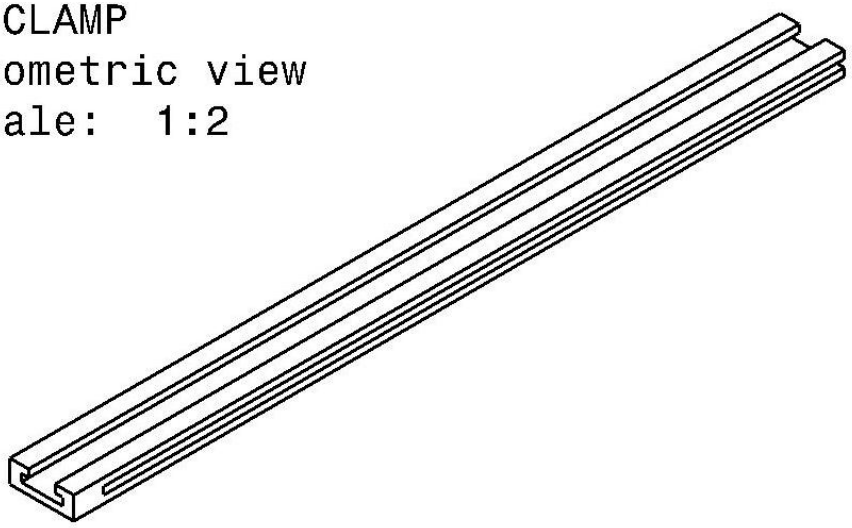

Top View
Scale: 1:2

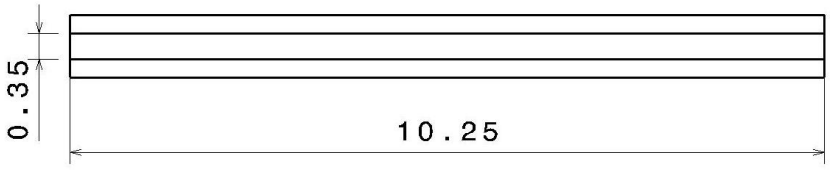

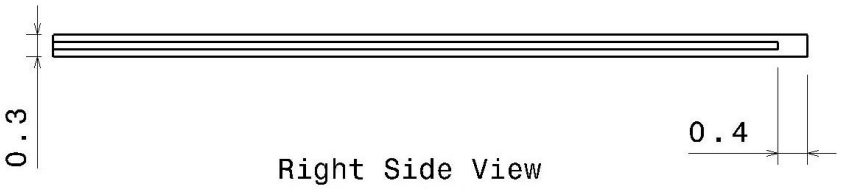

Right Side View
Scale: 1:2

Rear View
Scale: 1:2

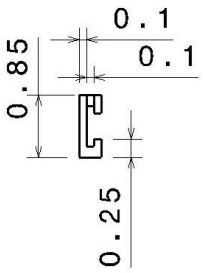

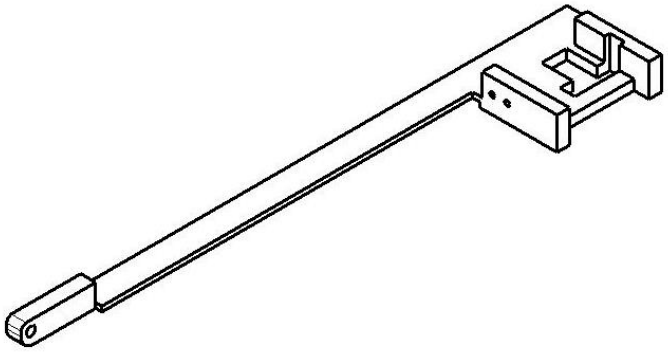

RACK BASE
Isometric view
Scale: 1:3

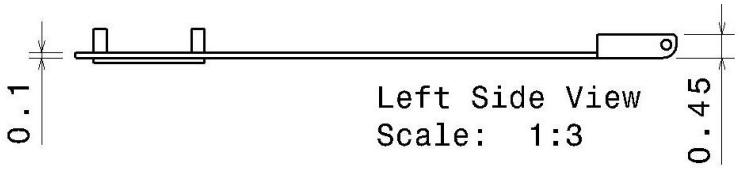

Left Side View
Scale: 1:3

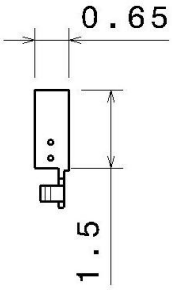

Right view
Scale: 1:3

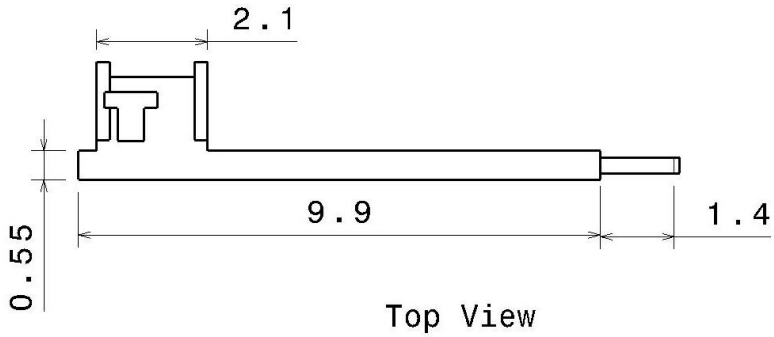

Top View
Scale: 1:3

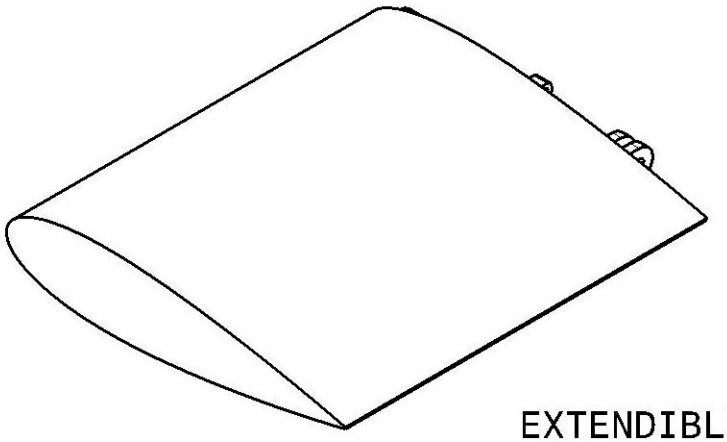

EXTENDIBLE WING
Isometric view
Scale: 1:3

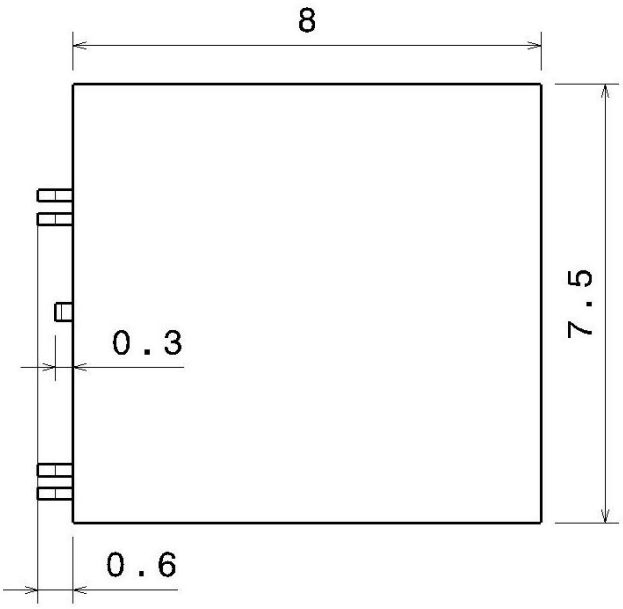

Top View
Scale: 1:3

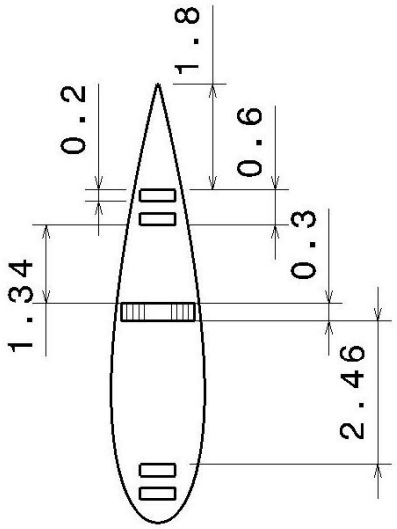

Rear View
Scale: 1:3

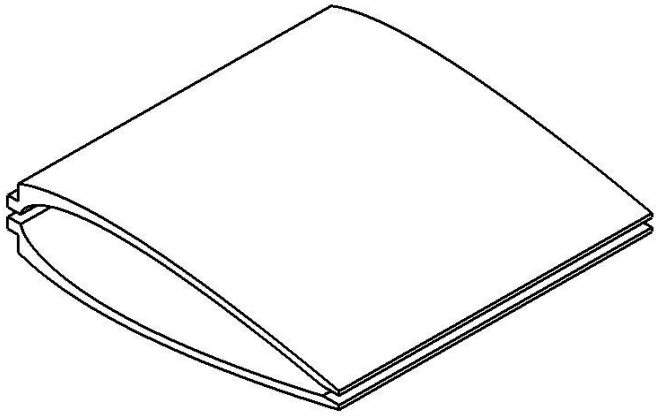

EXTENSION SUPPORT
Isometric view
Scale: 1:3

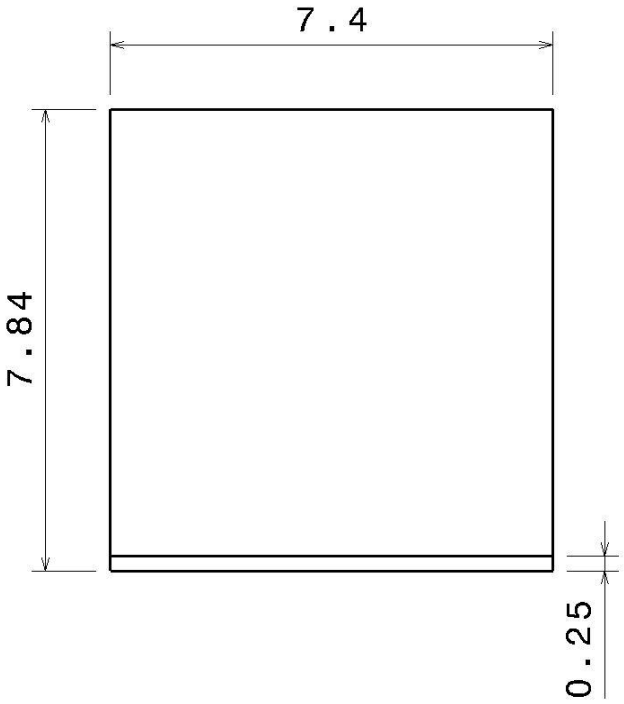

Rear view
Scale: 1:3

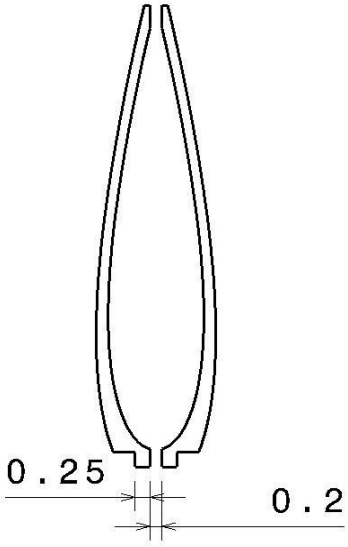

Left view
Scale: 1:3

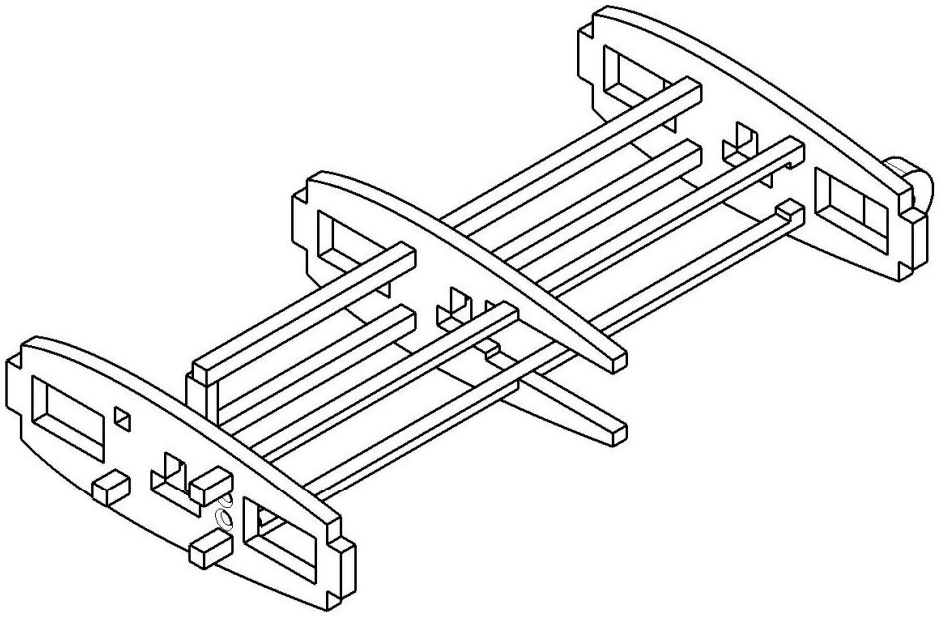

ASSEMBLY
Isometric view
Scale: 1:2

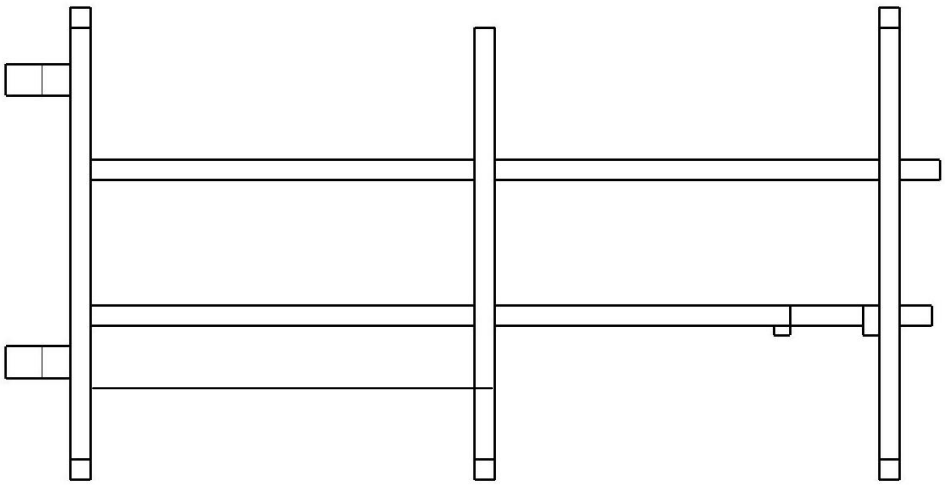

Top View
Scale: 1:2

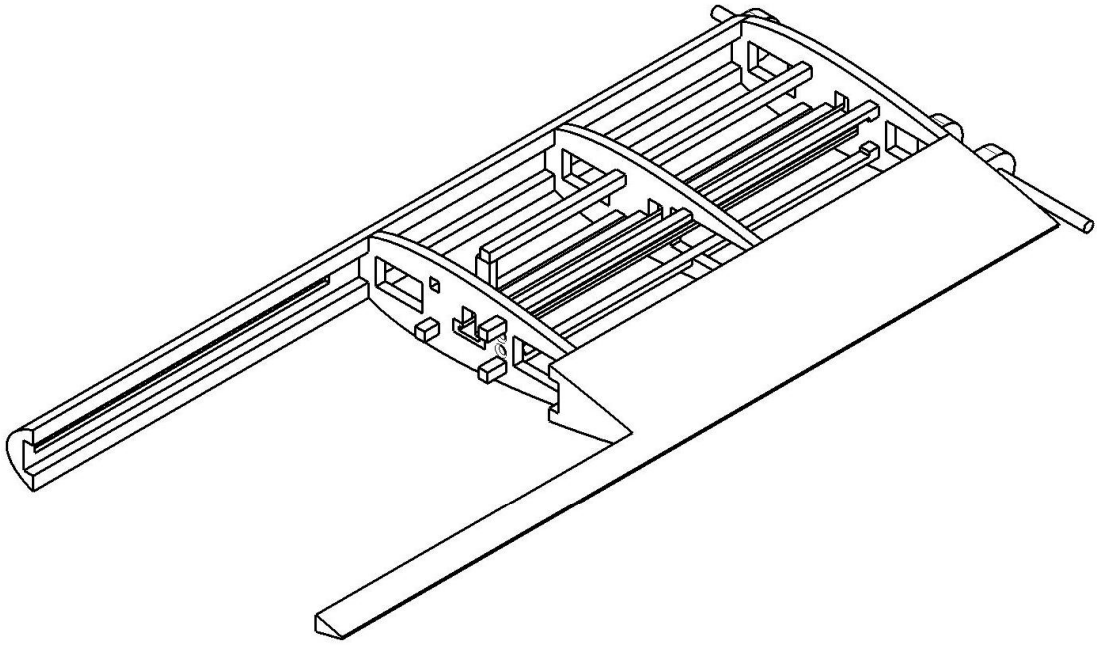

ASSEMBLY
Isometric view
Scale: 1:3

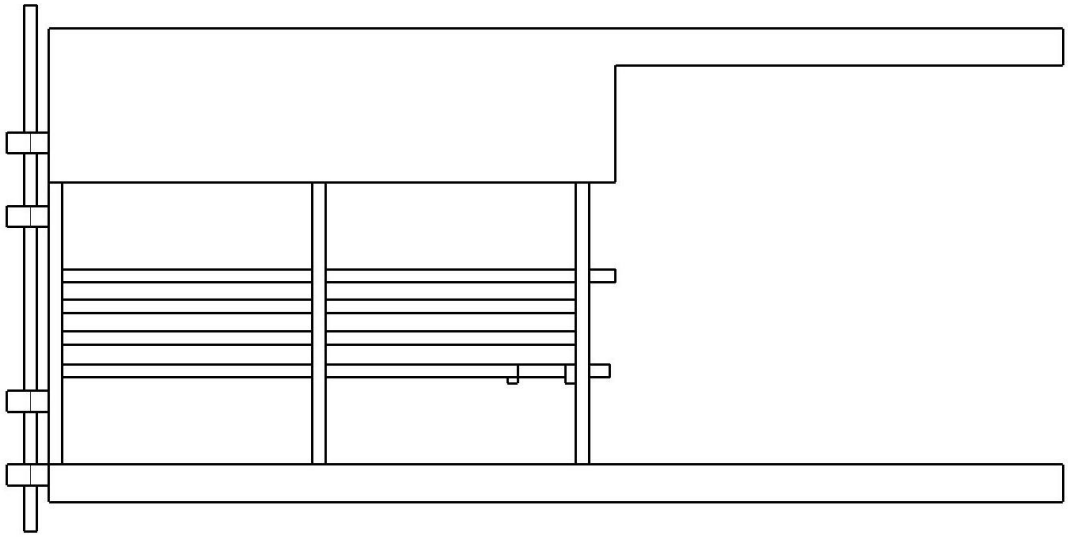

Top View
Scale: 1:3

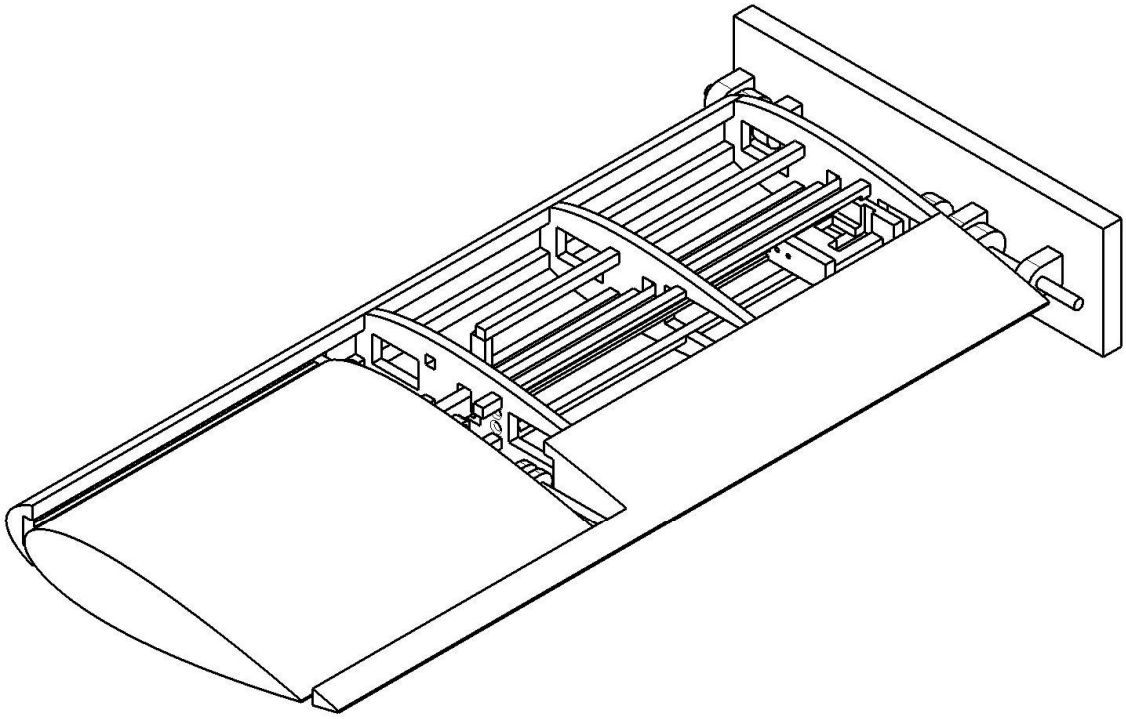

ASSEMBLY
Isometric view
Scale: 1:3

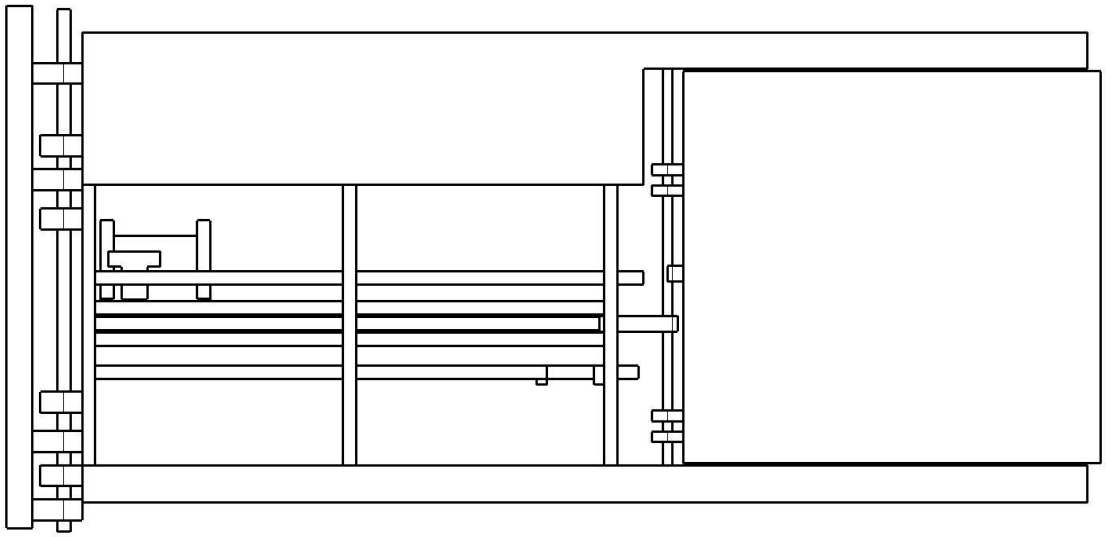

Top View
Scale: 1:3

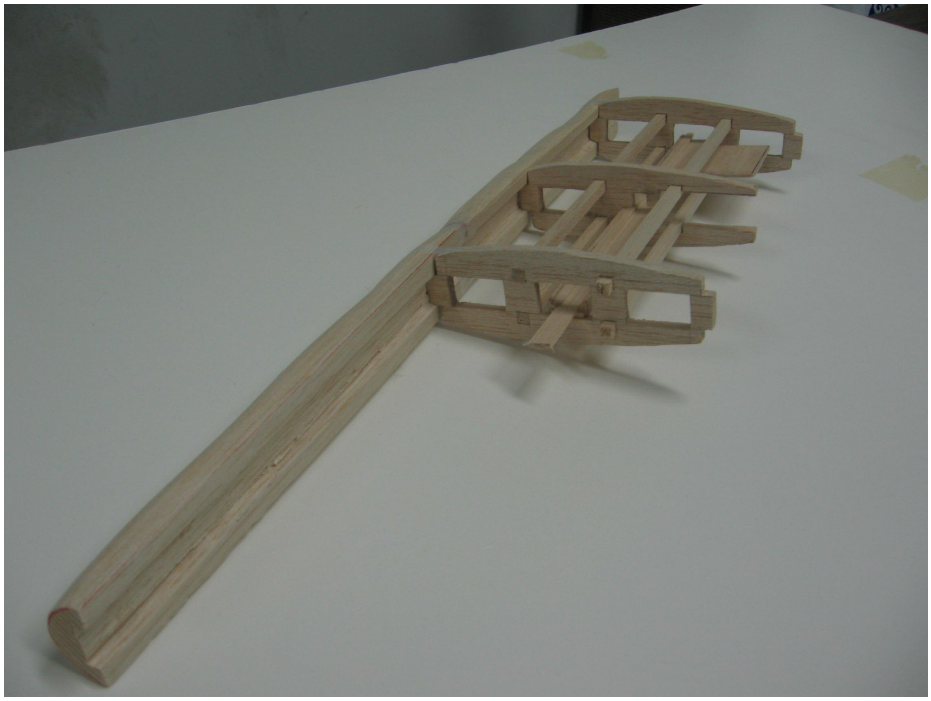

Figure: Shows the wing being assembled

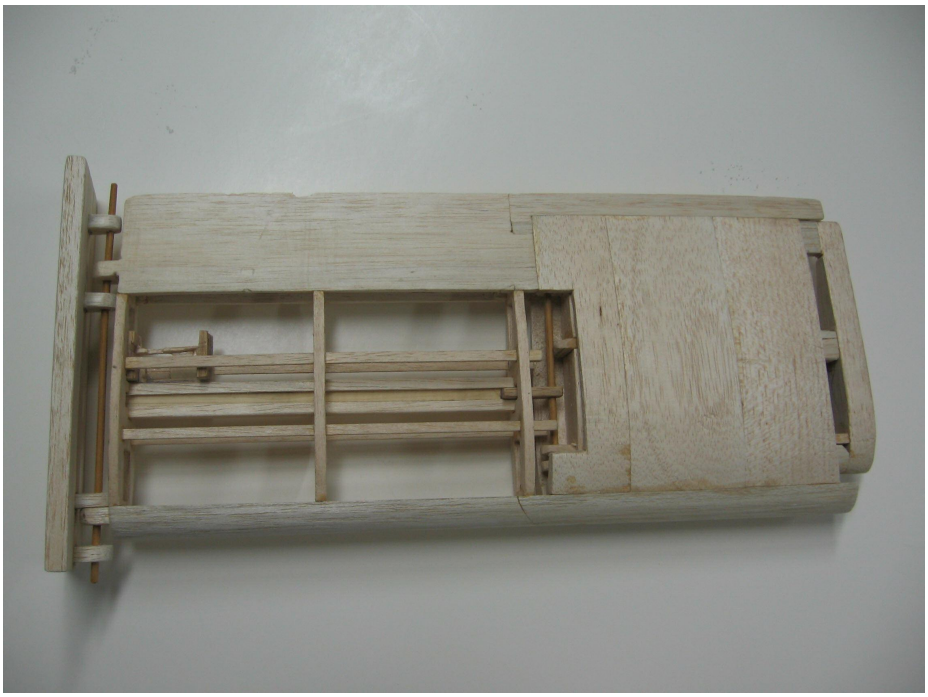

Figure: Shows the unextended wing configuration

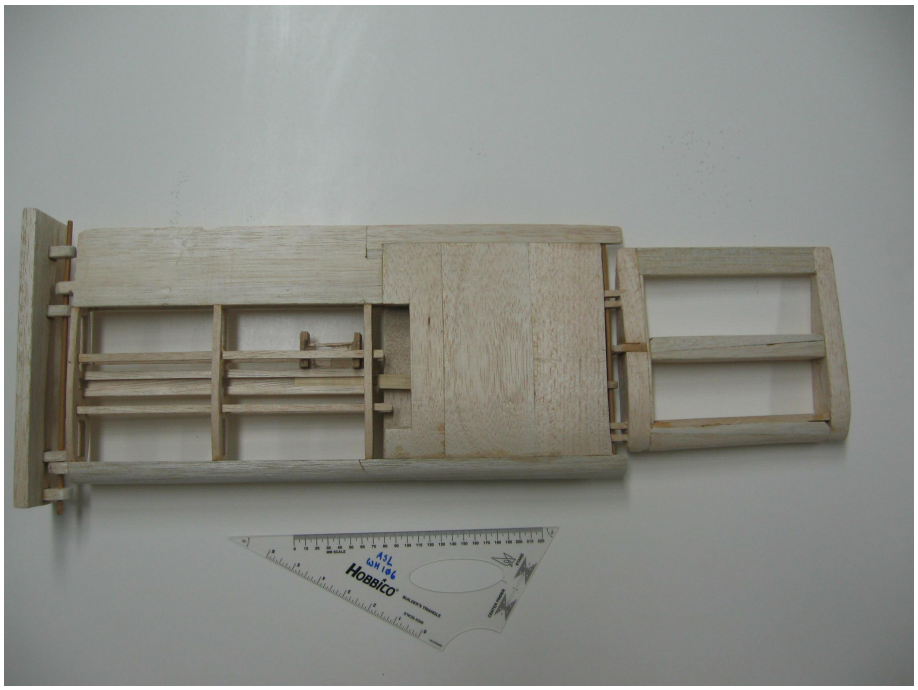

Figure: Shows the wing in extended configuration


Figure: Shows the wing in gull configuration

REFERENCES

[1]Ulla M. Lindhe Norberg (2002). Structure, Form, and Function of Flight in Engineering and the Living World. Journal of Morphology 252:52-81.

[2]Spillman, J., (1992). The Use of Variable Camber to Reduce Drag, Weight and Costs of Transport Aircraft. Aeronautical Journal, Vol. 96, Jan. 1992, pp. 1-8.

[3]Cone, C. D., (1963). The Aerodynamic Design of Wings with Cambered Span Having Minimum Induced Drag. NASA TR-R-152, 1963

[4]Wiggins, L. D., Stubbs, M. D., Johnston, C. O., Robertshaw, H. H., Reinholtz, C. F., and Inman, D. J., (2004). A Design and Analysis of a Hyper-Elliptic Cambered Span (HECS) Wing. 45th AIAA/ASME/ASCE/AHS/ASC Structures, Structural Dynamics & Materials Conference 19 - 22 April 2004, Palm Springs, California.

[5]Phillips, W., and Alley, N., (2007). Predicting Maximum Lift Coefficient for Twisted Wings Using Lifting-Line Theory. AIAA-2007-1267. 45th AIAA Aerospace Sciences Meeting and Exhibit, Reno, Nevada, Jan. 8-11, 2007

[6]Ma, B. F., Liu P. Q., Wei, Y., (2004). Effects of Wing and Canard Sweep on Lift-Enhancement of Canard-Configurations. Journal of Aircraft 2004, 0021-8669 vol.41 no.6 (1521-1523)

[7]Henry, J. J., Blondeau, J. E., and Pines, D. J., (2005). Stability Analysis for UAV's with a Variable Aspect Ratio Wing. 46th AIAA/ASME/ASCE/AHS/ASC

Structures, Structural Dynamics and Materials Conference; Austin, TX; Apr. 18-21, 2005

[8]Bae, J. S., Seigler, T. M., Inman, D. J., (2004). In Lee, Aerodynamic and Aeroelastic Considerations of A Variable - Span Morphing Wing. 45th AIAA/ASME/ASCE/AHS/ASC Structures, Structural Dynamics and Materials Conference; Palm Springs, CA; Apr. 19-22, 2004

[9]Blondeau, J., Richeson, J., and Pines, D.J., (2003). Design, Development and Testing of a Morphing Aspect Ratio Wing Using an Inflatable Telescopic Spar. AIAA Paper 2003-1718, 44th AIAA/ASME/ASCE/AHS Structures, Structural Dynamics, and Materials Conference and Exhibit, Norfolk, VA, April 7-10, 2003.

[10]Ehlers, S.M., and Weisshaar. T.A., (1990). Static Aeroelastic Behavior of a Laminated Piezoelectric Composite Wing. AIAA paper 90-1078-CP

[11]Pettit, G. W., Robertshaw, H. H., and Inman, D. J., (2001). Morphing wings for Unmanned Aircraft. Smart Materials Bulletin, Feature Article, November, 2001

[12]Ifju, P. G., Jenkins, D. A., Ettinger, S., Lian, Y., Shyy, W., Waszak, M. R., (2002). Flexible-Wing-Based Micro Air Vehicles. AIAA 2002-0705

[13]Jacob, J. D., (1998). On The Fluid Dynamics Of Adaptive Airfoils. Proceedings of 1998 ASME International Mechanical Engineering Congress and Exposition, November 15-20, 1998, Anaheim, CA, USA

[14]Bowman, J., Sanders, B., and Weisshaar. T. (2002). Evaluating the Impact of Morphing Technologies on Aircraft Performance. AIAA Paper 2002-1631, April 2002

[15]Egon Stanewsky (Oct. 2000). Aerodynamic benefits of adaptive wing technology. Aerospace Science and Technology (1270-9638). Vol. 4, no. 7, pp. 439-452.

[16]Abdulrahim, M., and Lind, R., (2004). Flight Testing and Response Characteristics of a Variable Gull-Wing Morphing Aircraft. AIAA Guidance, Navigation, and Control Conference and Exhibit 16 - 19 August 2004, Providence, Rhode Island

[17]Grant, P. J., Gulls- A Guide to Identification, Printed and bound in Great Britain by The Bath Press

[18]Liu, T., Kuykendoll, K., Rhew, R., and Jones, S. (2004). Avian Wings, 24th AIAA Aerodynamic Measurement Technology and Ground Testing Conference, 28 June – 1 July 2004, Portland, Oregon

[19]Andy Lennon, Basics of R/C Model Aircraft Design – Practical Techniques for building better models, Published by Air Age Inc.

[20] http://www.balsasales.co.uk/technical_info.html - Mechanical properties of Balsa Wood

[21]http://www.quadrantepp.matweb.com/SpecificMaterialNew.asp?bassnum=P1SM03&group=General - Mechanical properties of Delrin

[23]Bisplinghoff, R. L., Ashley, H., and Halfman, R. L., Aeroelasticity, Dover Publications, Inc., New York, 1996, pp. 429 – 434

[24]Housner, G. W., Vreeland, T., Jr., The Analysis of Stress and Deformation, The Macmillan Company, New York, 1966

[25]Goett H. J., and Bullivant, W. K. Test of N.A.C.A. 0009, 0012, and 0018 Airfoils in the full-scale tunnel. Report No. 647 – National Advisory Committee for Aeronautics

[26]Anderson J. D., Jr., Introduction to Flight, McGraw-Hill, New York, 1985, pp. 448

[27]Documetation at Aerodynamics Research Center, University of Texas at Arlington

BIOGRAPHICAL INFORMATION

"Complex things are made using simple concepts and basic principles". Till date, Abhijit has always reassured the truthfulness of this statement. Born in Pune, India, Abhijit mostly enjoyed flying kites and playing with marbles. After finishing his 10^{th} grade from the Loyola High School, Pune and he moved to the Fergusson Junior College to pursue his interests in the field of science.

Always fascinated by the applications of physics and mathematics in every-day life, they became subjects of principle interest to him. Abhijit secured admission to major in Mechanical Engineering at the Government College of Engineering, Pune, under the Pune University. Apart from the internship and projects during his undergraduate studies, Abhijit actively represented his school at the National Level Rowing Championships.

Through campus recruitment, Abhijit was placed in the Technology Centre, the Design and Development Group for Defense, Nuclear and Aerospace Cluster in the Heavy Engineering Division at Larsen and Toubro Limited. He was a part of the design and development team for the mission critical systems for the Indian Defense Establishment.

Abhijit's desired area of research is in the field of mathematical modelling and control of autonomous systems. He has pursued a systematic approach towards the design and development of the morphable wing as a part of his Master's thesis.